Digitally Enhanced Dispersion Spectroscopy

Justin Wong

A thesis submitted for the degree of
Doctor of Philosophy
at the Australian National University

September 10, 2025

Declaration

This thesis is an account of research undertaken between August 2020 and February 2025 at The Center of Gravitational Astrophysics, Department of Quantum Science, in the Research School of Physics at The Australian National University, Canberra, Australia.

Except where acknowledged in the customary manner, the material presented in this thesis is, to the best of my knowledge, original and has not been submitted in whole or part for a degree in any university.

Justin Wong

February, 2025

Acknowledgements

This thesis is the sum of many acts of kindness and charity that have been done to me, especially by my supervisors, Dr. Chathura Bandutunga, Associate Professor Malcolm Gray, and Professor Ben Buchler.

First of all, big shout out to my primary supervisor and scientific mentor, Dr. Chathura Bandutunga. This PhD would not have been possible without your technical guidance and leadership of the lab over the past four years, often under trying circumstances. Your work ethic, combined with ridiculous breadth of knowledge: theoretical, experimental, and practical, inspires me to do better. And thanks for keeping me on track during the tumultuous final year of this PhD.

To Mal, much of the experiments written in this thesis sprung from your "wacky ideas". You were an endless fount of novel techniques and suggestions, always shared generously and patiently. Thank you also for your strong scientific convictions, and being the staunchest defender of our papers come review time. And to Ben, thank you for taking me under your wing during a sensitive time, and offering so much support.

I am also greatly indebted to Dr. Jong Chow. Your lectures sparked my interest in optical metrology, bringing me into this fascinating field. You then took a chance on me, bringing me onto the PhD program. Thank you for seeing something in me; I still can't believe I've made it through four years.

I couldn't have asked for a more friendly and supportive place to work than The Center for Gravitational Astrophysics. Thanks especially to Anneshwa and Paul, who assisted greatly with digital signal processing. You both were so generous with your time, and were willing to help at a moment's notice. Thank you to Anika, for seeing through some of the ideas in this thesis to their conclusion. I'd also like to thank Sareh for going above and beyond to support all members of CGA. To my fellow CGA members, past and present: David, Zhang Ya, Terry, Logan, Zoe, Kandeel, Dan, Kar Meng, Sheon, Kirk, Andrew, Ben, Jen, Jennifer, Neil, Emily, Callum, Dana, Johannes, Roland, Bram, Keshu, thank you for all the great chats, about PhD life, about physics, or just random facts. A PhD can be a lonely journey, but all of you made it much less so.

I am also grateful to Shridhar, Marius, and Dragomir at TMOS for taking a chance on some of the concepts in this thesis, and finding an application for them. Within the university, last but not least, thank you to Luda and the Physics HDR Administration. You've been very understanding and patient through the years.

To my parents: thank you for inculcating my curiosity from the very beginning. It's not easy to have a child asking "Why?" about everything. And thank you for all the support and unconditional love, despite not having been a very good son.

Finally, to D. I work with light everyday, but you are the constant light that has illuminated everything in my life.

Abstract

Molecular dispersion spectroscopy for the optical detection, and characterization of anomalous dispersion is a developing field for the interferometric measurement of trace gas concentrations. As a phase sensitive detection technique, it eliminates the need for baselining or normalization of the spectroscopic signal which is typically required for absorption spectroscopy methods. Furthermore, dispersion sensitive methods excel at measuring through high optical depth, where absorption techniques are limited by the exponential response required by the Beer-Lambert Law.

This thesis presents novel architectures for dispersion spectroscopy using digital interferometry (DI), a laser metrology technique that enables range gated interferometric phase measurements using the correlation of pseudo-random binary sequences (PRBS) modulated onto the optical field. This enables rejection of unwanted scattered noise or other cross-talk down to microradian phase sensitivities, as well as a reduction of optical complexity and relaxation of electronic bandwidth requirements. Firstly, as a proof of concept, a Sagnac architecture is used to demonstrate digital interferometric phase extraction, achieving 2×10^{-7} rad/$\sqrt{\text{Hz}}$ sensitivity. Following this, a vapor cell is inserted into the sensing path, transforming the interferometer into a spectrometer. Using this instrument, and leveraging the sub-microradian phase noise, a baseband dispersion readout with 77 ppb $\times$ m/$\sqrt{\text{Hz}}$ concentration sensitivity is demonstrated. This sensitivity is possible due to the inherently matched path lengths of the Sagnac interferometer.

Subsequently, a more flexible in-line technique using a re-entrant delay line is developed. This creates a dispersion spectrometer which uses DI multiplexing to synthesize multiple sets of matched path lengths and a noise-suppressed measurement, achieving a phase sensitivity of 8×10^{-6} rad/$\sqrt{\text{Hz}}$, corresponding to a 159 ppb $\times$ m/$\sqrt{\text{Hz}}$ concentration sensitivity. This is a factor of two higher compared to the Sagnac architecture. However, the re-entrant optical architecture allows integrated wavelength tuning linearisation as well as greater flexibility in the measurement of spectroscopic samples. Finally, the thesis discusses ongoing work on extending the optical bandwidth of the re-entrant spectrometer, using an optical amplifier to generate a digitally addressable frequency comb. This has applications in the interrogation of wider linewidth resonance features such as metasurfaces.

Contents

List of Figures

1 Introduction

The interaction of light with matter is the fundamental principle of spectroscopy. This interaction can take many forms, including absorption, emission, scattering, and polarization rotation, lending names to a wide variety of spectroscopic methods. Among these methods, perhaps the most common for chemical and biological analysis is absorption spectroscopy, due to its simplicity in implementation. In its most simple form, light is passed through a spectroscopic sample, and then onto a dispersive element in front of a camera. The resulting spectrum contains information about the absorption of the sample, as wavelengths that are absorbed will result in fainter pixels on the camera. Plotting the intensity of each pixel results in an absorption line. This technique was first developed for atomic spectroscopy in the 1950s [1].

With the advent of the laser in the 1960s, the sensitivity of absorption spectroscopy techniques was no longer limited by the resolution of the dispersive element, but by laser linewidth. Furthermore, lasers allowed for higher sensitivity due to a lower shot noise limit, as optical power is focused in a narrow wavelength band around the absorption line of interest.

These properties of lasers, along with the ability to precisely control the wavelength, coherence, timing, and intensity of light, has made laser spectroscopy one of the most powerful tools in the analysis and elucidation of molecular structures. Within the research laboratory, this has seen applications in the development and analysis of new drugs, reagents, and materials [2]. The more recent developments of ultrafast and attosecond lasers [3] have also enabled the resolution of the dynamics of chemical reactions.

Concurrently, the development of portable, low cost, and widely tuneable semiconductor lasers has paved the way for applications of molecular laser spectroscopy outside of the laboratory— in industrial settings [4], as well as remote sensing and astrophysics [5]. In particular, for remote sensing applications, direct laser absorption spectroscopy has seen widespread use and development in recent years due to its flexibility and ability to perform highly sensitive atmospheric measurements of trace and greenhouse gas concentrations [6, 7]. This is due to its relatively high sensitivity and specificity, and its simple architecture and setup, which does not require an optical cavity.

Although, broadly speaking laser absorption spectroscopy can be divided into cavity enhanced and direct laser absorption techniques, in this thesis, we will focus on a variant of

direct absorption techniques, looking towards applications in remote sensing, as direct absorption techniques do not require the analyte of interest to be confined within an optical cavity.

1.1 Dispersion Spectroscopy

Anomalous Dispersion and resonant absorption are intrinsically linked optical phenomena. Resonant absorption occurs when photons of specific energies are absorbed by a medium, reducing the intensity of transmitted light and providing information about molecular composition. Anomalous dispersion, on the other hand, describes the variation of a material's refractive index with wavelength around an absorption line, which can be directly derived from absorption data using the Kramers-Kronig relations. This relationship arises because absorption implies energy dissipation, which in turn affects the phase velocity of propagating light. Thus, by measuring dispersion, one can infer absorption properties, and vice versa [8].

Anomalous dispersion is a fundamental property of all oscillators, and like most oscillators, we can construct an analogy using the time-honored picture of pushing a child on a swing. Every swing has a natural resonant frequency determined by the length of the chain. The most efficient way to push the swing is to apply force when the swing returns to its highest position, ie. at its resonant frequency, or alternatively, in phase with the oscillation. This is when the system absorbs the most energy. We can think of this as the absorption peak of a molecule.

Pushing the swing too soon (when it hasn't reached its highest point), or too late is less efficient, resulting in less energy being absorbed by the system, and less height on the swing. By analogy with spectroscopy, this occurs on the wings of the absorption line, away from the resonant frequency. In the phase picture, we can think of pushing the swing too soon or too late as being out-of-phase with the natural oscillation of the swing. Hence, we can see that absorption (amplitude) and anomalous dispersion (phase) are intrinsically linked in any oscillator.

1.1.1 Why Dispersion?

Direct laser absorption spectroscopic methods fall into two main categories, the first of which measures absorption - a change in field amplitude. A highly simplified model of this technique for greenhouse gas detection can be described as a collimated laser beam passing through a spectroscopic analyte to a photodetector. As the laser wavelength is tuned, absorption lines are resolved as a change in the optical power reaching the photodetector, and thus the sensor output voltage. These methods have long dominated due to their simple optical setup and relatively high sensitivity, approaching parts per million in gas concentration. Unfortunately, direct absorption spectroscopy suffers from some inherent limitations associated with amplitude measurements.

Chief among these limitations is noise in the power incident on the photodetector. Absorption spectroscopy treats the instantaneous photodetector voltage as a proxy for absorption strength, any amplitude noise is directly coupled as noise on the absorption signal. As laser absorption spectroscopy typically requires the laser to be wavelength tuned over a nanometer, this typically results in an associated residual amplitude modulation. Although this effect is repeatable and can be calibrated out in a process known as baselining,

it adds a layer of complexity to the technique. More pernicious is the effect of scattering or thermal absorption by spurious particles in the beam path. This effect is stochastic and thus cannot be baselined. These effects occur at relatively slow timescales below tens of Hertz. Although it is possible to reduce this effect by frequency modulating the laser such that the readout is moved away from lower frequencies where these noise sources occur, it cannot be removed entirely.

Another limitation associated with absorption measurements is the exponential decay of the measured intensity as concentration and/or sample length increases, as required by the Beer-Lambert Law. At high concentrations, this means fewer photons detected, and lower sensitivity to changes in concentration, thus reducing the dynamic range of measurement [9] This instrument error is known as photometric error.

A third and final limitation of absorption spectroscopy is the physical breakdown of the Beer Lambert law itself, which states that the absorbance is linear with concentration. However, this is only valid approximations for low concentrations with correspondingly small absorbance. For measurements where the absorbance is greater than ten percent, it can be shown using the Lorentz oscillator model of absorption [10] that the Beer-Lambert law is a first order approximation of a nonlinear function. This also poses a limitation where high dynamic range is required, as sensitivity at high concentrations is reduced due to flattening of linear relationship between concentration and absorbance. This further reduces the sensitivity obtained by absorption spectroscopy at high concentrations, as the absorbance curve itself flattens.

Alternatively, spectroscopic information can be obtained by measuring anomalous dispersion as the wavelength of a laser source is swept across a spectral line. This is because the molecular resonances can also be modelled as harmonic oscillators, and so must obey the Kramers-Kronig relations.

Heuristically, we model a simple molecule as two balls and a spring, forming a dipole. When radiation is incident, this drives the spring system, causing the molecule to oscillate, and the dipole to radiate. Absorption occurs due to destructive interference between the dipole radiation and incident radiation [11]. Drawing upon the analogy of the swing, we can see that changing the incident radiation to slightly below the resonant frequency will lead to incomplete destructive interference (less absorption), and also a lag in phase. By measuring this phase shift, the absorption (and thus concentration) can be obtained.

Crucially, since dispersion spectroscopy measures phase directly, it avoids the need to calibrate acquired spectra for laser intensity fluctuations as the laser frequency is tuned. The dispersion phase signal is also linearly proportional to concentration, in contrast to the amplitude based absorption signal, which follows the exponential Beer-Lambert Law. Finally, it has been proven that dispersion is highly linear with concentration, even for optically thick samples, where the Beer Lambert Law begins to breakdown and 'saturate'. This linearity has been shown to be preserved until the intensity of transmitted light through the strongly absorbing sample falls below the shot noise limit [9]. Thus, dispersion methods circumvent the sensitivity limits of amplitude methods when performing high concentration measurements, retaining linear sensitivity, and enabling a large measurement dynamic range.

A

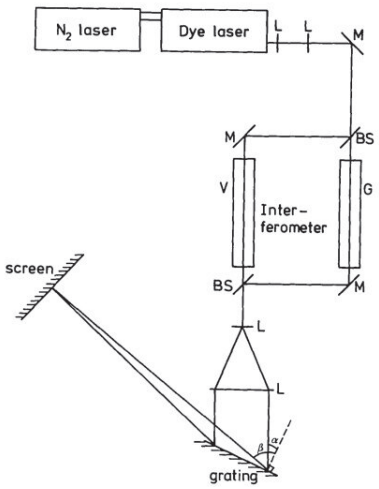

B

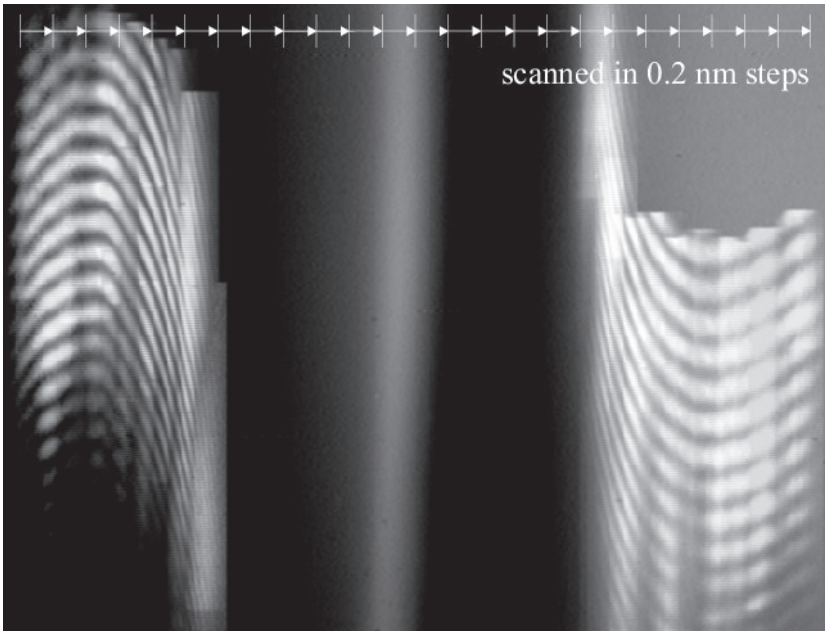

Figure 1.1: In the top panel, a typical experimental setup for Hook Method spectroscopy is reproduced [12]. A pumped dye laser is used as the light source. This is split by a beamsplitter into a path labeled G (gas tube) which contains the analyte and a path labeled V (vacuum). The two paths are recombined with a second beamsplitter, forming a Mach-Zehnder interferometer. Following recombination, the beam is incident on a grating and viewed on a screen. In the bottom panel, a spectrogram on a screen from a typical hook method interrogation of mercury vapor is reproduced [13]. The two characteristic hooks are visible, but the fringes around the linecenter are not resolved as the rate of phase change (fringe spacing) is greater than the spectrometer and camera spatial resolution. However, since the spectrometer resolution is known (0.2 nm here), the linewidth and strength can be determined. Reproduced from Kindel and Adler.

1.1.2 Early Methods of Measuring Dispersion

The first spectroscopic method to exploit anomalous dispersion, developed in 1912 is called the Hook Method. Here, a Mach Zehnder interferometer where one of the arms is filled with an analyte gas is interrogated with a broadband source, and the light from one of the outputs of the beamsplitter is dispersed by a grating and viewed on an observation screen, forming a two dimensional interference pattern. At the location on the screen corresponding to the absorption line wavelength, two characteristic hook shapes can be seen in the fringe pattern, giving this technique its name. The hook shapes represent a high rate of change of phase in the vicinity of the absorption line, as required by the Kramers Kronig Relations. Thus, by measuring the hook separation on the screen, the absorption strength can be calculated. An example of a hook method measurement is given in Figure 1.1 [12] [13]. Despite the development of lasers and precision spectrographs for use with the hook method, these methods were still reserved to analyze oscillator strengths of atomic vapor absorption and emission lines [1], as their precision was limited by spectrograph bandwidths, and limitations in fringe resolution and counting in traditional interferometric methods.

1.1.3 Laser Dispersion Spectroscopy

The development of the laser, with its high temporal coherence enabled interferometric dispersion measurements where phase could be measured directly instead of inferred from fringe counting. The first such measurement was done by Crance et al.in 1975 [14], using a Michelson interferometer with one of the arms containing an atom vapor. The use of a tunable dye laser along with a piezo-driven Michelson mirror allowed for a heterodyne measurement where phase was measured directly from in-phase and quadrature signals recorded on an oscilloscope. At the same time, work continued on laser based Hook Method techniques using Fabry-Perot resonators to enhance the interaction length [15]. With equipment available at the time, these experiments were generally easier to setup compared to the Michelson interferometer method developed by Crance et al. The first demonstration of a dispersion spectroscopy technique sensitive enough to measure the anomalous dispersion around ro-vibrational transitions of molecules was done in 2003 by Marchetti et al [16]. This was done by counting fringes in the transmission spectrum of a Fabry Perot cavity containing carbon dioxide. An inherent limitation of the fringe counting method is a phase sensitivity on the order of radians, relying on the long interaction length of the cavity instead to boost the dispersion signal.

Chirped Laser Dispersion Spectroscopy

The first family of methods developed to leverage modern interferometric techniques for directly interrogating dispersion induced phase shifts was Chirped Laser Dispersion Spectroscopy (CLaDS) [17]. This technique makes use of a heterodyne interferometer with an acousto-optic modulator (AOM) acting as an initial beamsplitter. The zeroth order and the first order diffracted beams function as two interferometer arms. The two beams are then recombined at a beamsplitter, and then passed through a vapor cell containing the spectroscopic analyte (nitric oxide). A conceptual diagram of a minimal configuration for the CLaDS interferometer is shown in Figure 1.2a.

The effect of the AOM shift is to produce sidebands that experience differing phase shifts corresponding to the dispersion profile of a spectroscopic sample. The resulting differential

signal is the first derivative of the dispersion curve around the transition of interest. The amplitude of the signal scales with the magnitude of the AOM frequency shift, where the optimal shift is on the order of the transition linewidth [18]. This phase shift is converted to a frequency shift with an enhancement factor corresponding to the frequency chirp rate of the laser source, and then frequency demodulated using standard RF demodulation techniques. By encoding dispersion induced phase shifts as frequency instead of amplitude modulation, this technique circumvents noise associated with amplitude fluctuations either due to laser tuning or the environment. Additionally, the measured frequency shift and thus signal amplitude is linear with concentration, allowing for greater measurement dynamic range. In the first demonstration this technique achieved sub parts per million meter sensitivity in the mid infrared, comparable to the best single pass absorption spectroscopy methods, and also demonstrated for the first time the advantages of dispersion spectroscopy for molecular absorption lines.

Subsequent work on CLaDS has further enhanced the sensitivity by reduction of spurious noise sources due to parasitic optical fringing [19], as well as by optimization of the chirp rate [20], bringing the sensitivity to 0.1 parts per million. Spurious noise due to unwanted molecular species can also be eliminated using Differential Optical Dispersion spectroscopy, a differential CLaDs setup with a carefully prepared or calibrated vapor cell in the reference arm [21]. Simultaneously, work has also been done to enhance the signal amplitude. This is done by using single sideband modulators, which are able to synthesize multi GHz frequency shifts, optimal for air-broadened molecular transitions. This was first done in the near-infrared [22], for which single sideband modulators are easily available. Since SSBs are not available in the mid-infrared, a non-linear difference frequency generation scheme was used to convert SSB modulated near-infrared light to the mid-infrared [23], achieving similar 0.1 parts per million concentration sensitivity.

Heterodyne Phase Sensitive Dispersion Spectroscopy

Heterodyne Phase Sensitive Dispersion Spectroscopy [24] was developed as an alternative dispersion spectroscopy technique with a simpler optical configuration that removes the need to frequency chirp the laser. In this technique, an intensity modulator is used in line with a laser to add amplitude modulations sidebands before entering a vapor cell containing the spectroscopic analyte. As in CLaDS, the sidebands and the carrier experience differential phase shifts corresponding to the dispersion curve around a molecular transition. At the photodetector, the sidebands beat with the carrier, and the demodulation of the beat note recovers the dispersion induced differential phase signal. A minimal configuration for HPSDS is shown in Figure 1.2b below.

Differing from CLaDS, instead of encoding the dispersion induced phase shift onto a laser frequency chirp, it is directly encoded as phase modulation on the beatnote between the sideband pair and the carrier. Rather than chirping across the transition, the laser is swept more slowly, serving only to scan across the transition, without providing a signal enhancement factor. As with CLaDS, the signal size depends on the separation of the sidebands, in this case depending on the intensity modulator drive frequency compared to the width of the transition of interest, typically GHz.

By placing a second optical intensity modulator with a slightly offset drive frequency after the vapor cell, it is possible to mix the GHz sidebands down to MHz, avoiding the GHz bandwidth demodulation required in CLaDS without the sacrificing the signal amplitude.

With this method, HPSDS achieved 10 ppm concentration sensitivity, comparable to that of CLaDS. This is achieved without the need for GHz demodulation or a fast frequency chirp. Similarly to CLaDS, this technique has been extended to the mid infrared [25] using difference frequency generation methods. The availability of intensity modulators at these wavelengths, along with not requiring fast laser frequency chirping has also allowed for direct use of mid [26] and far-infrared sources [27], without constructing an in-house difference frequency scheme.

Applications and Recent Developments

As both CLaDS and HPSDS techniques have matured, current research has focused on applications of dispersion spectroscopy for open path measurements and environmental monitoring. In particular, dispersion spectroscopy is well suited for flame and combustion measurements due to intrinsic immunity to laser power fluctuations caused by thermal radiation and scattering from soot particles [30]. Due to both techniques using FM modulation and demodulation, frequency modulated continuous wave (FMCW) lidar techniques have also been adapted into dispersion spectroscopy. This has allowed simultaneous path length measurement and range detection [31] [32]. Concurrently, using widely tunable Vertical cavity surface emitting lasers (VCSELs), multi-species measurement [26] is possible, opening the door for dispersion spectroscopy for open path and remote sensing of greenhouse gases, which have strong mid-infrared fundamental transitions. These techniques have achieved single ppm sensitivity and sub meter distance precision in measurements of methane plumes [33]. More recently, the technique has also been commercialized as the core technology in a device used for real-time, continuous leak detection at methane plants [34].

1.2 Digital Interferometry

Digital Interferometry (DI) [35] is a laser metrology technique originally developed at the NASA Jet Propulsion Laboratory, but now widely used at the ANU. This technique enables range gated interferometric phase measurements using the correlation of pseudo-random binary sequences (PRBS) modulated onto the optical field. The deterministic nature of PRBS codes allows these interferometric signals to be uniquely time stamped within a single PRBS code length, isolating the desired range-gated signal from a chosen target and enabling rejection of unwanted scattered noise or other cross-talk that leads to signal corruption. This unique range gating and multiplexing capability on a single modulated optical field has the effect of reducing optical complexity, and transferring it to digital signal processing. This is a convenient and cost-effective tradeoff as the processing power available, especially with dedicated FPGAs to perform modulation and demodulation, have grown immensely over the past two decades [36], and is similar in philosophy to techniques such as Deep Modulation Interferometry [37] and machine learning etalon identification and removal [38].

DI was originally developed as a heterodyne technique requiring a local oscillator to recover in-phase and quadrature components of the interference. However, a homodyne variant was subsequently developed. This variant uses an electro-optic modulator along with a quadrature phase shift keying scheme to scan the in-phase and quadrature components of the interference fringe. In doing so, this further reduces optical and mechanical complexity at the expense of more complicated digital signal processing[39].

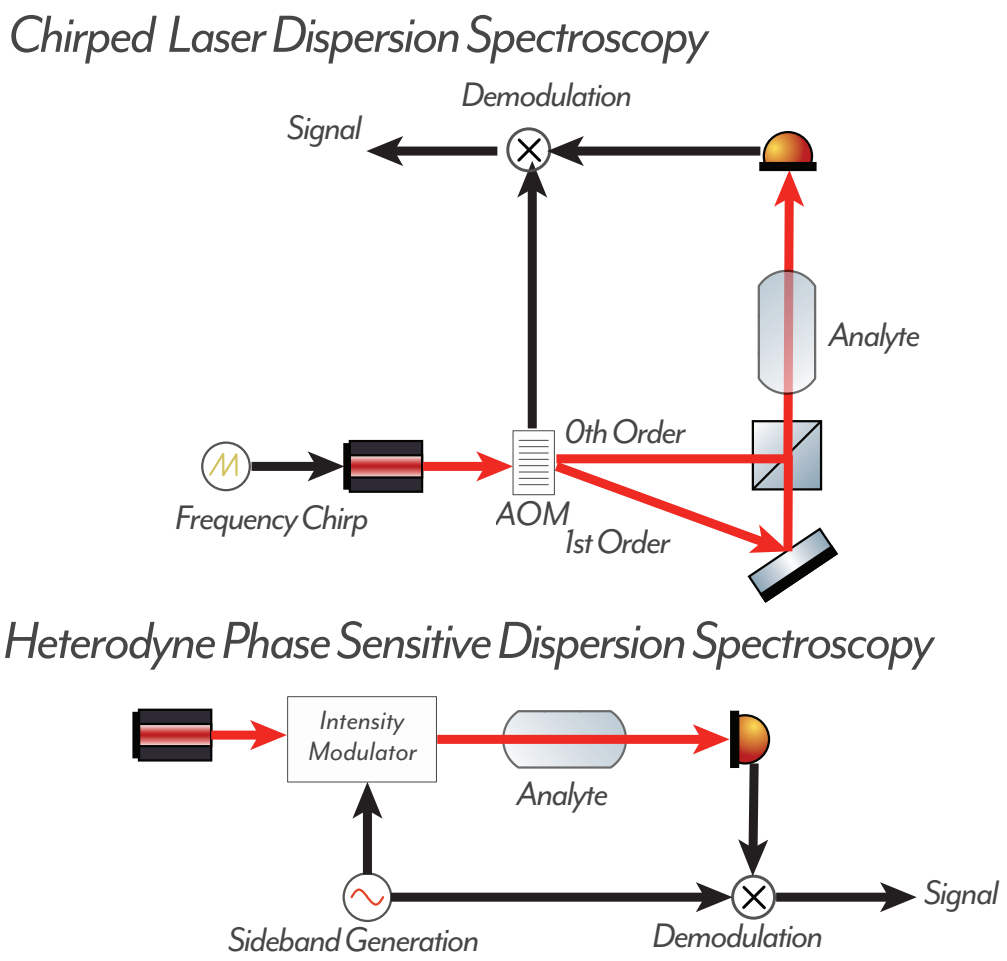

Figure 1.2: A comparison of Chirped laser dispersion spectroscopy and Heterodyne phase sensitive dispersion spectroscopy. Both are minimal configurations, taken from the initial demonstration of these techniques. In CLaDS, the laser is frequency chirped, and then frequency shifted and diffracted by an AOM, forming a defacto beamsplitter. The zeroth order and first order paths are then recombined at a true beamsplitter and then passed through a vapor cell containing the analyte. The shifted and unshifted fields sample the dispersion at different frequencies, leading to a phase shift, which is converted to a frequency shift signal by the laser chirp. The demodulation of the signal is done at the AOM shift frequency. The minimal configuration of HPSDS has a simpler setup. Here, the laser is not chirped, but merely scanned over the transition. The scanned laser is passed through an intensity modulator, which adds frequency sidebands, analogous to the role of the AOM in CLaDS. These sidebands probe the dispersion of the analyte at different frequencies, and then beat with the carrier on the photodetector. By demodulating at the intensity modulator drive frequency, the dispersion induced phase signal is recovered. We emphasize that this figure makes a clear distinction between CLaDS and HPSDS for didactic purposes. Recent methods have muddied the distinction and combined aspects of the two techniques. For example it is now common for the sideband generation in CLaDs to be implemented with EOMS, simplifying the optical setup [22]. Enhancement of the signal has also been achieved through the addition of a heterodyne local oscillator path [28]. In parallel HPSDS schemes have also made use of additional wavelength modulation of the laser [29].

Previous implementations of digital interferometry have relied on its range gating properties to perform displacement measurements at the picometer scale [40], multiplexed phase sensing for the control of optical phased arrays [41], and multi-target acoustic sensing [42]. DI has also been used to characterize phase noise due to optical path length drift [43], Rayleigh backscatter [44, 45], and polarization wander [46] in fiber interferometers.

Of particular relevance to the work in this thesis is DI's current state of development as a well characterized phase extraction technique with the ability reach sub microradian phase noise performance due to its scattering rejection properties. This is required as the dispersion induced phase gas absorption lines in the near infrared is typically only tens of milliradians in amplitude. Furthermore we explore the multiplexing capability of DI for use with multiheterodyne comb based spectroscopic measurements.

1.3 Frequency Comb Spectroscopy

Developing in parallel with dispersion spectroscopy, frequency comb spectroscopy has been an area of intense research interest since the Nobel Prize winning conception and realization of the optical frequency comb [47]. Here, a laser is pulsed at a repetition rate f_{rep}, which is equivalent to a set of discrete frequencies, or a comb in frequency domain. Thus, by referencing the repetition rate of a mode locked laser to an atomic microwave transition, a set of mutually coherent phase locked comb 'teeth' spanning tens of nanometers can be generated. This allows for absorptive, as well as dispersive spectroscopy across broad spectral bandwidths without moving mechanical components. In addition, the traceability of frequency combs to atomic transitions enables the calibration of the spectra to within the absolute accuracy of these standards [48].

The most straightforward application of optical frequency combs to spectroscopy is known as direct frequency comb spectroscopy [49]. Here, a comb line is aligned with the molecular transition of interest, and then the carrier frequency of the pulsed laser is swept across a free spectral range of the comb. The resulting absorption envelope is recorded on a photodetector. This method, however is limited to narrow transitions due to the tuning range of the carrier frequency, and suffers from many of the same problems of absorption spectroscopy.

Alternatively, a dispersive element along with a CCD array can be used to probe the interaction between the comb and the molecular sample [50]. This allows for broader or multiple transitions to be resolved. However, the technique is limited by the resolution of the dispersive optics, as well as the detector array.

Currently, the state of the art and most widely researched technique for frequency comb spectroscopy is dual comb spectroscopy [51]. This is a heterodyne interferometric technique, where a signal comb interrogates a sample, and a reference comb with an FSR offset by a few KHz acts as a local oscillator. The detected interference signal is an RF comb with KHz spacing where each of the RF comb teeth carries information about the amplitude and phase of the molecular transition. Thus dual comb spectroscopy can be used to probe both absorption and dispersion.

Of particular interest in dual comb spectroscopy is ensuring that the two combs possess a high degree of mutual coherence. This can be done using active feedback, stabilizing

the two combs to each other [52], or in feedforward correction of the RF interferograms [53, 54].

1.4 Electro-Optic and Acousto Optic Combs

While frequency combs based on mode locked lasers are the most common, active research is also being done on generation of combs using other techniques that offer inherent mutual coherence between comb teeth. Electro-optic frequency combs are generated using direct phase modulation of a CW laser using Mach Zehnder modulators. These were developed [56] with the aim of offering better mutual coherence for dual comb spectroscopy, and also to increase the flexibility and frequency agility of combs, as mode locked frequency combs are limited in their free spectral range as well as center frequency tunability. Additionally, many of these techniques trade off some absolute frequency accuracy for decreased optical complexity and cost and increased robustness and flexibility, allowing for frequency combs to be used in field-deployable spectroscopic devices [57]. Dual electro-optic comb systems have also been used in a heterodyne interferometer to independently recover both amplitude and phase information for dispersion spectroscopy, as an extension of heterodyne phase sensitive dispersion spectroscopy. In this scheme [24], two electro optic combs with differing comb spacing are generated from a seed laser using an electro-optic modulator in each arm of a Mach Zehnder interferometer. One of the combs are then frequency offset using an acousto optic modulator and passed through a vapor cell before being recombined with the reference comb arm. This results in a flexible, frequency agile comb that samples the vapor cell over multi GHz, but is heterodyned down to MHz frequencies. By using a lock in amplifier, the amplitude and the phase of each of mixed down comb teeth can be recovered to synthesize the spectroscopic signal. This signal retains the parts per million concentration sensitivity of heterodyne phase sensitive dispersion spectroscopy but has the advantage of a much higher laser tuning free optical bandwidth, and the ability to make a single shot spectroscopic measurement.

Although electro-optic frequency combs have become widely adopted for spectroscopy , compared to traditional combs [58], they possess smaller number of comb teeth generated, as well as narrower optical bandwidth. This is due to modulation depth limitations in the signal generators used to drive the electro-optic modulators. Progress has been made to generate higher density electro-optic combs using non-linear supercontinuum generation [59] and pseudo-random bit sequence modulation [55]. However, the bandwidth of the comb is still limited by the bandwidth of the modulators and the signal generators. An example of an electro-optic comb system is depicted in the middle panel of Figure 1.3.

To address this limitation, acousto-optic combs [60] were developed. Here, a comb is generated by placing an acousto-optic modulator within a re-entrant frequency shifting loop. Thus, the comb spacing is set by the acousto-optic frequency shift, and the optical bandwidth is only limited by transits of the frequency shifting loop. This can be boosted to hundreds of comb teeth by inserting an erbium doped fiber amplifier and carefully tuning parameters such as the EDFA gain and loop coupling ratios. An example of an acousto-optic comb system, compared to traditional combs and EOM combs is depicted in the middle panel of Figure 1.3.

This method has been used for molecular gas spectroscopy in the near infrared in a dual comb configuration, where a second comb with a slightly different FSR (on the order

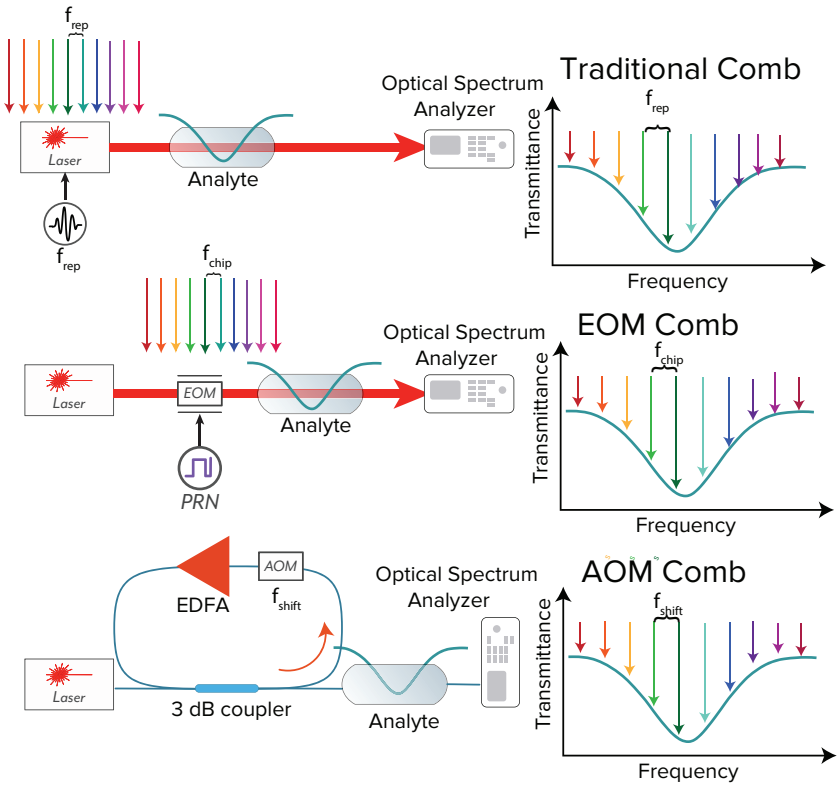

Figure 1.3: A minimal configuration for three types of comb absorption spectroscopy are compared. The traditional comb uses a pulsed, mode locked laser to generate a train of pulses in time domain. This is equivalent to a comb in frequency domain, with the spacing between each of the comb teeth determined by the pulse, or repetition rate f_{rep}. When passed through a vapor cell containing an analyte, the comb spectrum will be amplitude modulated by absorption line, forming an envelope in the transmission spectrum. The Electro-optic (EOM) comb is formed by phase modulating a seed laser, creating frequency sidebands and forming a comb. In recent work [55], a pseudo-random noise (PRN) sequence has been used to achieve spectral flatnesss. Here, the comb spacing is set by the modulation frequency. The Acousto-optic (AOM) comb is formed using a re-entrant delay line containing an AOM. After the seed laser is coupled into the re-entrant delay line, it is frequency shifted by an AOM, creating a frequency sideband. With each transit of the delay line, an adjacent sideband is generated, forming a frequency comb. Here, the comb spacing is set by the AOM frequency.

of KHz) serves as a reference in a Mach-Zehnder Interferometer [60]. This allows the amplitude and phase of the beatnote between the signal comb interrogating a gas cell and the slightly offset reference comb to be read out with relatively modest electronic bandwidth requirements, as the RF comb FSR is merely the KHz offset between the optical combs. Unfortunately, although the two AOM combs are seeded by the same laser, the optical path length in one of the combs will still drift compared to the other, so active phase control within one loop is still required to maintain the mutual coherence condition.

1.5 Thesis Objective and Roadmap

The work presented in this thesis aims to leverage recent developments in digital interferometric techniques for dispersion spectroscopy. As a robust phase sensing technique, it is particularly suited to dispersion spectroscopy, which requires interferometric sensing of milliradian phase signals. As a proof of concept of DI signal extraction and performance, we first demonstrate digital interferometry on a Sagnac interferometer. This is a good testbed for DI as the the inherently balanced arm lengths provide first order frequency noise suppression, but remain sensitive to scattering driven noise. In this balanced configuration, the interferometer achieves an optical phase noise floor of 0.2 µrad $\sqrt{\text{Hz}}$.

Taking advantage of the stability inherent to the Sagnac interferometer, we demonstrate a digitally enhanced homodyne dispersion spectrometer where a vapor cell is inserted into the Sagnac loop, and homodyne digital interferometry is used to extract a spectroscopic signal. The insertion of the vapor cell increases the optical phase noise modestly to 0.8 µrad $\sqrt{\text{Hz}}$. However, this is still sufficient to achieve sub parts-per million concentration sensitivity.

As a capstone experiment, we build a more flexible unidirectional system based around a re-entrant delay line Mach Zehnder interferometer. Using digital interferometry, we track the passes through the delay line and re-synthesize a balanced path length interferometer where common frequency noise is subtracted from the spectroscopic signal. In doing so, we achieve a phase sensitivity of 8 µrad/$\sqrt{\text{Hz}}$, which corresponds to a parts per million concentration sensitivity.

At the time of the writing of this thesis, we use the multiplexing capability of DI to recover up to thirty additional transits of this delay line, in effect forming an acousto-optic frequency comb with thirty teeth. We characterize the RF spectrum of this frequency comb, and recover the amplitude of each of the comb teeth, using an HCN vapor cell as a calibration tool. Finally, we discuss some recent work in digital interferometry that enables greater phase fidelity and lower crosstalk in highly multiplexed systems such as the digital interferometric acousto-optic frequency comb.

1.6 Publications and Patents

Below is a list of peer-reviewed journal publications, conference proceedings and patents resulting from the research undertaken during my PhD program

1.6.1 Journal Publications

- Justin Wong, Chathura P. Bandutunga, Ya Zhang, Malcolm B. Gray, and Jong H. Chow. Digitally enhanced molecular dispersion spectroscopy *Optics Letters* 45, 6290-6293 (2020).
- Justin Wong, Chathura P. Bandutunga, Priya Singh, Malcolm B Gray, Jong H Chow. Molecular Dispersion Spectroscopy Using a Code-Division-Multiplexed Optical Carrier. *Physical Review Applied* 19 4(2023).
- Anika O. Chan, Justin Wong, Paul G. Sibley, Chathura P. Bandutunga. (in press). Narrow-band readout and compression of a single acousto-optic frequency comb using Digitally Enhanced Heterodyne Interferometry. *Optics Express*
- Anneshwa Dey, Paul G. Sibley, Justin Wong, Malcolm B. Gray, and Chathura P. Bandutunga, "Common-mode phase noise suppression with an open-loop differential phasemeter," *Opt. Express* 32, 48276-48288 (2024)
- Anneshwa Dey, Ya Zhang, Justin Wong, Paul G. Sibley, Chathura P. Bandutunga, Malcolm B. Gray, and Jong H. Chow. Algebraic cancellation of inter-channel cross talk in multiplexed heterodyne interferometry *Optics Letters* 46, 5830-5833 (2021)

1.6.2 Conference Proceedings

- J. Wong, C. Bandutunga, M. Gray, and J. Chow, "Dispersion Spectroscopy using a Code Division Multiplexed Re-Entrant Delay Line," in *Optica Sensing Congress 2023 (AIS, FTS, HISE, Sensors, ES)*, Technical Digest Series (Optica Publishing Group, 2023), paper SW3B.5.
- J. Wong, C. Bandutunga, M. Gray, and J. Chow, "Digitally Enhanced Fiber Sagnac Interferometer for Near-Infrared Molecular Dispersion Spectroscopy" in *Frontiers in Optics + Laser Science 2022 (FIO, LS)*, Technical Digest Series (Optica Publishing Group, 2022), paper JTu5A.7.
- J. Wong, C. P. Bandutunga, Y. Zhang, M. B. Gray, and J. H. Chow, "Molecular Gas Sensing in the Near Infrared using Digitally Enhanced Dispersion Spectroscopy," in *OSA Optical Sensors and Sensing Congress 2021 (AIS, FTS, HISE, SENSORS, ES)*, S. Buckley, F. Vanier, S. Shi, K. Walker, I. Coddington, S. Paine, K. Lok Chan, W. Moses, S. Qian, P. Pellegrino, F. Vollmer, G. , J. Jágerská, R. Menzies, L. Emmenegger, and J. Westberg, eds., OSA Technical Digest (Optica Publishing Group, 2021), paper EThA1A.4.
- J. Wong, C. P. Bandutunga, Y. Zhang, M. B. Gray, and J. H. Chow, "Digitally Enhanced Homodyne Dispersion Spectrometer," in *14th Pacific Rim Conference on Lasers and Electro-Optics (CLEO PR 2020)*, OSA Technical Digest (Optica Publishing Group, 2020), paper C6D_4.

1.6.3 Patents

- Systems and methods/processes for Optical Interferometric Sensing A. Dey, C.P. Bandutunga, Y. Zhang, M. B.Gray, J. H. Chow, J. C. T. Wong, P.G. Sibley, Australian Patent Application No. 2022341028. Date Filed: 30 Aug 2022

- Systems and methods for Sagnac Interferometry, A. Dey, C.P. Bandutunga, Y. Zhang, M. B.Gray, J. H. Chow, J. C. T. Wong, P.G. Sibley Australian Patent Application No. 2021332083. Date Filed: 19 Aug 2021
- Systems and methods for optical interferometric sensing, A. Dey, C.P. Bandutunga, Y. Zhang, M. B.Gray, J. H. Chow, J. C. T. Wong, P.G. Sibley, Australian Provisional Patent Application No. 2021902822. Date Filed: 31 Aug 2021

2

Absorption and Dispersion

Any introduction to dispersion spectroscopy must first begin with a treatment of absorption. To that end, we first derive the Beer-Lambert Law. We then convert the Beer-Lambert Law to a form commonly used for molecular spectroscopy, and identify parameters of interest, notably concentration. In the following section of the chapter, using the Kramers-Kronig relations, an absorption lineshape is converted to dispersion (refractive index units). Here, we give a heuristic proof that dispersion scales linearly with concentration. In the final section, the common lineshapes used to model absorption lines are introduced. These absorption lineshapes are then converted to dispersion, and a numeric demonstration of the linearity with concentration is provided.

2.1 Beer-Lambert Law and Absorption

A simple model for the absorption of light through a spectroscopic sample can be constructed by considering the linear change in the intensity of light as it passes through a vapor cell,

$$-\frac{dI_x}{I_x} = \frac{\sigma}{dA} N_g dA dx \tag{2.1}$$

where I is the incident intensity along the x axis, σ is the absorption cross section, N_g is concentration or number density in units of inverse meter cubed, and dA is the cross sectional area of the sample illuminated. We interpret $N_g dA dx$ as the the number of molecules seen by the light beam, and the term $\frac{\sigma}{dA}$ as the probability that a photon will be absorbed by one of the molecules. Therefore, the product gives the change in intensity as light passes through a volume element of the sample. Integrating both sides, and rearranging terms, we obtain

$$\int_{I_0}^{I} -\frac{dI_x}{I} = \int_0^x \frac{\sigma}{dA} N_g dA dx \tag{2.2}$$

$$\ln \frac{I}{I_0} = -\sigma N_g x \tag{2.3}$$

$$I = I_0 e^{-\sigma N_g x} \tag{2.4}$$

This is known as the Beer-Lambert Law. The amount of light absorbed is exponential with the concentration and path length through the absorbing medium. Of course, the absorption is also dependent on the frequency of the incident light. We have neglected this dependence in our initial derivation but we reintroduce it by noting that the absorption cross section term σ depends on the frequency of the incident light, as well as the pressure and temperature of the absorbing medium. This defines a unitless lineshape function $\phi(\nu, P, T)$. As the absorption strength of different absorption lines also vary depending on the geometry of the gas molecules and the associated ro-vibrational modes, we also define a line strength per molecule parameter $S(T)$ where

$$S(T) = \int_{-\infty}^{\infty} \sigma(\nu, P, T) d\nu \tag{2.5}$$

Combining these parameters, we obtain

$$\sigma(\nu, P, T) = S(T)\phi(\nu, P, T) \tag{2.6}$$

We note that this implies that the integral of the lineshape function $\phi(\nu, P, T)$ with respect to frequency is normalized to unity. Thus, the linestrength is convolved with the lineshape function to broaden out the absorption line, where the amount of broadening is determined by the natural linewidth and the pressure and temperature of the gas molecules. To tease out these parameters further, we use the ideal gas law to rewrite the number density N_g as

$$N_g = \frac{p}{k_B T} \tag{2.7}$$

where p is the pressure, k_B is the Boltzmann constant and T is the temperature. Putting these parameters into the Beer-Lambert law defined in Equation 2.4 gives

$$I = I_0 e^{-S(T)\phi(\nu,P,T)\frac{P}{k_B T}x} \tag{2.8}$$

To simplify this expression, it is common to define a parameter α

$$\alpha(\nu, P, T) = \frac{P_0}{k_B T_0} S(T)\phi(\nu, P, T) \tag{2.9}$$

where P_0 and T_0 are standard pressure (1 atm) and temperature (273 Kelvin). Using this parameter, we redefine Equation 2.8 to the following:

$$I = I_0 e^{-\alpha \frac{k_B T_0}{P_0} \frac{P}{k_B T} x} \tag{2.10}$$

$$= I_0 e^{-\alpha C x} \tag{2.11}$$

Where we have defined C, the concentration relative to standard temperature and pressure in air as

$$C = \frac{N_g}{N_0} = \frac{k_B T_0}{P_0} \frac{P}{k_B T} \tag{2.12}$$

Since concentration is dimensionless, we may define its units as parts-per-million, which is the standard used for quantifying the amount of greenhouse or toxic gases in the atmosphere [61]. For in situ measurements of greenhouse gas concentrations, such as in a vapor or flow cell, it is also customary to multiply through by the length of the gas cell to quote a path length concentration in parts per million-meters. As an example calculation, consider a 25 cm gas cell filled with 10 torr of carbon dioxide gas. This gives a parts per million meter figure of 3290 parts per million meter. Thus, by measuring the linecenter depth for a given absorption line, and knowing the concentration, it is possible to measure the maximum absorption coefficient α for each absorption line. Alternatively, by retrieving the absorption coefficient from a spectroscopic database, with a known path length, the gas concentration can be extracted.

From Equation 2.11, the absorption is exponential with concentration. This results in non-linearity of the concentration measurement $\frac{I}{I_0}$. Additionally, any intensity fluctuation will directly couple into the concentration readout as well.

2.2 Absorption to Refractive Index

2.2.1 Kramers Kronig Relations

Any absorption of laser light around a transition is also associated with a change in refractive index, in a phenomemon called anomalous dispersion. This is a general property of all dissipative, resonant systems, and applies to the ro-vibrational resonance of molecules that lead to bands of absorption lines [62]. The size and shape of the refractive index deviation for any given absorption line can be calculated using the Kramers Kronig relations from its absorption coefficient $\alpha(\nu, P, T)$. We begin by defining the Kramers Kronig relations generally for an impulse response of a causal, linear system in the frequency domain $H(\omega)$:

$$H(\omega) = H'(\omega) + H''(\omega) \tag{2.13}$$

where $H'(\omega)$ and $H''(\omega)$ are the real and imaginary parts respectively of the complex valued impulse response. The Kramers Kronig relations state that the real and imaginary parts are related, and can be derived from one another:

$$H'(\omega) = \frac{2}{\pi}\int_0^\infty \frac{\Omega H''(\Omega)}{\omega^2 - \Omega^2} d\Omega \tag{2.14}$$

$$H''(\omega) = -\frac{2\omega}{\pi}\int_0^\infty \frac{\Omega H'(\Omega)}{\omega^2 - \Omega^2} d\Omega \tag{2.15}$$

where Ω is a dummy integration variable. To relate this to a physical system, ie. the interaction of coherent laser light with atoms or molecules, we begin by noting that the electric susceptibility $\chi_e(\omega)$ is the frequency domain impulse response of a molecular or atomic resonance and can be written analogously to our general impulse function $H(\omega)$

$$\tilde{\chi_e}(\omega) = \chi_e'(\omega) + \chi_e''(\omega)$$

We simply replace the H_ω with the susceptibility $\chi_e'(\omega)$ in the Kramers Kronig relations, obtaining

$$\chi_e'(\omega) = \frac{2}{\pi}\int_0^\infty \frac{\Omega \chi_e''(\omega)}{\omega^2 - \Omega^2} d\Omega$$

$$\chi_e''(\omega) = -\frac{2\omega}{\pi}\int_0^\infty \frac{\Omega \chi_e'(\omega)}{\omega^2 - \Omega^2} d\Omega \tag{2.16}$$

We can express these relations in terms of absorption and refractive index by relating the complex refractive index $\tilde{n}$ and susceptibility:

$$\tilde{n} = n_0(\omega) + i\kappa(\omega) = \sqrt{1 + \tilde{\chi_e}(\omega)} \tag{2.17}$$

where $\kappa(\omega)$ is the extinction coefficient. This is a dimensionless quantity that is related to the absorption coefficient α by the following:

$$\kappa = \frac{\alpha\lambda}{4\pi} \tag{2.18}$$

For gases, due to their low molecular density, the complex susceptibility is small($\tilde{\chi_e(\omega)} \lll$ 1). We can therefore use the binomial expansion to approximate the square root:

$$\sqrt{1 + \tilde{\chi_e}(\omega)} \approxeq 1 + \frac{\tilde{\chi_e}(\omega)}{2} = 1 + \frac{\chi_e'(\omega)}{2} + j\frac{\chi_e''(\omega)}{2} \tag{2.19}$$

Grouping the real and complex terms, we isolate the refractive index and the extinction coefficient:

$$n_0(\omega) = 1 + \frac{\chi_e'(\omega)}{2} \tag{2.20}$$

$$\kappa(\omega) = \frac{\chi_e''(\omega)}{2} \tag{2.21}$$

Substituting this into the Kramers Kronig relations for susceptibility given by Equation 2.16, we obtain the relation between refractive index and the extinction coefficient:

$$n_0(\omega) = 1 + \frac{2}{\pi}\int_0^\infty \frac{\Omega\kappa(\Omega)}{\omega^2 - \Omega^2} d\Omega \tag{2.22}$$

Finally, we make the substitution for the extinction coefficient $\kappa(\Omega) = \frac{c}{2\Omega}\alpha$, and obtain an equation that allows us to compute the refractive index profile given an absorption line $\alpha(\omega)$:

$$n_0(\omega) = 1 + \frac{c}{\pi}\int_0^\infty \frac{\alpha(\Omega)}{\omega^2 - \Omega^2} d\Omega \tag{2.23}$$

In general, the Kramers Kronig relations are difficult to use analytically, and are most often computed numerically from absorption data. However, to develop some intuition, we work an example, approximating an absorption line as a square well.

2.2.2 Simple Kramers Kronig Calculation

We define a square well as a linear combination of step functions Θ, with a height λ where the steps occur at the sides of the well ω_1 and ω_2:

$$\kappa(\Omega) = \lambda\Theta(\Omega - \omega_1) - \Theta(\Omega - \omega_2) \tag{2.24}$$

Inserting this expression into the Kramers Kronig relations given in Equation 2.21, we obtain:

$$\begin{aligned} n(\omega) &= 1 + \frac{2}{\pi}\int_0^\infty \frac{\lambda\left[\Theta\left(\Omega - \omega_1\right) - \Theta\left(\Omega - \omega_2\right)\right]\Omega}{\Omega^2 - \omega^2} d\Omega \\ &= 1 + \frac{2\lambda}{\pi}\int_{\omega_1}^\infty \frac{\Omega}{\Omega^2 - \omega^2} d\Omega - \frac{2\lambda}{\pi} P\int_{\omega_2}^\infty \frac{\Omega}{\Omega^2 - \omega^2} d\Omega \end{aligned} \tag{2.25}$$

where we have used the integration properties of step functions to simplify the integral and redefine the integration limits. Taking the antiderivative of the integrand, we obtain:

$$\begin{aligned} n(\omega) &= 1 + \frac{2\lambda}{\pi}\left[\frac{1}{2}\ln\left(\left|\Omega^2 - \omega^2\right|\right)\right]_{\omega_1}^\infty - \frac{2\lambda}{\pi}\left[\frac{1}{2}\ln\left(\left|\Omega^2 - \omega^2\right|\right)\right]_{\omega_2}^\infty \\ &= 1 + \frac{\lambda}{\pi}\left[\ln\left(\left|\omega_2^2 - \omega^2\right|\right) - \ln\left(\left|\omega_1^2 - \omega^2\right|\right)\right] \end{aligned} \tag{2.26}$$

Plotting the square well and its Kramers-Kronig transform in Figure 2.1, we see the general shape of anomalous dispersion for an absorption line. At frequencies below the absorption linecenter, there is a sharp rise in the refractive index, indicating a phase lag between the driving frequency and the resonance. At the center of the absorption line, the refractive index is 1. Physically, this means that the resonance is completely in-phase with the driver of the oscillation at the linecenter. At frequencies greater than the resonance, there is a phase-advance compared to the resonance, resulting in a refractive index less than 1. Implicit within this behavior is the causality of the resonant system.

Although the square well is a highly simplified model of an absorption line, the general characteristics and shape of its Kramers-Kronig transform will apply for physical absorption lines as well.

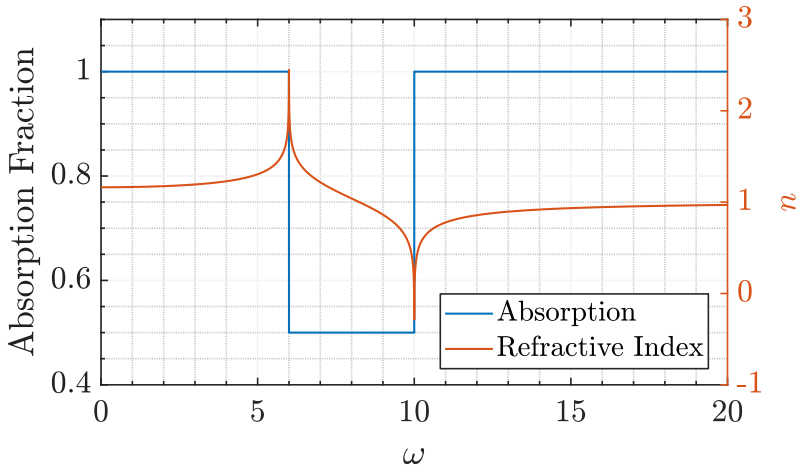

Figure 2.1: A square well transmission spectrum and its associated phase response, calculated analytically using the Kramers Kronig transform is plotted. The normalized depth of the absorption line is 0.5, and the units of refractive index are plotted on the right axis.

2.2.3 Dispersion from the Hilbert Transform

Practically speaking, it is very difficult to calculate analytically the refractive index profile from absorption line data. Typically, the calculation is done numerically on a computer via the evaluation of the Kramers Kronig integral. This is computationally quite expensive, as it requires piecewise evaluation of the integrand and summing of the integral. However, a more recent method [63] uses the Hilbert Transform. Since the Hilbert Transform is included in most numerical signal processing packages and leverages the Fast Fourier transform, it allows a computational time saving of 4 orders of magnitude compared to evaluating the Kramers Kronig integral directly. The Hilbert transform is defined as the following:

$$\hat{H}(\omega) = \frac{1}{\pi} \int_{-\infty}^{\infty} \frac{H(\Omega)}{\omega - \Omega} d\Omega \tag{2.27}$$

At a glance, it is easy to see that this equation resembles the form of the Kramers Kronig relations. In fact, it is an intermediate form in the derivation of the Kramers Kronig relations, and it can be proven that real and imaginary parts of the complex susceptibility $\chi_e'(\omega)$ and $\chi_e''(\omega)$ are also Hilbert Transform pairs [63]. Thus, knowing the imaginary part

of the complex susceptibility χ_e'' (found from absorption), the real component related to dispersion can be found.

To convert absorption data to imaginary susceptibility, we make use of the definition of the extinction coefficient given in Equation 2.18 $\kappa(\Omega) = \frac{\alpha\lambda}{4\pi}$, Equation 2.21 and the Beer-Lambert law.

We begin by isolating the absorption strength concentration product αC from the Beer-Lambert Law given in 2.11, where we have divided through by incident intensity to obtain a normalized transmitted power, and defined the length L as the optical path length:

$$T(\omega) = \frac{I}{I_0} = e^{-\alpha C L} \tag{2.28}$$

We proceed by taking the natural log of the transmitted power, and then dividing by optical path length L:

$$\alpha C = \frac{\ln T(\omega)}{L} \tag{2.29}$$

Next, we divide both sides by the wavevector of the incident light $k = 2\pi/\lambda$, and then make use of Equation 2.18 to obtain the extinction coefficient κ. Since concentration is a dimensionless factor we have also absorbed the concentration C into the term, with the subscript denoting that κ_C is an extensive variable dependent on concentration

$$\kappa_C(\omega) = \frac{\ln T(\omega)}{2kL} \tag{2.30}$$

Finally, from Equation 2.21, the extinction coefficient is related to the susceptibility by a factor of 2:

$$\chi_e'' = 2\kappa_C = \frac{\ln T(\omega)}{kL} \tag{2.31}$$

Armed with the imaginary susceptibility, we then take the Hilbert transform to convert to the real susceptibility:

$$\chi_e' = \hat{H}\chi_e'' \tag{2.32}$$

Finally, we use Equation 2.17 to obtain the refractive index, pulling the concentration C that we absorbed earlier back out of the real susceptibility:

$$n = \sqrt{1 + C\chi_e'} \tag{2.33}$$

We can show heuristically from the above calculation that the refractive index is now linear with concentration. This can be seen by the natural log operation in Equation 2.29 'undoing' the exponential equation to retrieve imaginary susceptibility, a parameter that is linear with concentration. Proceeding through the calculation, the Hilbert transform is a linear operator. Thus, the real susceptibility is also linear with concentration. The

square root term in Equation 2.33 is **not** a linear operation. However, using the dilute media approximation (valid for organic molecules) [64], where the susceptibility is much smaller than 1, we may use the binomial expansion to linearize the square root:

$$n \approx 1 + \frac{C\chi_e'}{2} \tag{2.34}$$

Therefore, the refractive index n is linear with concentration. Experimentally, this means that measuring any change in the refractive index of an analyte yields a direct linear relationship with the analyte concentration.

2.2.4 Spectral Lines and Broadening

Lorentzian Lines

The natural lineshape of an atomic or molecular transition is a Lorentzian. Thus, as a first step towards modelling a spectral line and its dispersion, we examine Lorentzian lines. This is a quantum mechanical effect, arising from the finite lifetime of excited states due to spontaneous emission. From the Heisenberg uncertainty principle, we know that $\Delta E \Delta t \geq h$. Therefore, an uncertainty, or finite lifetime of an excited state will also give rise to an uncertainty in energy, or a spread of frequencies over which absorption occurs. This is the natural linewidth of atomic or molecular transitions.

This natural linewidth of molecular transitions can be approached via Doppler free spectroscopy. However, for the purposes of this thesis, which discusses the application of spectroscopy to large ensembles of molecules at relatively high pressures, the linewidth is dominated by pressure or collisional broadening.

Pressure broadening arises from the collision of molecules, causing perturbations in the energy levels of the molecules. The collision mechanism reduces the lifetime (time uncertainty) of the excited states, thus causing a larger spread of energies over which absorption occurs. Thus, the amount of broadening increases with collision rate, which is in turn dependent on the molecular cross section and the number density of molecules. For a sealed, rigid walled vapor cell (fixed volume and moles), kept at a constant temperature (fixed temperature), this implies through the ideal gas law that the broadened width is dependent on the pressure inside the vapor cell.

Pressure broadening results in a Lorentzian spectral lineshape $T_L(\omega)$ of the form:

$$T_L(\omega) = 1 - \alpha_{max} \frac{\omega_L}{\omega_L^2 + (\omega - \omega_c)^2} \tag{2.35}$$

where α_{max} is the peak absorption fraction determined from the Beer-Lambert Law, ω_L is the Lorentzian half linewidth, and ω_c is the center frequency of the transition. We have also normalized the absorption lineshape to 1 and expressed it in the form of a transmission spectrum. This allows us to directly insert the transmission spectrum into Equation 2.30 to immediately calculate the anomalous dispersion using the Hilbert Transform.

The key parameter for the Lorentzian lineshape is the half linewidth. Typically, for most molecular absorption lines, it is difficult to calculate this analytically as the interaction

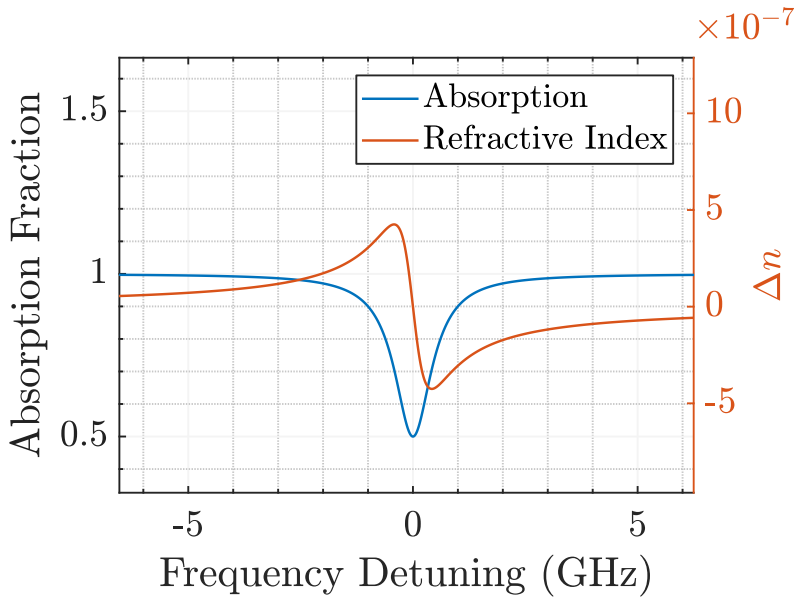

Figure 2.2: The Lorentzian lineshape in transmission for an absorption line with a normalized depth of 0.5 over 10 cm of optical path length and a linewidth of 1 GHz is plotted. The refractive index variation is also computed using the Kramers Kronig relations.

cross section between molecules is affected by long range and second order dipole interactions [65].

Instead, Lorentzian linewidth for molecules is usually determined via consulting a table of pressure broadening coefficients for each absorption line [66], which are generally quoted in MHz/Torr. For most molecules, this broadening coefficient is tens of MHz/torr. At standard temperature and pressure, this results in linewidths on the order of several GHz. As an example, in Figure 2.2 we plot a pressure broadened Lorentzian spectral line with a width of 0.5 GHz and a peak absorption of 0.5. The dispersion profile associated with the Lorentzian spectral line into its is also plotted in Figure 2.2. This was computed using the Hilbert transform method described in the previous section.

The dispersion profile plotted in Figure 2.2 is qualitatively similar in shape to the photographic interferogram obtained by the hook method, reproduced in Chapter 1, Figure 1.1. The two characteristic hooks make up the wings of the dispersion profile. Around the linecenter (-0.5 GHz to 0.5 GHz here), the dispersion profile is obscured in the hook method, as the phase slope is greater than the diffraction grating spectral resolution or CCD spatial resolution, hence the two hooks appear discontinuous.

Doppler Broadening

At higher temperatures and low pressures, the Lorentzian lineshape produced by pressure broadening is not sufficient to approximate a spectral line. This is due to the dominance of an effect known as Doppler broadening [67]. Doppler broadening occurs due to the Doppler shift in the frequency seen by the absorbing molecule. This is dependent on the velocity distribution of the molecules in the ensemble given by the Maxwell Boltzmann distribution:

$$N(v_z)dv_z = N_T\sqrt{\frac{m}{2\pi k_B T}}\exp\left\{-\frac{mv_z^2}{2k_B T}\right\}dv_z \tag{2.36}$$

where the expression gives the number of molecules with mass m and temperature T distributed in the range $[v_z, v_z + dv_z]$. We can relate the velocity of the molecules to the Doppler shift using the standard Doppler shift equation:

$$\frac{\nu - \nu_0}{v_0} = v_z/c \tag{2.37}$$

Inserting Eq. 2.37 into, the Maxwell Boltzmann distribution, we obtain a Gaussian lineshape $\phi(\nu, T)$:

$$\phi(\nu, T) \propto \exp\left\{-\left(\frac{v - v_0}{\sigma_D}\right)^2\right\} \tag{2.38}$$

where we have assumed that the number of molecules between $[v_z, v_z + dv_z]$ corresponds to the amount of light absorbed between $[\nu, \nu + d\nu]$. The Gaussian standard deviation σ_D expanded is:

$$\sigma_D = \nu_0\sqrt{\frac{2k_B T}{mc^2}} \tag{2.39}$$

As the temperature of the molecules increase, the molecules will have a broader distribution of speeds, and thus a wider spread of frequencies over which they absorb.

We can also relate the standard deviation to the Gaussian full width half maximum ω_G:

$$\begin{aligned}\omega_G &= 2\sigma_D\sqrt{\ln 2} \\ &= \nu_0\sqrt{\frac{8k_B T \ln 2}{mc^2}}\end{aligned} \tag{2.40}$$

In order to match the transmission equation and lineshape given in Equation 2.35, we also normalize the depth of the Gaussian lineshape:

$$T_G(\omega) = 1 - \alpha_{max}\exp\left\{-\left(\frac{\omega - \omega_c}{2\pi\sigma_D}\right)^2\right\} \tag{2.41}$$

To show the difference in the lineshape, we also plot the depth normalized Doppler and pressure broadening transmission spectra in Figure 2.3.

As an example calculation to give a sense of the order of magnitude for Doppler broadening of small molecules transitions at room temperature, we use a molecule of interest in this thesis: HCN. With a molar mass of 27 g/mol, at 298 degrees kelvin, and around 1550 nm,

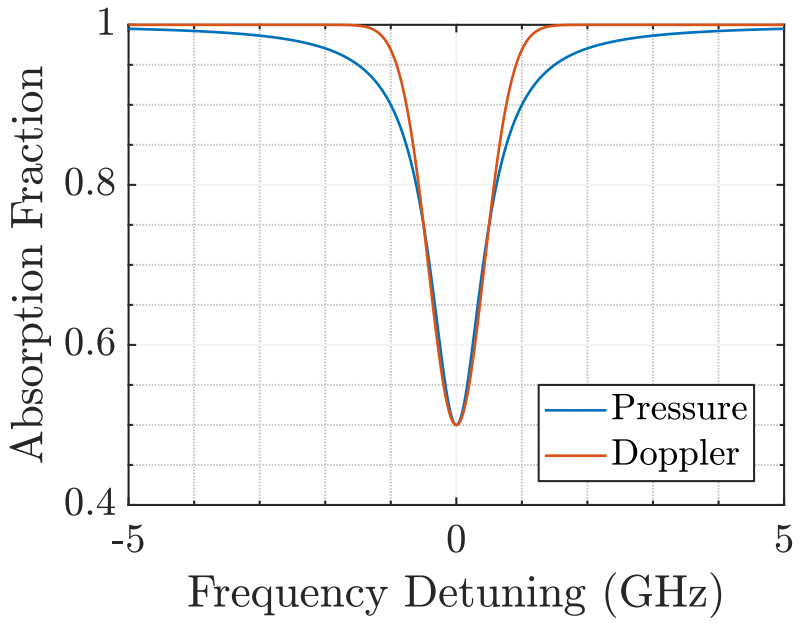

Figure 2.3: The normalized Lorentzian and Gaussian lineshape in transmission for an absorption line with a normalized depth of 0.5 over 10 cm of optical path length and a linewidth of 1 GHz is plotted.

inserting this into Equation 2.40, and converting from molar mass to unit mass, gives a Gaussian full width half maximum of 0.32 GHz.

Voigt Profile

When the Doppler broadening and collisional broadening linewidths are of the same order, neither the Gaussian nor the Lorentzian lineshapes dominate. For most small molecules at standard temperature, this regime occurs at low pressures(<100 torr), such as can be found in a vapor cell. As an example, for Hydrogen Cyanide (HCN) at room temperature, the collisional broadening linewidth for the P branch lines are ≈ 800 MHz [66], and the Doppler linewidth is 380 MHz, In this case, the Doppler broadening and collisional broadening lineshapes must be convolved to produce what is known as the Voigt profile. The convolution is used as the Doppler and collisional broadening processes are treated as independent, to first order [68]. We can write an expression for the Voigt profile in transmission as the convolution between the Gaussian and Lorentzian lineshapes defined in Equations 2.41 and 2.35 :

$$T_V(\omega) = T_L(\omega) \circledast T_G(\omega) \tag{2.42}$$

$$= \left[1 - \alpha_{max} \frac{\omega_L^2}{\omega_L^2 + (\omega - \omega_c)^2}\right] \circledast \left[1 - \alpha_{max} \exp\left\{-\left(\frac{\omega - \omega_c}{2\pi\sigma_D}\right)^2\right\}\right] \tag{2.43}$$

where α_{max} is the maximum normalized depth of the absorption line. This lineshape is plotted in Fig. 2.4 below:

. To illustrate the difference between the three line profiles, we have set the linewidth of the collisional and Doppler broadened lines equal to 1 GHz and the Doppler and collisional

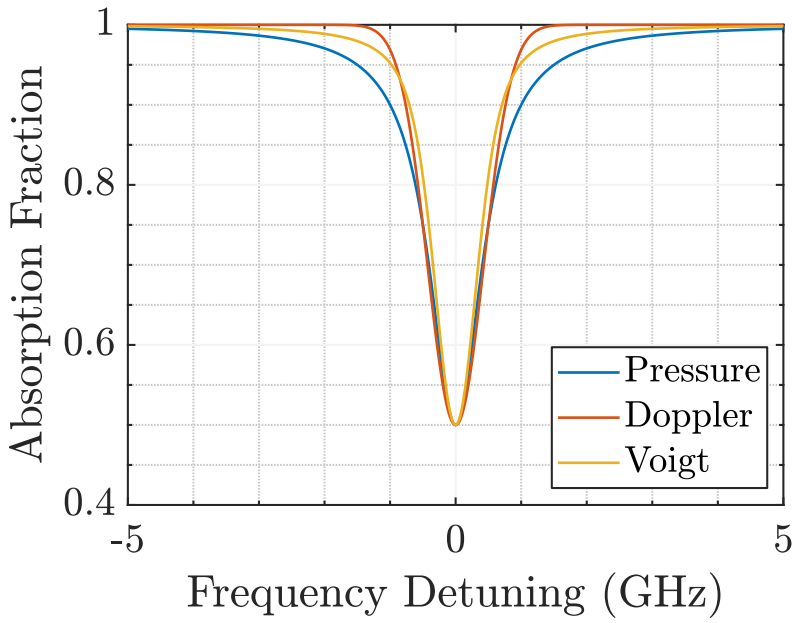

Figure 2.4: The pressure and Doppler broadening linewidths are 1 GHz. For the Voigt profile, the collisional and Doppler broadening contributions are both 0.5 GHz. The values were chosen such that the Voigt profile linewidth is approximately equal to both the Doppler and collisional broadening linewidths. This is to illustrate the qualitative differences between the three lineshapes.

components of the Voigt profile to be 0.5 GHz. We see that the Voigt profile has a lineshape that is qualitatively intermediate between pressure and Doppler broadening lineshapes at the wings of the line. Using the Hilbert transform recipe outlined in Section 2.2.3, where $T(\omega)$ are the absorption lineshapes, we can finally, can generate a dispersion lineshape associated with the Voigt line. Applying the same recipe for the Gaussian and Lorentzian profiles separately, we plot the three dispersion lineshapes associated with the lineshapes in Figure 2.5 below:

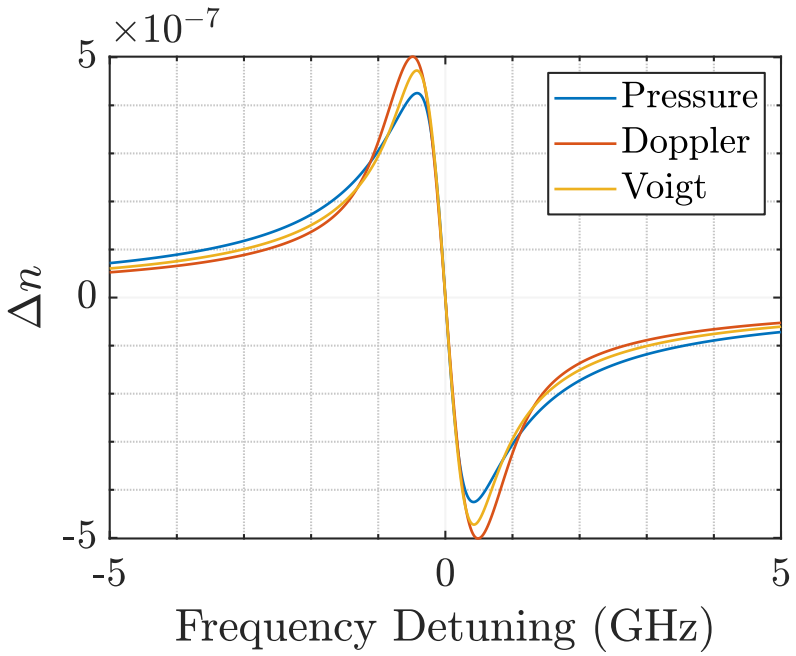

Figure 2.5: The dispersion lines associated with the absorption lines shown in Figure 2.4 are plotted here. The difference in amplitude of the refractive index deviation is due to the difference in the wings of the Doppler and pressure lines. This is because the Kramers-Kronig transfrom requires an integration of the absorption profile from negative infinity to infinity.

Area Normalized Profiles

In the above discussion of the three spectroscopic absorption lineshapes, and their dispersion equivalents, we have used a depth normalization scheme in order to better show the qualitative differences between the lineshapes. In this scheme, the maximum absorption α_{max} is held constant across the three lineshapes, However, the convention in spectroscopy is to normalize the area underneath the absorption lines. By doing so, parameters intrinsic to the line, such as concentration, and α are held constant. This is because the energy associated with a particular transition is fixed, and the broadening mechanisms merely distribute this energy in different ways. However, by normalizing to the area, the line depth is free to vary. This can be seen from equation 2.29, where $T(\omega)$ and C vary proportionally.

We now proceed with a derivation of the area normalized absorption line profiles. The area normalized factors for the Lorentzian and Gaussian broadened lineshapes are given below:

$$T_L^{\text{norm}}(\omega) = 1 - \frac{1}{2\pi}\frac{\omega_L}{\omega_L^2 + (\omega - \omega_c)^2} \tag{2.44}$$

$$T_G^{\text{norm}}(\omega) = 1 - \frac{1}{\sigma_D\sqrt{2\pi}}\exp\left\{-\left(\frac{\omega - \omega_c}{2\pi\sigma_D}\right)^2\right\} \tag{2.45}$$

where we note that these are equations 2.35 and 2.41 multiplied by normalization factors. These normalization factors ensure that integrals of the lineshapes from negative to posi-

tive infinity equal to 1. The normalized Voigt lineshape is then obtained using the usual method of convolving the Lorentzian and Gaussian profiles:

$$T_V^{\text{norm}}(\omega) = T_L^{\text{norm}}(\omega) \circledast T_G^{\text{norm}}(\omega) \tag{2.46}$$

Because the convolution of two area normalized functions is also normalized, this implies that the resulting Voigt profile is normalized. The linewidth of the resulting Voigt lineshape is approximated by a function of the Gaussian and Lorentzian linewidths [69]. Using the Hilbert Transform recipe again, as outlined in Section 2.2.3, we can also obtain the dispersion profiles associated with these absorption lines. These are plotted, along with corresponding absorption profiles in Figure 2.6 below:

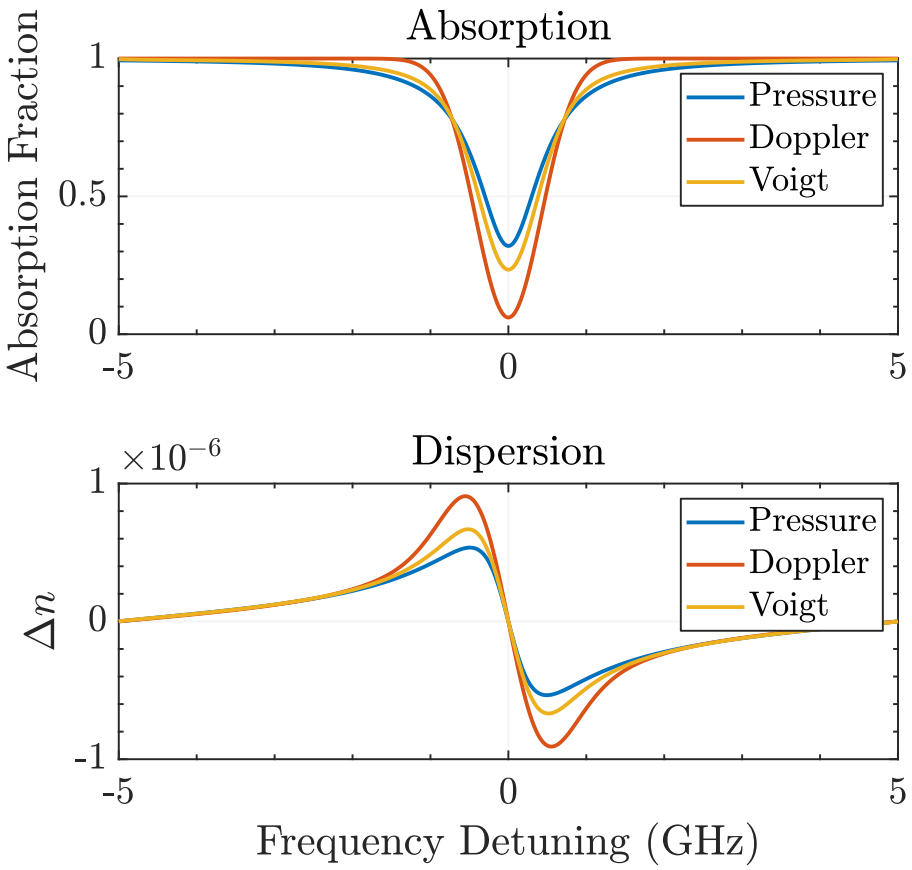

Figure 2.6: The normalized Lorentzian pressure broadening, Gaussian Doppler broadening, and Voigt absorption lineshapes are plotted in the upper subbplot. Their corresponding dispersion profiles are plotted in the lower subplot. The absorption lines all have a linewidth of 1 GHz. For the Voigt line, the pressure and Doppler broadening contributions f_L and f_D have been chosen to be equal. Using the approximation given by Kielkopf [69], we calculate that $f_L = f_D = 611$ MHz ensures that the Voigt linewidth is also 1 GHz. The maximum absorption depth varies between the three lineshapes, with the Lorentzian pressure broadening line being the shallowest. This is because more of the transition energy has been distributed to the broad wings of the Lorentzian, whereas the Gaussian Doppler broadening line has most of its energy distributed within $3\sigma_D$.

Numerical Demonstration of Concentration Linearity

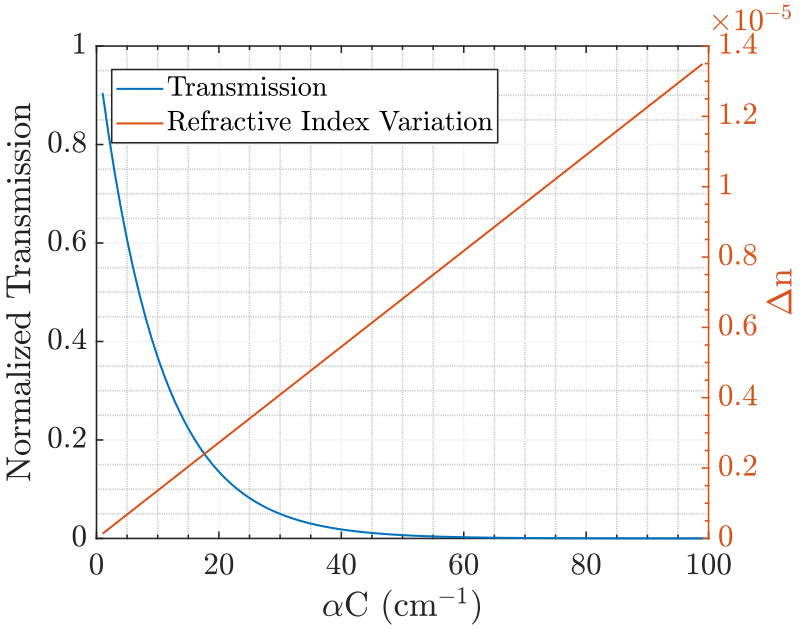

Figure 2.7: The simulated transmission through a vapor cell is plotted for a range of αC. The transmission through the vapor cell is decreases exponentially with increasing concentration, as required by the Beer-Lambert Law. However, the refractive index variation remains linear as concentration increases.

Using the Voigt line as a spectroscopic model, we numerically extract the spectroscopic parameter most relevant to this thesis: concentration. Although we had earlier given a heuristic proof of the linearity of dispersion with concentration, we can use the simulated anomalous dispersion signal to provide a numerical demonstration. In Figure 2.7, we have plotted on the left axis the Beer-Lambert law for the absorption peak, or transmission minimum $\alpha_{max} = \exp(-\alpha CL)$, and the maximum refractive index deviation on the right axis. This was done for a range of αC, with the length L held constant. The refractive index deviation is computed using the Hilbert transform of Voigt profiles calculated from the range of αC values.

From Figure 2.7, we see that the refractive index variation is zero at zero concentration. This leads to a zero-baseline signal, a key advantage of dispersion spectroscopy. By contrast, at zero concentration, the transmission is maximized, leading to a high baseline signal that would have to be subtracted out.

2.3 Summary

This chapter has introduced the basic spectroscopic terminology required for understanding dispersion spectroscopy, starting from a derivation of the Beer-Lambert law, and the identification of the exponential dependence of absorption on the concentration. The Kramers Kronig relations are also applied to derive anomalous dispersion from arbitrary absorption lines. Finally, the linearity of an anomalous dispersion signal with concentration is shown both heuristically and using a numerical model. In the next chapter, we will relate the anomalous dispersion to phase, and provide an introduction to the measurement of this phase using interferometry.

3 Phase Extraction

3.1 Introduction

In the previous chapter, we derived the anomalous dispersion lineshape for a molecular absorption line. The size of the refractive index deviation is small, only 1×10^{-6} refractive index units for an absorption line with a depth of 0.5. In order to detect such a small change in refractive index, a phase sensitive measurement technique is required. For dispersion spectroscopy, we obtain the phase shift from the refractive index using this Equation:

$$\Delta\phi(\omega) = \frac{n(\omega)\omega L}{c} \tag{3.1}$$

where ω is the angular frequency, $n(\omega)$ is the refractive index, and L is the optical path length. For a refractive index profile with a deviation on the order of 10^{-6} at 1550 nm, through an optical path length L of 10 cm, this works out to a maximum phase shift of 0.2 radians. In this chapter, we discuss interferometry, a method for resolving these optical phase shifts with sub-microradian precision. We also discuss several optical architectures for interferometry, including the Sagnac interferometer, comparing its inherent stability to that of a traditional two-beam interferometer. However, the stability of the Sagnac interferometer also makes measuring dispersion challenging. We address this in subsequent chapters.

Finally, we will introduce an interferometric method called digital interferometry that underpins the phase extraction schemes used in this thesis, allowing for the multiplexed spectroscopic measurements performed in Chapter 6. We end the chapter by motivating Digitally Enhanced Homodyne Interferometry, a more specialized form of DI that is required by the Sagnac architecture.

3.2 Two Beam Interferometry

3.2.1 Homodyne Interferometer

Interferometry is the basis of the dispersion spectroscopy technique, as dispersion is ultimately measured through optical phase. As the simplest configuration, let us first consider

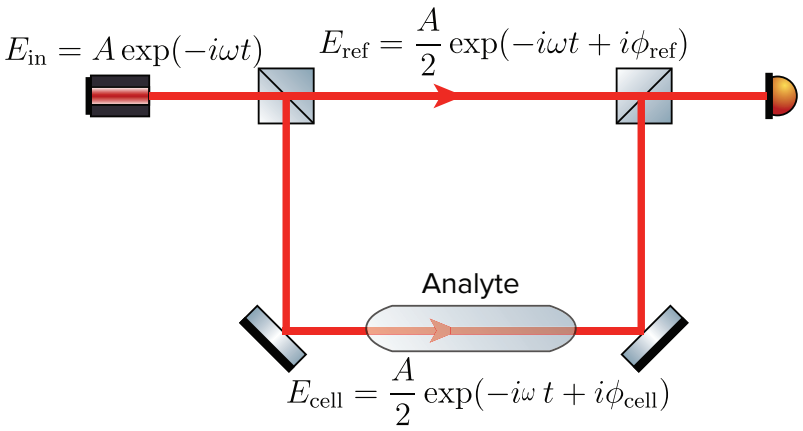

Figure 3.1: The input field $E_{in} = A\exp(-i\omega t)$ is split into two paths by the input beamsplitter. The reference (top) path picks up a phase ϕ_{ref}. The bottom path goes through a vapor cell and picks up a a phase ϕ_{cell}.

a two-beam interferometer. An input optical field can be expressed as the complex exponential:

$$E_{\text{in}} = A\exp(-i\omega t) \tag{3.2}$$

where ω is the optical frequency and A is the amplitude. The field is split by a beamsplitter into a reference path and a signal path, which we have denoted in Figure 3.1 below:

At the beamsplitter, the two fields interfere, yielding the superposition field at the photodetector E_{pd}:

$$\begin{aligned} E_{\text{pd}} &= E_{\text{ref}} + E_{\text{cell}} && (3.3)\\ &= \frac{A}{2}\exp(-i\omega t + i\phi_{\text{ref}}) + \frac{A}{2}\exp(-i\omega t + i\phi_{\text{cell}}) && (3.4) \end{aligned}$$

To calculate the power incident on the photodetector, we multiply E_{pd} by its complex conjugate:

$$\begin{aligned} P &= E_{\text{pd}}E^*_{\text{pd}} && (3.5)\\ &= \frac{A^2}{4}[1 + \cos(\phi_{\text{cell}} - \phi_{\text{ref}})] && (3.6)\\ &= \frac{P_{\text{in}}}{4}[1 + \cos(\phi_{\text{cell}} - \phi_{\text{ref}})] && (3.7) \end{aligned}$$

Thus, there is a DC term with optical power of $\frac{P_{\text{in}}}{4}$ and a term that depends on the phase difference between the cell and reference path. We can insert Equation 3.1 into this expression to obtain an expression for the minimal interferometer configuration to extract a spectroscopic signal through measuring dispersion induced phase shift:

$$P(\omega) = \frac{P_{\text{in}}}{4}\left\{1 + \cos\left[\frac{n(\omega)\omega L}{c}\right]\right\} \tag{3.8}$$

Therefore, by sweeping the frequency of the incident optical field over the transition, a change in optical power can be recorded at the photodetector. However, for a typical dispersion signal on the order of 0.1 radian in phase, this only corresponds to a change in optical power on the order of one percent.

3.2.2 Heterodyne Interferometry

Heterodyne interferometry offers a phase sensitive method to extract the dispersion induced phase shift directly. In this scheme, an acousto-optic modulator, or alternate frequency shifting method is used to shift the frequency of the optical field in one of the interferometer arms:

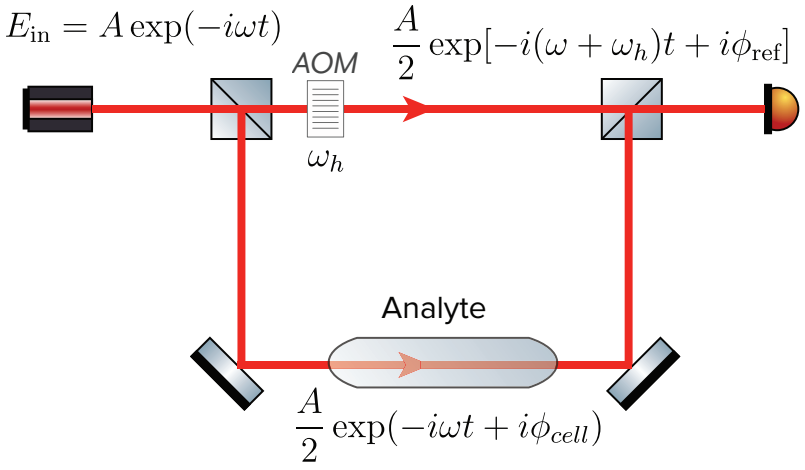

Figure 3.2: The input field $E_{\text{in}} = A\exp(-i\omega t)$ is split into two paths by the input beamsplitter. The field in the reference (top) path picks up a phase ϕ_{ref} and also a frequency shift ω_h from the acousto-optic modulator. The bottom path goes through a vapor cell and picks up a a phase ϕ_{cell}.

The field calculation for a heterodyne interferometer is similar to that of the homodyne interferometer, modulo a frequency shift ω_h in the optical fields of one of the arms (here we have chosen the reference arm):

$$E_{\text{pd}} = E_{\text{ref}} + E_{\text{cell}} \tag{3.9}$$

$$= \frac{A}{2}\exp[-i(\omega+\omega_h)t + i\phi_{\text{ref}}] + \frac{A}{2}\exp(-i\omega t + i\phi_{\text{cell}}) \tag{3.10}$$

At the photodetector, the complex conjugate squared is taken, yielding again two terms:

$$P(\omega) = E_{\text{pd}} E_{\text{pd}}^{*} \tag{3.11}$$
$$= \frac{A^2}{4}[1 + \cos(\omega_h t + \phi_{\text{cell}} - \phi_{\text{ref}})] \tag{3.12}$$
$$= \frac{P_{\text{in}}}{4}[1 + \cos(\omega_h t + \phi_{\text{cell}} - \phi_{\text{ref}})] \tag{3.13}$$
$$= \frac{P_{\text{in}}}{4}\left\{1 + \cos\left[\omega_h t + \frac{n(\omega)\omega L}{c}\right]\right\} \tag{3.14}$$

Here, we see that the dispersion induced phase is encoded on a carrier frequency, ω_h. In order to extract this phase, a method called lock in detection and IQ demodulation is applied. Lock in detection is used in order to isolate only the phase of the carrier in a narrow band around the heterodyne frequency, rejecting other frequency components that may introduce perturbing sources of phase noise. The procedure for lock-in-detection begins by multiplying the photodetector output with an in-phase (cosine) and quadrature (sine) local oscillator at the heterodyne frequency:

$$V_{\text{mix,I}} \propto \frac{P_{\text{in}}}{4}\left\{1 + \cos\left[\omega_h t + \frac{n(\omega)\omega L}{c}\right]\right\} \times \cos(\omega_h t) \tag{3.15}$$
$$= \frac{V_{\text{PD}}}{4}\cos(\omega_h t) + \frac{V_{\text{PD}}}{8}\cos\left[2\omega_h t + \frac{n(\omega)\omega L}{c}\right] + \frac{V_{\text{PD}}}{8}\cos\frac{n(\omega)\omega L}{c}$$
$$V_{\text{mix,Q}} \propto \frac{P_{\text{in}}}{4}\left\{1 + \cos\left[\omega_h t + \frac{n(\omega)\omega L}{c}\right]\right\} \times \sin(\omega_h t) \tag{3.16}$$
$$= \frac{V_{\text{PD}}}{4}\sin(\omega_h t) + \frac{V_{\text{PD}}}{8}\sin\left[2\omega_h t + \frac{n(\omega)\omega L}{c}\right] - \frac{V_{\text{PD}}}{8}\sin\frac{n(\omega)\omega L}{c}$$

where post-photodetection, the optical power has been converted to units of volts. After mixing with the local oscillator, there are three frequencies present in both the in-phase (I) and quadrature (Q) components: $\omega_h, 2\omega_h$, and zero(baseband). Since we are only interested in the dispersion induced phase-shift $n(\omega)\omega L/c$, now at DC, we apply a low-pass filter with a corner frequency $f_c << \omega_h$ to $V_{\text{mix,I}}$ and $V_{\text{mix,Q}}$. This removes the non-dc terms, and we are left with:

$$V_{\text{mix,I}} = \frac{V_{\text{PD}}}{8}\cos\frac{n(\omega)\omega L}{c} \tag{3.17}$$
$$V_{\text{mix,Q}} = \frac{V_{\text{PD}}}{8}\sin\frac{n(\omega)\omega L}{c}$$

Finally, we perform an arctangent operation to recover the dispersion induced phase:

$$\Delta\phi = \arctan\left[\frac{V_{\text{mix,Q}}}{V_{\text{mix,I}}}\right] = \frac{n(\omega)\omega L}{c} \tag{3.18}$$

This two-argument arctangent can be performed efficiently on digital signal processing hardware using the CORDIC (coordinate rotation digital computer) algorithm, or in post processing of the in phase and quadrature components. While this scheme may seem more complicated, in addition to noise rejection, it offers two key advantages compared to homodyne detection. Firstly, the phase is extracted without phase ambiguity, as the four quadrant arctangent typically used for heterodyne interferometry accounts for all four quadrants of the phase plane. This allows more robust tracking of large phase dynamics, lowering the chance of cycle slips. In the case of homodyne interferometry, as phase is the sole argument of the cosine function, a 2π phase ambiguity is possible, and either higher bandwidth phase tracking, or post processing must be used to eliminate cycle slips.

Additionally, the small signal linearity of the interferometer response is dependent on the bias point of the interferometer. Thus, in order to recover a linear dispersion induced phase signal (which is typically small compared to 2π radians of phase), the interferometer would have to be biased at the quadrature point via either arm locking or frequency stabilization of the laser source.

3.2.3 Sagnac Interferometers

An alternative interferometer configuration that has found use in sensing applications is the Sagnac interferometer, shown in Figure 3.3. In this configuration, the input beamspliter divides the field into clockwise and counterclockwise paths around the interferometer, forming a closed, bidirectional loop. A vapor cell is included in the loop, but since both paths encounter the vapor cell and are phase shifted, there is zero sensitivity to dispersion induced phase in this interferometer. At the beamsplitter, the interfering fields yield:

$$E_{\text{sagnac}} = \frac{A}{2}\exp(-i\omega t + i\phi_{\text{cw}} + i\phi_{\text{cell}}) + \frac{A}{2}\exp(-i\omega t + i\phi_{\text{ccw}} + i\phi_{\text{cell}}) \tag{3.19}$$

where ϕ_{ccw} and ϕ_{cw} are the phases picked up by the counterclockwise and clockwise paths. Upon photodetection, we recover a voltage signal proportional to:

$$V_{\text{PD}} \propto \cos(\phi_{\text{ccw}} - \phi_{\text{cw}}) \tag{3.20}$$

The phase shift $\phi_{\text{ccw}} - \phi_{\text{cw}}$ is known as the Sagnac phase and proportional to rotation rate of the Sagnac loop, enabling Sagnac interferometers to be used as sensitive gyroscopes. However, this readout is completely insensitive to dispersion induced phase, due to the inherent reciprocity of the Sagnac interferometer. In Chapter 5, we will discuss a modification that will allow a dispersion induced phase shift to be extracted. This also requires an additional layer of digital modulation. On the other hand, the balanced path lengths give the Sagnac interferometer excellent immunity to laser frequency and path length noise, making this interferometer a worthwhile avenue to pursue.

3.3 Frequency and Phase Noise Coupling

To see how laser frequency noise couples into the the readout of a two beam interferometer, consider the phase accrued by an optical field with an optical modulation depth of ω_L

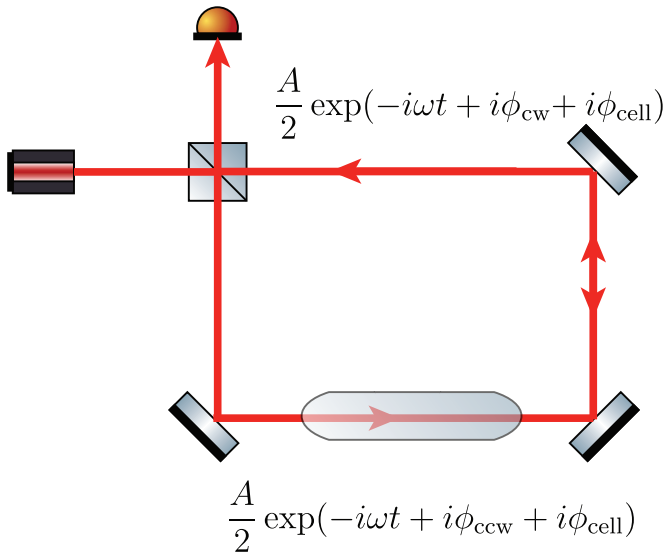

Figure 3.3: The input field is split into clockwise and counterclockwise paths around a closed loop. A vapor cell has been included for consistency. The fields interfere at the input beamsplitter and are incident on a photodetector.

around its center frequency, oscillating at a Fourier frequency Ω. To calculate the phase accrued, we integrate the time varying optical frequency over the time of flight of the field:

$$\begin{aligned}\phi_{\text{sig}} &= \omega_L \int_0^{\tau_{\text{sig}}} \exp(i\Omega t)dt \\ \phi_{\text{ref}} &= \omega_L \int_0^{\tau_{\text{ref}}} \exp(i\Omega t)dt\end{aligned} \tag{3.21}$$

where the two arms of the interferometer are denoted by signal and reference. Integrating, we obtain the phase difference $\Delta\phi$:

$$\Delta\phi = \phi_{\text{sig}} - \phi_{\text{ref}} = \frac{\omega_L}{i\Omega}[\exp(i\Omega\tau_{\text{ref}}) - \exp(i\Omega\tau_{\text{sig}})] \tag{3.22}$$

The absolute magnitude of the phase difference is given by:

$$|\Delta\phi| = \sqrt{\Delta\phi\Delta\phi^*} \tag{3.23}$$

$$\begin{aligned}&= \sqrt{\frac{2\omega_L^2}{\Omega^2}(1-\cos\Omega\Delta\tau)} \\ &= \sqrt{\frac{4\omega_L^2}{\Omega^2}\sin^2\left(\frac{\Omega\Delta\tau}{2}\right)} \\ &= \frac{2\omega_L}{\Omega}\sin\left(\frac{\Omega\Delta\tau}{2}\right)\end{aligned} \tag{3.24}$$

where $\Delta\tau$ is the time of flight distance between the signal and reference path $\tau_{\text{sig}} - \tau_{\text{ref}}$. Dividing both sides by ω_L, this equation gives us a transfer function between laser frequency noise and phase. We plot this transfer function $|\Delta\phi|/\omega_L$ as a function of Ω, the Fourier frequency, in Figure 3.4 below:

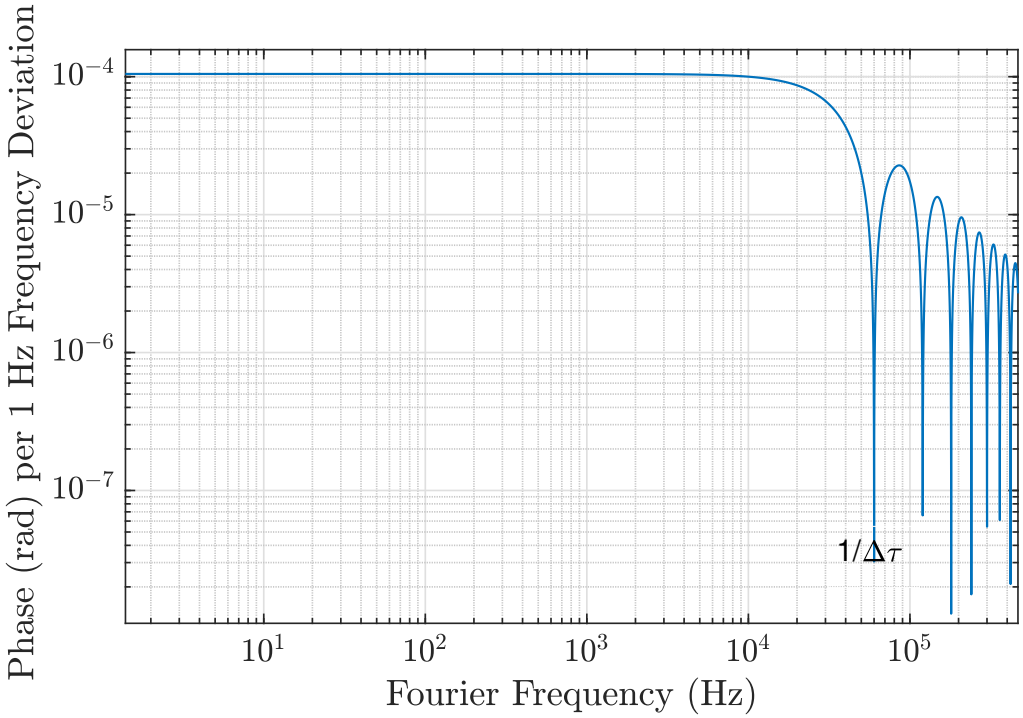

Figure 3.4: Equation (3.24) is plotted as a function of Ω. The arm length difference is 5 kilometers, equal to a time of flight difference $\Delta\tau$ of 16 μs, and corresponding to the first null at 62.5 KHz. The y-axis corresponds to the phase excursion per optical modulation depth ω_L of 1 Hz.

We have chosen a long arm length mismatch of 5 km to illustrate the general shape of the two beam interferometer transfer function, which has a null at the Fourier frequency corresponding to the arm length difference. An interferometer with such a long arm length mismatch serves as a good frequency noise sensor. For example, consider a typical telecommunications grade distributed feedback (DFB) laser frequency noise spectrum [70] plotted in Figure 3.5 below.

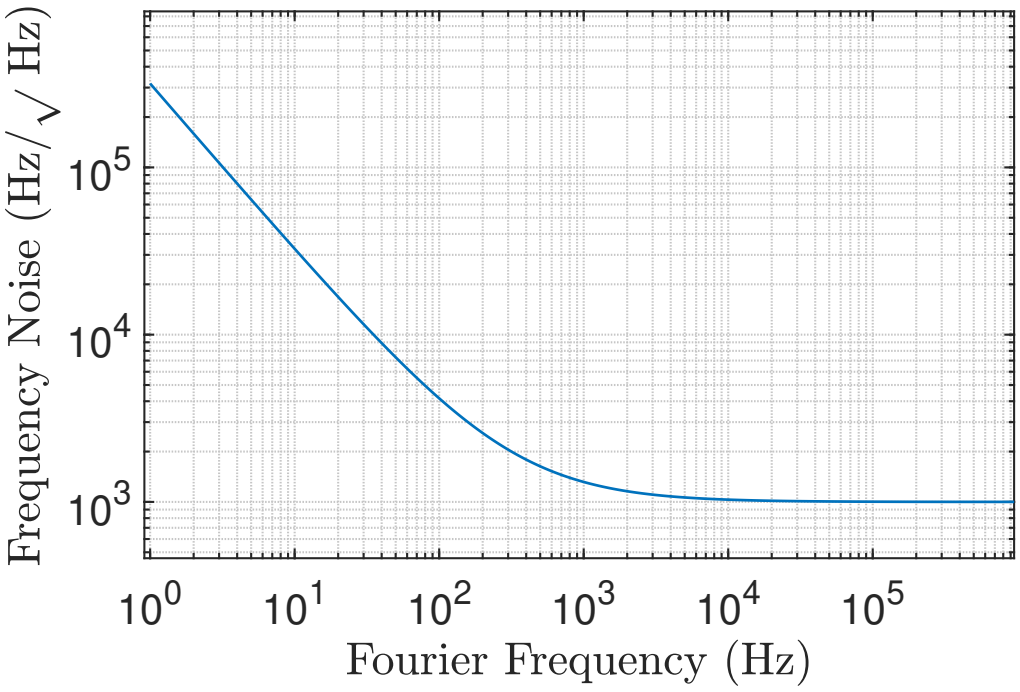

Figure 3.5: A typical telecommunications grade DFB frequency noise is plotted. We have used a 1/f frequency noise model, which approximates well the frequency noise characteristics of a DFB laser. The laser frequency noise rolls of to 1KHz/$\sqrt{\text{Hz}}$ at beyond 1 KHz fourier frequencies.

DFB lasers generally have a 1/f rolloff of laser frequency noise, down to a noise floor. Multiplying the 5 km armlength mismatch transfer function by this frequency noise spectrum, we obtain a phase spectral density, plotted in Figure 3.6:

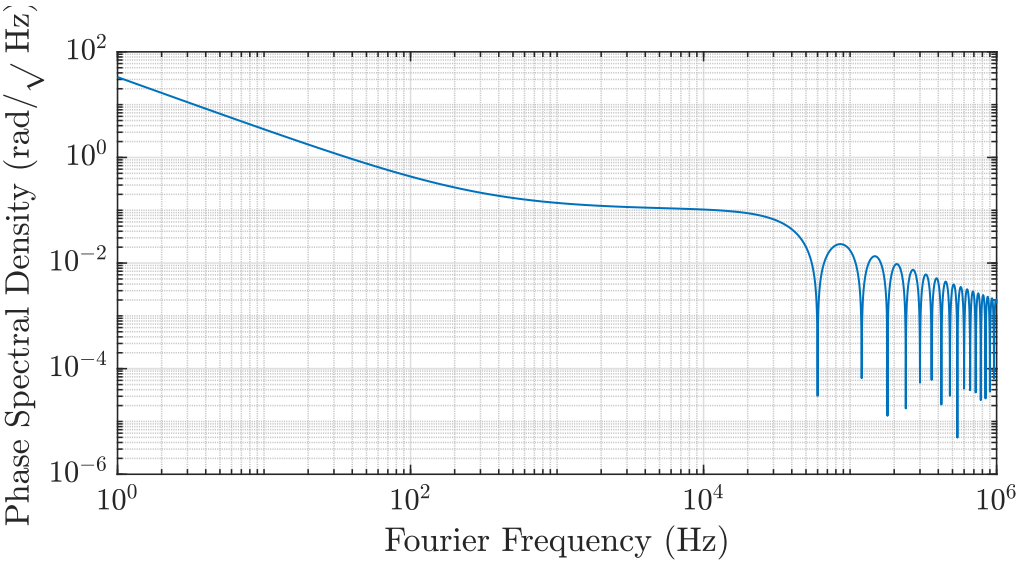

Figure 3.6: Here, we multiply the laser frequency noise for a typical DFB laser shown in Figure 3.5 with the Mach-Zehnder interferometer transfer function for a 5 km armlength mismatch shown in Figure 3.4.

As an interferometer used to measure frequency noise, this constitutes a large phase signal (tens of radians at 1 Hz) that is relatively easy to track. However, in this thesis, we are

concerned with interferometers that have a maximum of thirty meters in arm length difference. In this case, $\Delta\tau$ is much smaller, on the order of $1-10$nS. Here, the transfer function roll off is at GHz Fourier frequencies, well beyond typical measurement bandwidths. This transfer function is well-approximated as a DC value. For a 1 meter arm length difference, we insert the time of flight equivalent into Equation 3.24 and obtain a DC level of 20 nrad of phase. Multiplying this DC transfer function by the laser frequency noise trace plotted in Figure 3.6, we obtain the phase noise spectral density for a two beam interferometer with a 1 m arm length mismatch, plotted in Figure 3.7:

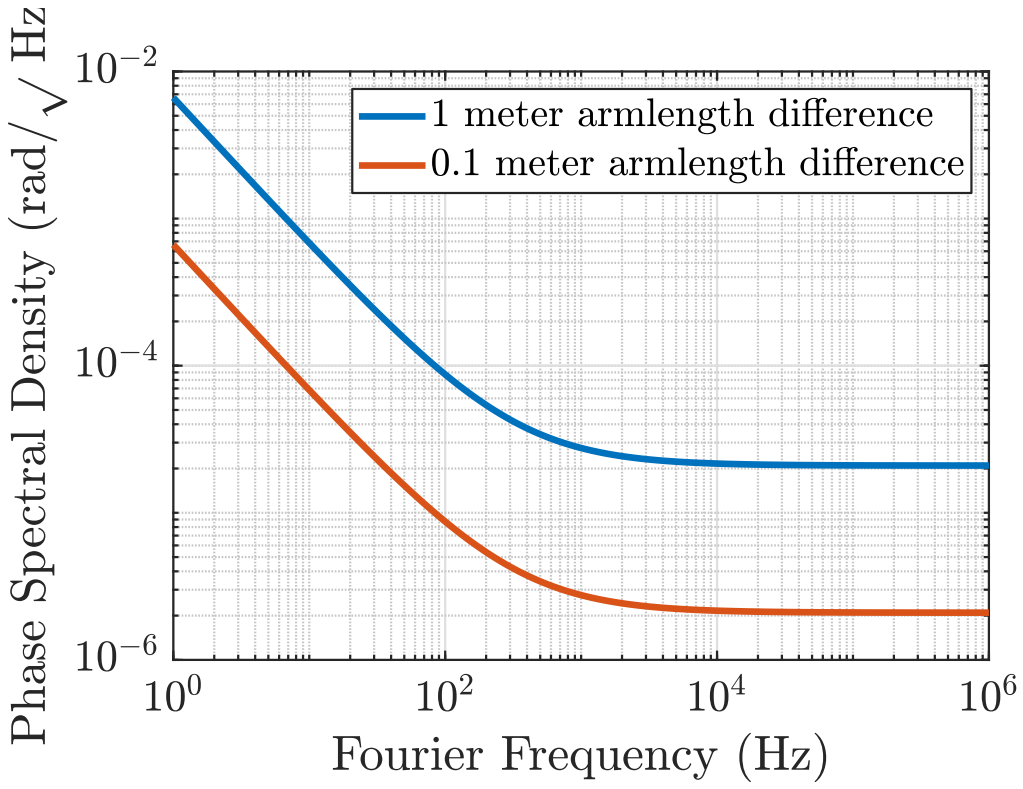

Figure 3.7: Here, we follow the same procedure to obtain a phase noise spectral density plot driven by laser frequency noise as in Figure 3.6. We plot this for armlength differences of 1 meter and 0.1 meter. Instead of trying to track laser frequency noise as in a frequency reference, we are concerned with frequency noise entering a spectroscopic measurement as a spurious source of phase noise. This phase noise is seen to be 0.7 mrad $/\sqrt{\text{Hz}}$ at 10 Hz for 1 meter armlength difference and 0.07 mrad $/\sqrt{\text{Hz}}$ for the 1 cm armlength difference.

To see the implications of this phase noise level for a dispersion measuring interferometer, consider a laser scan rate of 10 Hz across an absorption line. Previously, we calculated that for an absorption line with a depth of 0.5 through a length of 10 cm, the dispersion induced phase shift is 0.2 radians. Looking at the phase noise at a Fourier frequency of 10 Hz in Figure 3.7, this would imply a 0.7 millradian phase noise level, and a modest signal to noise ratio of 285, in the absence of any other sources of noise, which is worse than the SNR of absorption spectroscopy methods [71]. However, this is for an interferometer with a 1 meter armlength difference. At 0.1 meter armlength difference, the phase noise is an order of magnitude smaller. Thus, in order to extract the dispersion induced phase at 10 Hz with an SNR>2000 so as to be comparable with absorption spectroscopy, the path lengths must be matched to within 10 cm. This is not a trivial task in Mach Zehnder

fiber interferometers. Alternatively, we can use inherently balanced interferometers such as a Sagnac interferometer such that the phase noise contribution from this first order frequency noise coupling is zero.

3.4 Digital Interferometry

Digital interferometry is a set of optical phase extraction techniques that form the basis of interferometric dispersion measurements in this thesis. At its core, digital interferometry is built on the phase modulation of optical fields with pseudo-random sequences. These pseudo-random sequences have well-defined autocorrelation properties, such that demodulation of the optical carrier by a local sequence with a controllable *electronic* delay allows selective signal isolation based on *optical* delay.

3.5 Elements of Digital Interferometry

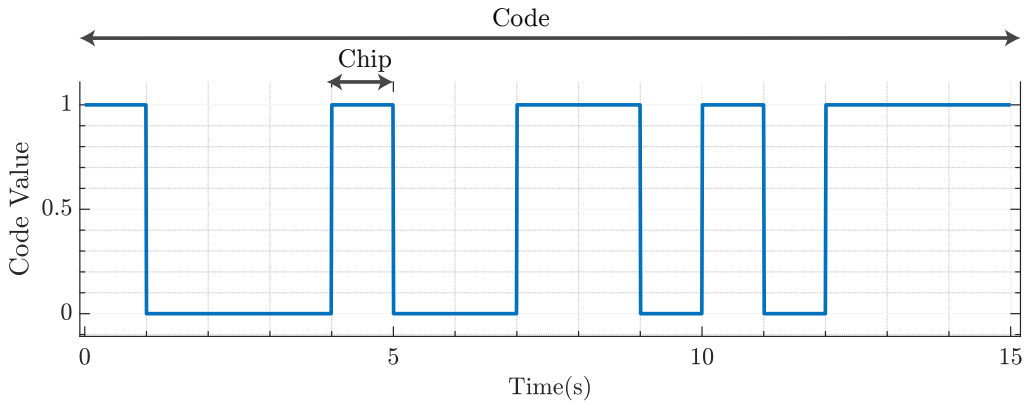

Figure 3.8: A sample 4 bit, 15 length code is displayed. We have chosen the time base of our code to be in seconds. One chip represents one element of the code, which in this case is one second. This also defines our chip frequency of 1 Hz. The code frequency is therefore 1/15 Hz.

The first generation of digital interferometry techniques used the Maximal-length sequence as the modulation code, and to date, they remain the most widely used DI sequence due to the periodicity of their autocorrelation properties and their ease of generation. M-sequences also benefit from being well characterized through decades of use in the telecommunications industry [72]. The Maximal-length, or m sequence is a type of pseudo-random bit sequence (PRBS), which toggles between 1 and 0, or alternatively 1 and -1. M sequences are generated using linear feedback shift registers, which are recursive state machines that calculate an input bit using an XOR operation on the bits currently within the shift register, and then shift (output) the rightmost register bit.The maximum periodicity, or length of the sequence is set by the bitwidth of the shift register. The bits on which the XOR operates are called taps, and these are specifically chosen to maximize the periodicity of the sequence. For an N-bit LFSR, the m-sequence periodicity, or length is given by

$$L = 2^N - 1 \tag{3.25}$$

where N is the number of bits held in the shift register. In Figure 3.8, a sample 4 bit (N=4) DI code with 15 elements is plotted. In the terminology of digital interferometry, we define a chip as one element of the code. As we have chosen a chip length of 1 second, we can also define a chip frequency, of 1 Hz. Since the code length is 15, this also defines a code frequency of 1/15 Hz.

3.5.1 Digitally Enhanced Heterodyne Interferometry

So far, we have only discussed the m-sequence code with reference to binary values 1 and 0. In a heterodyne digital interferometry scheme, this code is modulated onto the phase of the optical carrier, with a modulation depth of π. This means that the optical carrier phase is inverted when the code value is equal to 1. We illustrate a simple heterodyne DI system with this modulation scheme in Figure 3.9 below:

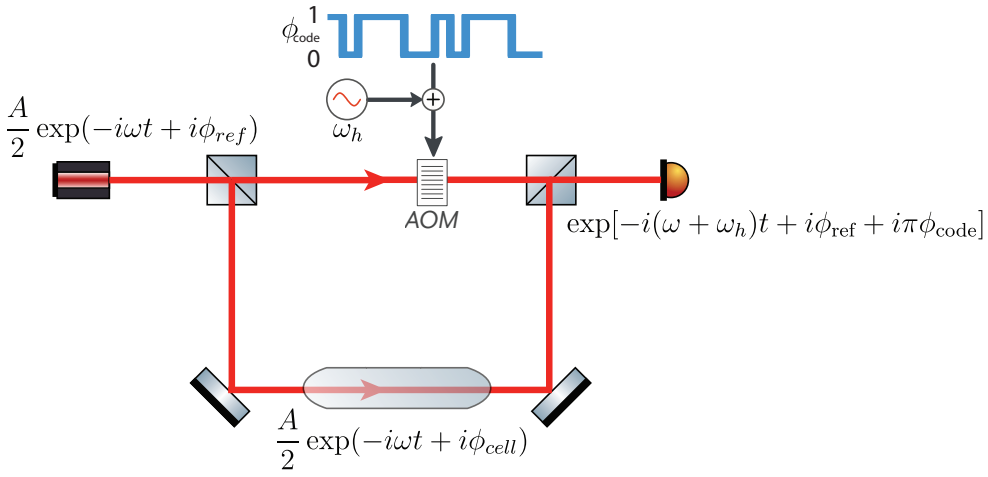

Figure 3.9: A heterodyne interferometer with an m-sequence modulated onto the optical carrier using the acousto-optic modulator. This is done by phase modulating the heterodyne frequency ω_h at π depth. Mathematically, this is represented by adding the $i\pi\phi_{\text{code}}$ phase term to the complex exponential, where ϕ_{code} pseudorandomly toggles between 1 and 0.

Here, for clarity, we have written the DI modulation code as an exponential phase $\exp[i\pi\phi_{\text{code}}(t-\tau)]$, where τ is the code delay. However, the exponential phase term can be simplified as $C(n-\tau)$ where $C(n-\tau)$ represents a single element of the bipolar code and takes the value of 1 or -1. Hence we write the modulated field E_{mod}:

$$E_{\text{mod}} = \exp[-i(\omega+\omega_h)t + i\phi_{\text{ref}} + i\pi\phi_{\text{code}}(t-\tau)] \tag{3.26}$$

$$= C(n-\tau)\exp[-i(\omega+\omega_h)t + i\phi_{\text{ref}}] \tag{3.27}$$

The effect of the modulation on the carrier is to pseudorandomly invert the phase of the heterodyne beat note. We plot a time domain representation of a carrier modulated by a 4 bit code in Figure 3.10 below.

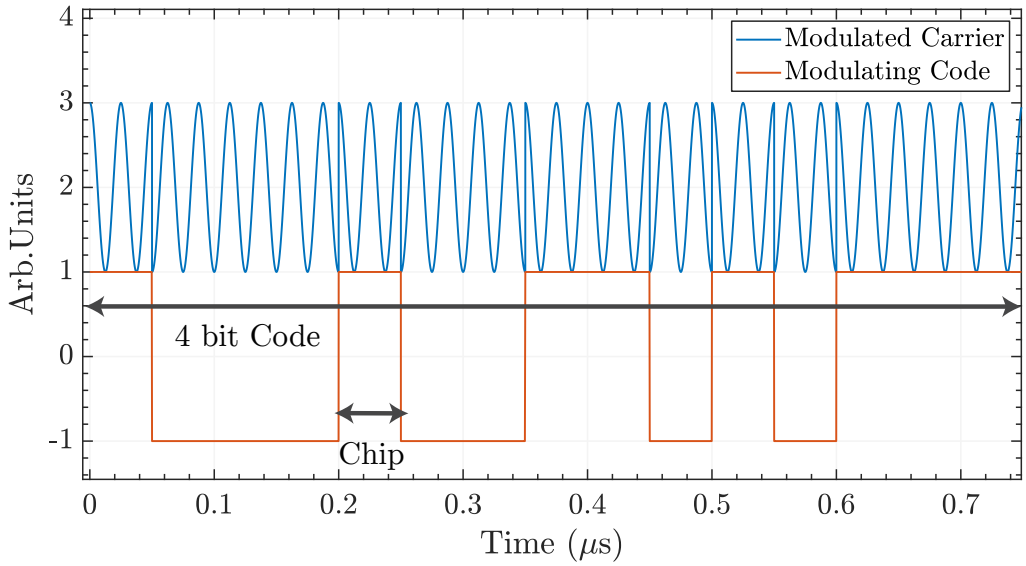

Figure 3.10: A 40 MHz carrier phase modulated by a 4 bit code with a 20 MHz chip frequency is plotted. The modulating code, offset for clarity is also plotted. Since the 20 MHz chip frequency is half that of the carrier frequency, a single chip period, as indicated in the Figure consists of two periods of the carrier wave. At the chip transitions, the π phase flip is visible as a discontinuity in the carrier phase.

The frequency domain representation of the resulting beat note at the photodetector is plotted in Figure 3.11 below.

The effect of the digital interferometric code is to suppress the beatnote at 40 MHz, and spread the beatnote power to a comb of frequencies. The nulls of the comb envelope are set by the chip frequency f_{chip} and the spacing between each of the teeth are set by the code frequency f_{code}.

DI modulation can also be viewed as a controlled broadening of the optical source. Consider a beatnote in standard heterodyne interferometry. A narrow-linewidth source ($<$ 1 KHz) can be treated as a narrow spike around the heterodyne frequency, with width equal to the linewidth of the source. When DI phase modulation is applied, the chip frequency determines the new broadened linewidth. Associated with a linewidth, is also the coherence length of the modulation broadened source, which we call the digital coherence length:

$$L_{DI} = \frac{c}{n f_{chip}} \tag{3.28}$$

where c is the speed of light in vacuum, n the refractive index of the medium of propagation and f_{chip} the chip frequency. Indeed, the essence of digital interferometry lies in the ability to control coherence since the codes are pseudorandom. At photodetection, we can "undo"

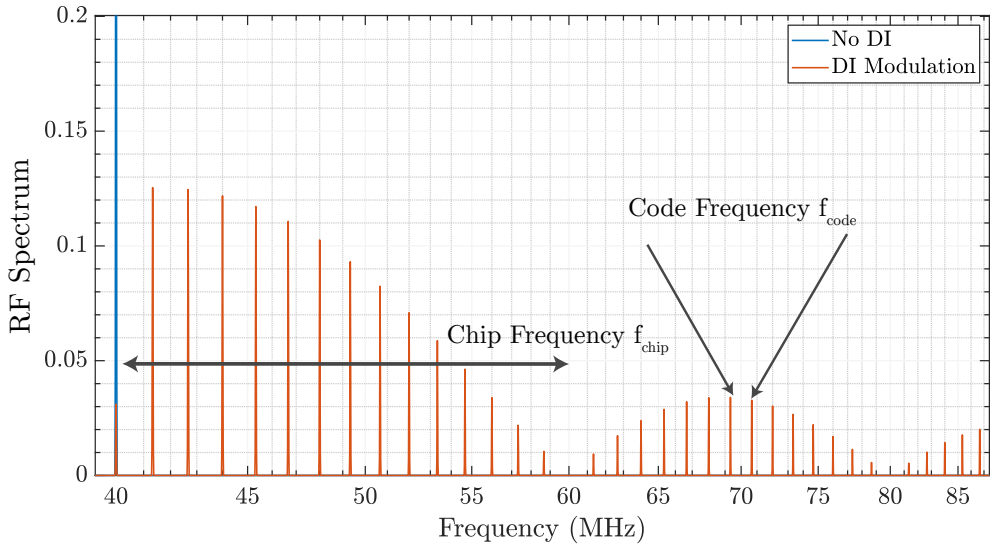

Figure 3.11: Simulated normalized radio frequency (RF) spectrum of a 4 bit modulation sequence at 20 MHz on a 40 MHz carrier. This is the frequency domain representation of the modulated carrier plotted in Figure 3.10. The unmodulated carrier at 40 MHz is also plotted in blue as a sharp peak. We see the spread-spectrum envelope can be broadened by increasing the chip frequency, which corresponds to the first null of the spectrum, currently at (40+20 = 60 MHz). Looking within the envelope, we see the spread-spectrum consists of 15 individual harmonics, corresponding to the code length, the spacing of which is determined by the code frequency. These need to be resolved in order to achieve robust, error-free decoding. We also note that the spectrum is symmetric around 40 MHz, but have chosen not to plot it here, as the FFT routine used to generate the spectrum introduces distortions as the frequency approaches DC (zero frequencies)

the phase scrambling by performing an autocorrelation with a locally delayed copy of the code:

$$A(\tau) = \sum_{n=1}^{L} C(n)C(n-\tau) \tag{3.29}$$

where τ is the code delay, and L is the code length. $C(n)$ represents one element of the code, and takes the values of 1 or -1. M-sequences are designed such that their autocorrelation have the following properties:

$$A(\tau) = \begin{cases} L, & \text{if } \tau = mL \text{ where } m \exists \mathbb{Z}. \\ -1, & \text{otherwise.} \end{cases} \tag{3.30}$$

This autocorrelation function for a 5 bit code with $L_{\mathrm{DI}} = 31$ is plotted in Figure 3.12 below:

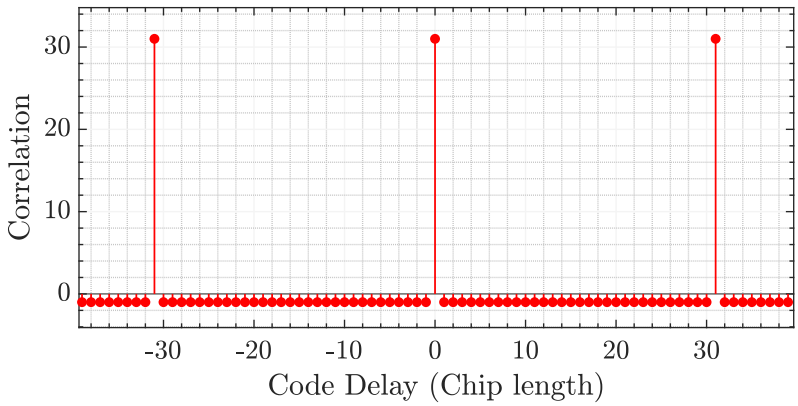

Figure 3.12: Here, we plot the autocorrelation of a five bit code ($L_{\mathrm{DI}} = 31$). At zero delay, the code correlation is equal to the code length (31). Since the code repeats every code length, the code correlation is also 31 at every integer multiple of the code length. At all other delays, the correlation is -1.

We see that the autocorrelation reaches a peak value equal to the code length of 31 at zero delay, and at every integer multiple of the code length. In other words, coherence of the carrier is only recovered when the code is correlated with itself. Let us extend digital interferometry to the heterodyne interferometer model to see how this control of coherence allows us to range gate. Consider the reference and vapor cell fields in Figure 3.9. At the photodetector, their interference yields:

$$\begin{aligned} P_{\mathrm{mod}} &= \frac{P_{\mathrm{in}}}{4}[1 + \cos(\omega_h t + \phi_{\mathrm{cell}} - \phi_{\mathrm{ref}} + \pi\phi_{\mathrm{code}}(t-\tau))] \\ &= \frac{P_{\mathrm{in}}}{4}[1 + C(n-\tau)\cos(\omega_h t + \phi_{\mathrm{cell}} - \phi_{\mathrm{ref}})] \end{aligned} \tag{3.31}$$

At demodulation, the signal at the photodetector is multiplied by a local copy of the code $C(n - \tau_{\mathrm{decode}})$:

$$V_{\mathrm{decode}} = \frac{V_{\mathrm{in}}}{4}[C(n-\tau_{\mathrm{decode}})C(n-\tau)\cos(\omega_h t + \phi_{\mathrm{cell}} - \phi_{\mathrm{ref}})] \tag{3.32}$$

where we have only kept the interference term for clarity, and converted power to units of voltage. Since the code C(n) only takes values of 1 or -1, multiplying by the correctly delayed code reverses the inversion of the phase, recovering a pure heterodyne tone. For the heterodyne interferometer pictured in 3.9, this means choosing $\tau_{\mathrm{decode}} = \tau$, where τ is the optical time of flight between the modulation of the code at the AOM, and the photodetector, in addition to any electronic delays. When $\tau_{\mathrm{decode}} \neq \tau$, the multiplication of the unmatched codes yield a third code, leaving the phase of the resulting signal scrambled. The results of correct and incorrect decoding are plotted in Figure 3.13 below:

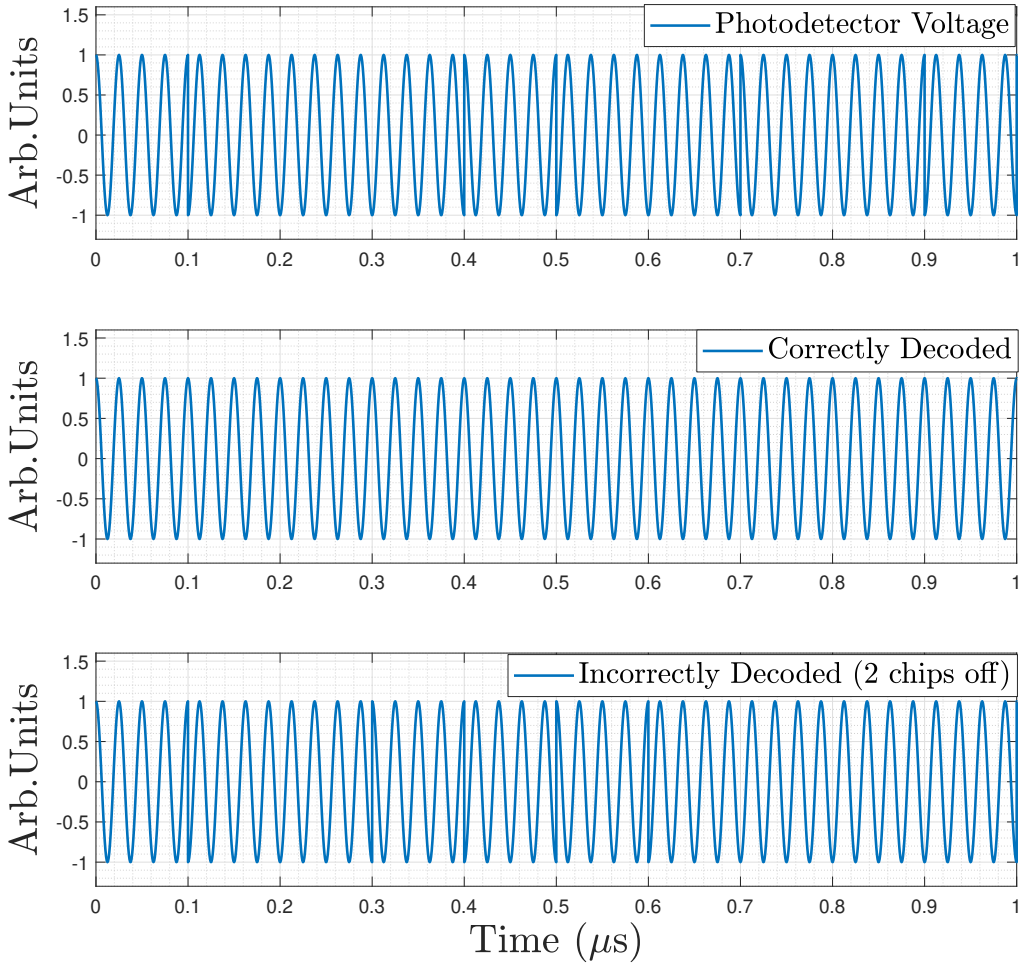

Figure 3.13: In the top subplot, we have plotted the photodetector voltage before decoding. The signal is a 40 MHz carrier phase modulated by a 4 bit code with a 20 MHz chip frequency. In the second subplot, the photodetector signal has been multiplied by a correctly delayed code, recovering a coherent heterodyne tone at 40 MHz. In the bottom subplot, the photodetector signal is multiplied by a copy of the code that is delayed by 2 chips. The result is a phase that remains scrambled and incoherent. In the Fourier domain, the signal is still spread spectrum, and can be rejected using appropriate low-pass filtering.

Thus far, we have not performed an autocorrelation, only an element wise multiplication of the two codes that demonstrates coherent vs incoherent phase recovery. However, the demodulation process requires an autocorrelation to be applied. The first step in heterodyne DI demodulation proceeds through the IQ mixdown procedure outlined in the previous section, where we have omitted the DC term at the photodetector for simplicity:

$$V_{\text{mix,I}} = \frac{V_{\text{PD}}}{8} C(n-\tau_{\text{decode}})C(n-\tau)\cos\Big[2\omega_h t + \Delta\phi\Big] + \frac{V_{\text{PD}}}{8} C(n-\tau_{\text{decode}})C(n-\tau)\cos\Delta\phi$$
$$V_{\text{mix,Q}} = \frac{V_{\text{PD}}}{8} C(n-\tau_{\text{decode}})C(n-\tau)\sin\Big[2\omega_h t + \Delta\phi\Big] - \frac{V_{\text{PD}}}{8} C(n-\tau_{\text{decode}})C(n-\tau)\sin\Delta\phi \tag{3.33}$$

Following IQ mixing, the autocorrelation is taken by summing over a codelength, as given in Equation 3.29 noting that the baseband and $2\omega_h$ terms are also summed over:

$$V_{\text{mix,I}} = \sum_{n=1}^{L} \frac{V_{\text{PD}}}{8} C(n-\tau_{\text{decode}})C(n-\tau)\cos\Big[2\omega_h t+\Delta\phi\Big]+\sum_{n=1}^{L} \frac{V_{\text{PD}}}{8} C(n-\tau_{\text{decode}})C(n-\tau)\cos\Delta\phi$$

Applying the autocorrelation properties of m-sequences in Equation 3.30, we obtain the following for the in phase component of the signal:

$$V_{\text{mix,I}} = \begin{cases} \frac{V_{\text{PD}}}{8} L \sum_{t=0}^{t_{\text{code}}} \cos\Big[2\omega_h t + \Delta\phi\Big] + \frac{V_{\text{PD}}}{8} L \sum_{t=0}^{t_{\text{code}}} \cos\Delta\phi, & \text{if } \tau = \tau_{\text{decode}}. \\ \frac{V_{\text{PD}}}{8} \sum_{t=0}^{t_{\text{code}}} \cos\Big[2\omega_h t + \Delta\phi\Big] + \frac{V_{\text{PD}}}{8} \sum_{t=0}^{t_{\text{code}}} \cos\Delta\phi, & \text{if } \tau \neq \tau_{\text{decode}}. \end{cases} \tag{3.34}$$

where the autocorrelation properties of the codes yield the correlation constant L (code length), when $\tau = \tau_{\text{decode}}$, and 1 otherwise.

Since the autocorrelation is taken by summing over one complete codelength, we rewrite the limits of the sum in units of time, where the upper limit is the code time t_{code}. This is equivalent to a simple windowed averaging filter on the baseband and $2\omega_h$ terms. Since the average is taken over the code time, the corner frequency of this filter is equivalent to the its inverse, the code frequency. From Figure 3.11, we can see that the code frequency is much smaller than the heterodyne frequency. Therefore, the code summation operation fulfills the function of the final low pass filter stage in the IQ mixdown operation, removing the $2\omega_h$ term. This results in the filtered expression for the in-phase signal:

$$V_{\text{mix,I}} = \begin{cases} \frac{V_{\text{PD}}}{8} \sum_{t=0}^{t_{\text{code}}} \cos\Delta\phi, & \text{if } \tau = \tau_{\text{decode}}. \\ \frac{V_{\text{PD}}}{8} \frac{1}{L} \sum_{t=0}^{t_{\text{code}}} \cos\Delta\phi, & \text{if } \tau \neq \tau_{\text{decode}}. \end{cases} \tag{3.35}$$

where we have divided through by the codelength L to normalize the averaging filter. We have also kept the summation to show that $\cos\Delta\phi$ has been downsampled to the code frequency. The same IQ demodulation and filtering process is applied to the quadrature signal:

$$V_{\text{mix,Q}} = \begin{cases} -\frac{V_{\text{PD}}}{8} \sum_{t=0}^{t_{\text{code}}} \sin\Delta\phi, & \text{if } \tau = \tau_{\text{decode}}. \\ -\frac{V_{\text{PD}}}{8} \frac{1}{L} \sum_{t=0}^{t_{\text{code}}} \sin\Delta\phi, & \text{if } \tau \neq \tau_{\text{decode}}. \end{cases} \tag{3.36}$$

From the decoding process, we can see that incorrectly decoded signals are suppressed by a factor of the code length L. Choosing a longer code length allows for greater suppression, but at the tradeoff of lower signal bandwidth.

By careful choice of τ_{decode} to match optical time of flights of interest, we can isolate and track multiple paths in an interferometer. Conversely, scattering fields will be suppressed by the code length, as they will have time of flights different from the primary interfering fields. The resolution of this range gating is set by the physical chip length, as the autocorrelation rapidly falls from its peak value when τ_{decode} is detuned by just one chip.

In other words, we can multiplex two or more signals as long as their time of flights differ by at least one physical chip length. This capability will be explored in Chapter 6, where the phase accrued over three optical paths will be coherently decoded using digital heterodyne interferometry.

3.5.2 From Digital Heterodyne to Digital Homodyne Interferometry

Historically, digital heterodyne interferometry was developed first, as linear phase extraction is in general, easier using heterodyne interferometry. From Equation 3.8, we can see that the dispersion induced phase shift is encoded onto the optical power received via the cosine term. Thus to recover the phase, a nonlinear phase extraction scheme is required, on top of resolving phase ambiguities due to the discontinuous inverse cosine function. In contrast, traditional heterodyne interferometry yields a continuous, unwrappable phase readout.

In heterodyne interferometry, the signal field (arm with the vapor cell) is frequency offset from the reference field (arm with the frequency shift), as seen in in Figure 3.2. The frequency offset causes a linearly ramping phase shift between the two fields, with the slope being the heterodyne frequency. The phase ramp, in effect samples the in-phase and quadrature components of the complex plane, reconstructing the interference fringe. Thus, direct phase extraction can be done without digital interferometric modulation. Digitally Enhanced Homodyne Interferometry [39, 73], by contrast, accomplishes this sampling of the in-phase and quadrature components with a four-level phase-stepping algorithm. This can be applied either using an electro-optic phase modulator, or by phase modulating the frequency shift of an acousto-optic modulator. This allows the modulation to sweep all four quadratures of the phase plane, eliminating the need for the heterodyne tone and further reducing the physical complexity of the system. However, we note that in this scheme, digital interferometric modulation is an in-built and necessary requirement for phase extraction. These differences are highlighted Figure 3.14 below, where we show heterodyne and homodyne phase scanning of an IQ plane.

In the next chapter, we will provide a mathematical expression for this modulation scheme, showing that the four-level-phase stepping algorithm can be expressed as the sum of a modulation code that toggles between in-phase components, and an orthogonal code that toggles between the quadrature components of the interference fringe.

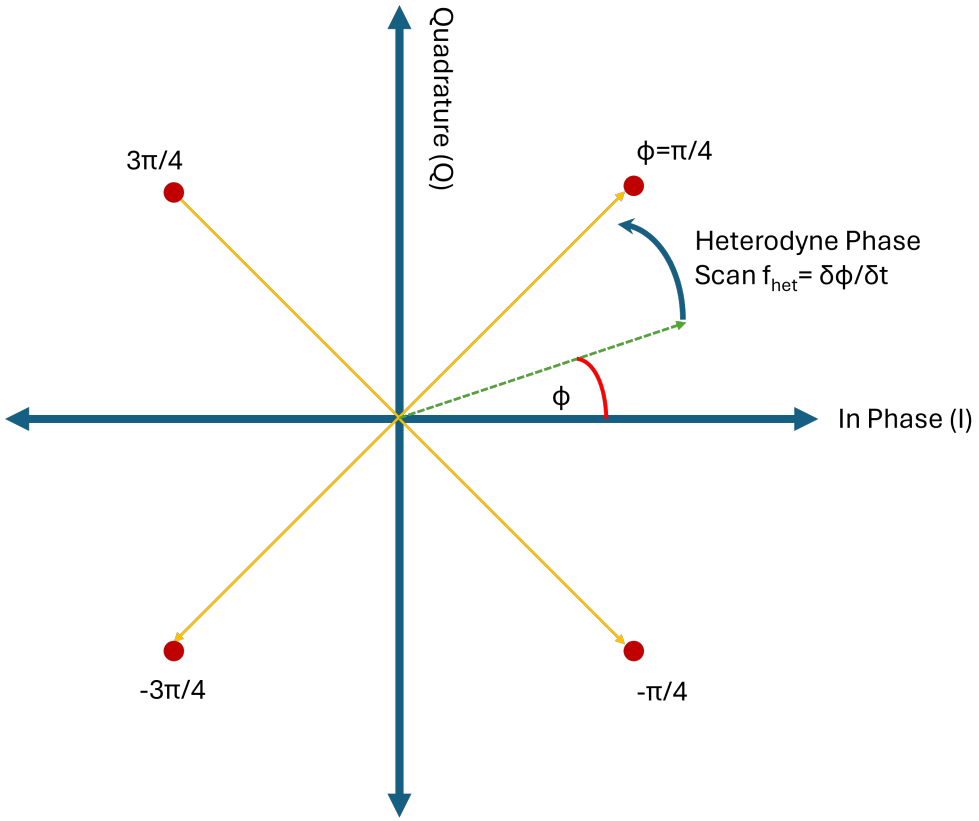

Figure 3.14: In heterodyne digital interferometry, the phasor (interference fringe) rotates around the IQ plane, sampling all four quadrants equally. By contrast, homodyne digital interferometry evenly samples the IQ plane using a four level phase stepping algorithm, forming a four point constellation with of $\pm\pi/4$, and $\pm\,3\pi/4$. We note that despite this scanning of the four quadrants of the IQ plane, digital homodyne interferometry is named as such because a frequency shift is not required.

3.6 Summary

In the first broad section of this chapter, we introduced two beam interferometry, which is the core sensing technique used in this thesis to extract dispersion induced phase shifts. We introduced heterodyne and homodyne interferometry, two common readout schemes for interferometers, showing that it is possible to extract a dispersion induced phase shift in the signal arm of a two-beam Mach-Zehnder interferometer. An alternative two beam homodyne interferometer, the Sagnac was also introduced as an inherently balanced sensing configuration that offers suppression of laser frequency noise, compared to standard two beam interferometers.

Digital Interferometry was then introduced as a phase extraction scheme used throughout this thesis. We outlined the basic terminology and concepts used for describing DI systems and proceeded through the derivation of modulation and decoding process for a Digitally Enhanced Heterodyne Interferometry phase signal. This illustrated the key concepts of DI: controllable coherence enabling signal multiplexing and range gating of interferometric signals.

4 Digitally Enhanced Sagnac Interferometer

In this chapter, we introduce the Sagnac interferometer as a proving ground for the performance of digital interferometry in fiber interferometers. This is due to its inherently matched path lengths, removing the effect of first order frequency noise coupling in the phase measurement. For the same reason, the Sagnac interferometer is also a good candidate as an interferometer used for dispersion spectroscopy, where dispersion induced phase shifts are only on the order of 10^{-2} radians.

Traditionally, Sagnac interferometers are used to measure rotation rate, and have found use as fiber optic gyroscopes [74]. For that application, white light sources such as superluminescent diodes with > 40 nm of optical bandwidth are used. This is to mitigate the effect of Rayleigh and polarization scattering, as scattering perturbations on the phase readout are rendered incoherent [75] due to the extremely short coherence length of the sources. However, measurements of dispersion induced phase requires a coherent and tunable light source. In order to use the Sagnac interferometer for dispersion spectroscopy, we modify the architecture of a traditional Sagnac interferometer and introduce the use of digital interferometry. This allows us to overcome the problem of scattering when using a laser diode, while still preserving the path length stability of a Sagnac interferometer.

4.1 Introduction

Digital Interferometry (DI) was developed originally for highly coherent, narrow linewidth optical sources [35], achieving phase sensitivities of ~ 10 $\mu\text{rad}/\sqrt{\text{Hz}}$ with a continuous, unwrapped phase readout [40, 76]. The technique works by introducing a pseudo-random phase modulation which results in an optical spread-spectrum in frequency domain. This enables gating of spurious interference, similar to white-light interferometry used for optical coherence tomography [77] and fiber optic gyroscopes. Upon demodulation of the code for the chosen macroscopic optical path length, coherence is recovered.

This allows for a tunable, high coherence source such as a Distributed Fiber Bragg (DFB) laser to be used in a Sagnac interferometer, as a DI modulated laser behaves like a low coherence length source while propagating through the Sagnac loop. However, upon demodulation, coherence is selectively recovered for the path length of interest (clockwise and counterclockwise paths), while spurious scattering path lengths remain incoherent and are strongly rejected. This is the main motivation in using digital interferometry for

a laser interrogated Sagnac interferometer– we reap the benefits of coherent sources for interferometry, while mitigating coherent scattering.

In the previous chapter, we bridged the gap from Digital Heterodyne Interferometry to Digital Homodyne Interferometry. This variant is the modulation scheme used in the Sagnac interferometer, which, due to its reciprocity, requires a homodyne phase readout, as any 'heterodyne' frequency shift seen in one of its arms will also be seen by the other. This architecture and modulation scheme retains the sub-microradian phase sensitivity offered by Digital Heterodyne Interferometry while enabling a continuous, high dynamic range readout free of active phase control.

4.2 Digitally Enhanced Sagnac Modulation Scheme

Introduced in the previous chapter, Digital Heterodyne Interferometry uses pseudo-random phase modulation to encode the optical phase. This allows for the propagation time of the code through an optical system to be identified by the delay of the code's auto-correlation in demodulation. Critically, this auto-correlation is low-valued for all time delays except for when it is an integer multiple of the code period. However, DE-HoI differs from Digital Heterodyne Interfometry in that two pseudo-random binary codes are used to create a 4-level phase constellation, akin to Quadrature Phase Shift Keying (QPSK) modulation. These 4 levels allow for discrete sampling of each quadrature of the IQ plane, with each code corresponding to a specific quadrature, as shown in Figure 3.14 from the previous chapter. The effect of this modulation is to pseudo-randomly toggle across all four quadratures of the IQ plane, forming a pseudorandom, four-level phase modulation signal. A snippet of this signal is shown in the QPSK Phase Modulator box in Figure 4.1.

We can describe such a QPSK phase modulated electric field in terms of its constituent pseudo-random binary codes using the following expression:

$$E(t) = \tilde{E}(t)M(t)e^{i\omega t + i\phi(t)} \tag{4.1}$$

$$M(t) \equiv C_I(t) + iC_Q(t) \tag{4.2}$$

where $C_I(t)$ and $C_Q(t)$ are mappings of the I and Q binary codes to ± 1. We write this in compact form as $M(t)$, noting that this forms a constellation of four modulation points in the complex plane. $\tilde{E}(t)$ represents the time varying amplitude of the field, ω the optical carrier frequency and $\phi(t)$ a time varying phase. The code delay, τ is determined by the propagation time from the point of modulation to the point of decoding in signal processing. This is typically dominated by the time-of-flight through the optical system. When implemented in a two beam interferometer this results in two optical fields superposed at the photodetector, each encoded with a uniquely delayed QPSK code.

To implement a digital interferometric readout for a Sagnac interferometer, we require phase modulation to be encoded on both the clockwise (CW) and counterclockwise (CCW) metrology fields. Due to the symmetric nature of the Sagnac interferometer, any modulation that is encoded outside the interferometer is common, and does not manifest itself in the measurement. While this reciprocity condition is advantageous for suppressing laser frequency noise and other common noise sources, it also requires any modulation for readout purposes to be applied within the sensing coil.

For phase modulation, we use an acousto-optic modulator. When placed asymmetrically in a coil of length L, following propagation through the sensing coil in both the CW and CCW directions, we see in Fig. 4.1 that the CCW path is modulated first, which introduces a τ delay to the CCW code relative to the CW path, where $\tau = nL/c$ is the coil transit time. Crucially, upon recombination at the coupler, both CW and CCW fields are frequency shifted, such that a homodyne readout is required.

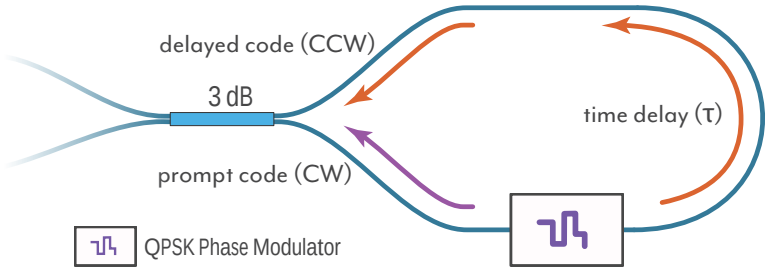

Figure 4.1: By using an asymmetrically placed acousto-optic phase modulator, the QPSK modulation results in two codes with a relative delay of τ encoded on the fields interfering on the photodetector. Using DEHoI to decode them then recovers the interference between the CW and CCW fields, enabling a measurement of the Sagnac phase.

We can write the CW and CCW fields using this formalism as follows:

$$E_{\mathrm{CW}}(t) = \tilde{E}(t)M(t)e^{i\omega t + i\phi_{\mathrm{CW}}(t)} \tag{4.3}$$

$$E_{\mathrm{CCW}}(t) = \tilde{E}(t)M(t-\tau)e^{i\omega t + i\phi_{\mathrm{CCW}}(t)} \tag{4.4}$$

We note that although there is a frequency shift due to the acousto-optic modulator, the shift is experienced by both CW and CCW paths, and the interference occurs at baseband. Thus, without loss of generality, we can write the frequency of the CW and CCW fields as ω. The superposition of the two returning fields at the 3dB coupler results is the sum of the clockswise and counterclockwise fields:

$$E_D = E_{\mathrm{CW}}(t) + E_{\mathrm{CCW}}(t) \tag{4.5}$$

$$= \tilde{E}(t)M(t)e^{i\omega t + i\phi_{\mathrm{CW}}(t)} + \tilde{E}(t)M(t-\tau)e^{i\omega t + i\phi_{\mathrm{CCW}}(t)} \tag{4.6}$$

At the photodetector, we take the complex conjugate squared of this superposition field and re-expand the modulation term M(t) into its constituent I and Q codes to obtain a DC term, and four encoded interference terms, along with their complex conjugates, at the photodetector:

$$\begin{aligned} P_D = & P_{sig} C_I(t) C_I(t-\tau) e^{i\Delta\phi} \\ & + P_{sig} C_Q(t) C_Q(t-\tau) e^{i\Delta\phi} \\ & - iP_{sig} C_Q(t) C_I(t-\tau) e^{i\Delta\phi} \\ & + iP_{sig} C_I(t) C_Q(t-\tau) e^{i\Delta\phi} \\ & + \text{C.C.} \\ & + 4P_{sig} \end{aligned} \tag{4.7}$$

where $P_{sig} \simeq |\tilde{E_{cw}}(t)\tilde{E_{ccw}}(t)|$ is the signal power on the detector assuming the Rayleigh scattered power is small, and C.C. stands for the complex conjugate of each of the terms. We have also rewritten the phase difference between clockwise and counterclockwise paths as $\Delta\phi(t) = \phi_{CW}(t) - \phi_{CCW}(t)$. Finally, using the Euler identity, we simplify the complex exponential terms:

$$\begin{aligned} P_D = \; & P_{sig} C_I(t) C_I(t-\tau) \cos(\Delta\phi(t)) && (I_{CW} \;\&\; I_{CCW}) \\ & + P_{sig} C_I(t) C_Q(t-\tau) \sin(\Delta\phi(t)) && (I_{CW} \;\&\; Q_{CCW}) \\ & - P_{sig} C_Q(t) C_I(t-\tau) \sin(\Delta\phi(t)) && (Q_{CW} \;\&\; I_{CCW}) \\ & + P_{sig} C_Q(t) C_Q(t-\tau) \cos(\Delta\phi(t)) && (Q_{CW} \;\&\; Q_{CCW}) \end{aligned} \tag{4.8}$$

Each of the terms in Equation 4.8 is encoded with the phase difference between the two paths $\Delta\phi$. For a rotation sensing Sagnac interferometer, this phase is the Sagnac phase and proportional to the rotation rate of the fiber loop. In this testbed system, the phase is an additional phase term injected by the acousto-optic modulator that is used to verify the digital interferometric readout. From Equation 4.8, by assuming that the chip frequency (on the order of MHz), is much faster than dynamics of the phase signal, we can also see that the detected power consists of only three discrete levels, P_{sig}, $-P_{sig}$, and 0. This is because the interference term created by homodyne DI is constructed from the difference between two four level codes.

In order to recover this phase, we construct codes with the appropriate delays, selectively ensuring that the code correlation is high for only the desired signals. We can construct these codes as follows:

$$\begin{aligned} II_{\text{decode}} &= C_I(t) C_I(t - \tau_{\text{decode}}) \\ IQ_{\text{decode}} &= C_I(t) C_Q(t - \tau_{\text{decode}}) \\ QI_{\text{decode}} &= C_Q(t) C_I(t - \tau_{\text{decode}}) \\ QQ_{\text{decode}} &= C_Q(t) C_Q(t - \tau_{\text{decode}}) \end{aligned} \tag{4.9}$$

To decode correctly, we set the correct decoding delay $\tau_{\text{decode}} = \tau$ equal to the transit time of the Sagnac coil. By multiplying each of the terms in Equation 4.8, with the appropriately delayed decoding terms in Equation 4.9, and following integration over a

code length, we are left with the four differential phase terms arising from Equation 4.8, each multiplied by a correlation constant of order unity.

Following demodulation we can then use a linear combination of these four measurements to construct an IQ projection for the actual measurement phasor:

$$\begin{aligned} s(t) &= \underbrace{(II + QQ)}_{\text{In-Phase (I)}} + \underbrace{i(IQ - QI)}_{\text{Quadrature (Q)}} \\ &= 2P_{sig}\cos(\Delta\phi) + 2iP_{sig}\sin(\Delta\phi) \end{aligned}$$

The phase difference $\Delta\phi(t)$ is then given by:

$$\Delta\phi(t) = \tan^{-1}\left(\frac{Q}{I}\right)$$

where I and Q are the phasor components obtained from the DEHoI readout. Using this method we are able to reconstruct the phase with a continuous, high dynamic range readout. This correctly decoded phase represents the interference between clockwise and counterclockwise modulated fields.

To see how scattered fields are rejected through this decoding process, consider a singly scattered field which experience a time delay $\tau_s \neq \tau_{\text{decode}}$, and thus an interference term with a code term $C(t-\tau_s)$. When correlated against a code with the correct decoding delay $C(t - \tau_{\text{decode}})$, the correlation constant is suppressed by a factor equivalent to the code length. This is effectively range-gating to suppress spurious interference due to residual scattering interactions, allowing a coherent source such as a laser to be used.

Additionally, by using an acousto-optic modulator, we further minimize the amount of coherent scattering effects from the interferometer, as scattered fields are either doubly frequency shifted, or not shifted at al

4.3 Experimental Demonstration

We use a JDSU (JDS Uniphase) diode laser with a linewidth of 1 MHz centered around 1550 nm. The fiber coupled output of this source is sent through a circulator and 3 dB splitter into the arms of the Sagnac interferometer as shown in Fig. 4.2.

Our DEHoI scheme uses an acousto-optic modulator to phase encode the two interferometer fields with a 4-level QPSK code. The use of an AOM enables polarization independent phase modulation, eliminating the need for polarization management within the Sagnac fiber coil.

For the modulation, we use an 11 bit m-sequence to generate the QPSK modulation, using two differently seeded linear feedback shift registers to generate orthogonal code pairs. The use of m-sequences as the generator codes therefore results in a QPSK modulation with a code length of 2047 chips (symbols). This is modulated onto the CW and CCW fields at a 2 MHz chip frequency, corresponding to a physical chip length in optical fiber of 100 m. Since the DeHoI readout requires averaging over a code length to recover the necessary

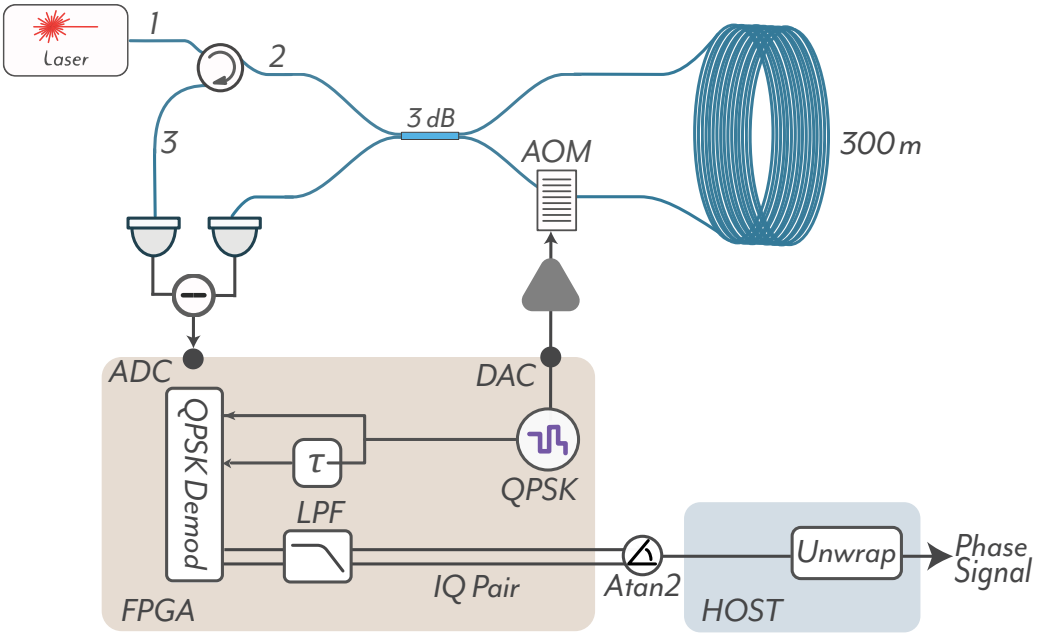

Figure 4.2: The experimental setup consists of a single acousto-optic modulator (AOM) asymmetrically placed in the Sagnac interferometer with a 300 m sensing coil of SMF-28e fiber. We use the AOM to modulate the QPSK code and provide a frequency shift of approximately +40 MHz to the optical fields. Both the modulation signal and the RF drive frequency are generated on an FPGA. In addition, we use the AOM to introduce a 12 Hz signal tone to demonstrate dynamic signal response. Photodetection was carried out using an Insight BPD1 balanced detector, and the signal was run into an ADC synchronous with the DAC. Following digitization by the ADC, the QPSK binning is used to demodulate the photodetected signal with prompt and coil delayed QPSK codes before averaging obtains the code correlation and output IQ data. The output data was converted into optical phase by computing the arctangent on a computer in post-processing.

autocorrelation, the final decimated sampling frequency of 977 Hz determines the phase readout bandwidth

The generation of the QPSK code and the 40 MHz AOM drive frequency are handled in parallel on a field programmable gate array (FPGA), with the AOM drive frequency being encoded digitally prior to conversion to the analog domain. In addition to the code, the FPGA adds flexibility to include phase and frequency modulation on top of the AOM drive frequency for calibration purposes.

We use a National Instruments, Virtex 5, 7965R FPGA with the analog interface provided by a NI 5781 transceiver. The transceiver operates at 100 MS/s on both the two input ADCs and 2 output DACs. This provides the I/O card with an effective 40 MHz bandwidth, capable of generating the necessary modulation of the AOM. After being output from the DAC, the signal is amplified using a Mini-Circuits ZHL-32A RF amplifier and sent to the AOM (IntraAction 40 MHz FCM-401E5A) placed at the start of the CCW arm.

The asymmetric placement of the modulator allows the modulation of the QPSK code at the start of the CCW direction of the fiber coil, and therefore at the end of the CW direction of the fiber coil. This means we are able to modulate the counter-propagating

beams with a differentially delayed QPSK code. For the CW beam, the code is therefore delayed by τ, where τ is the coil transit time, with respect to the CCW path. At the coupler, the two fields (and codes) interfere. An oscilloscope trace of the photodetector output demonstrating the code interference is shown here:

Figure 4.3: An oscilloscope trace of the DI Sagnac photodetector output with a 2 MHz chip frequency is shown. Excluding the ringing around chip transitions, we can see that there are 3 levels, at roughly 0, 400 mV, and 800 mV, corresponding to the interference of two four level codes.

The phase difference between the CW and CCW paths was then coherently extracted from a raw detected signal shown in Figure 4.3 by decoding for the CW-CCW code delay combinations shown in Equation 4.8.

The preliminary measurement of the Sagnac interferometer was to confirm the phase calibration of the readout. To do this, we tune the AOM RF frequency shift by the free spectral range (FSR) of the interferometer, which can be determined by the inverse of the Sagnac coil transit time of 1.5 µs, equivalent to 667 KHz Tuning the AOM frequency changes the differential optical phase accrued between the two counter-propagating beams, with a full FSR frequency shift (666 KHz) corresponding with a 2π phase change. By repeatedly scanning at the FSR depth sinusoidally, we see in Fig. 4.4 that the readout tracks over the expected 2π phase shift. This ensures that our digital interferometric readout outputs a correctly calibrated phase.

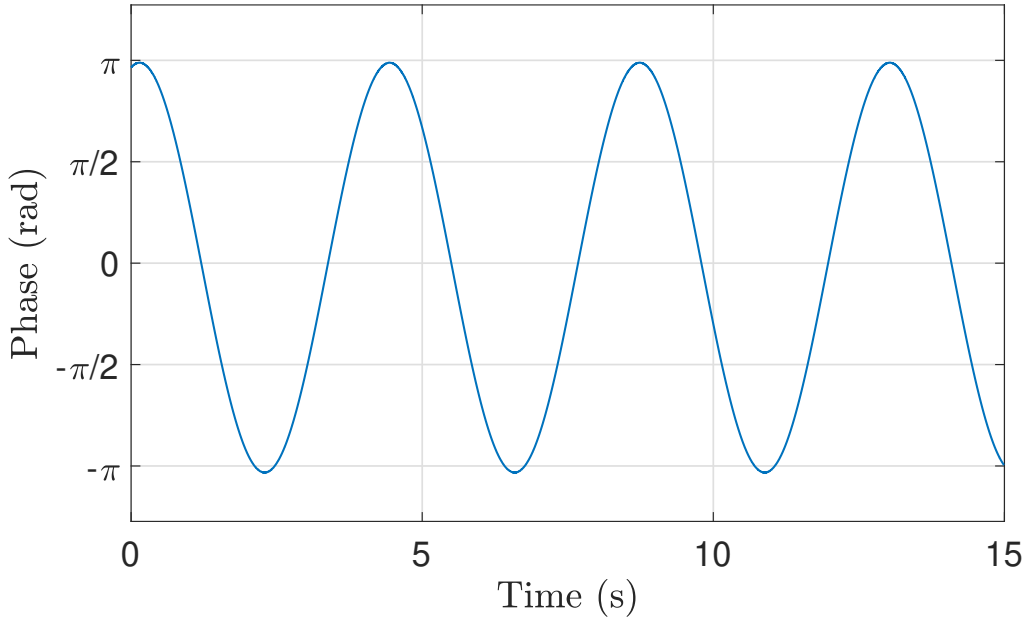

Figure 4.4: A time domain measurement showing the sinusoidal frequency modulation of the AOM RF drive frequency. This results in a phase scan in the readout with an expected magnitude of 2π. This was used to confirm the calibration of the DEHoI phase readout.

4.4 Noise Floor Analysis

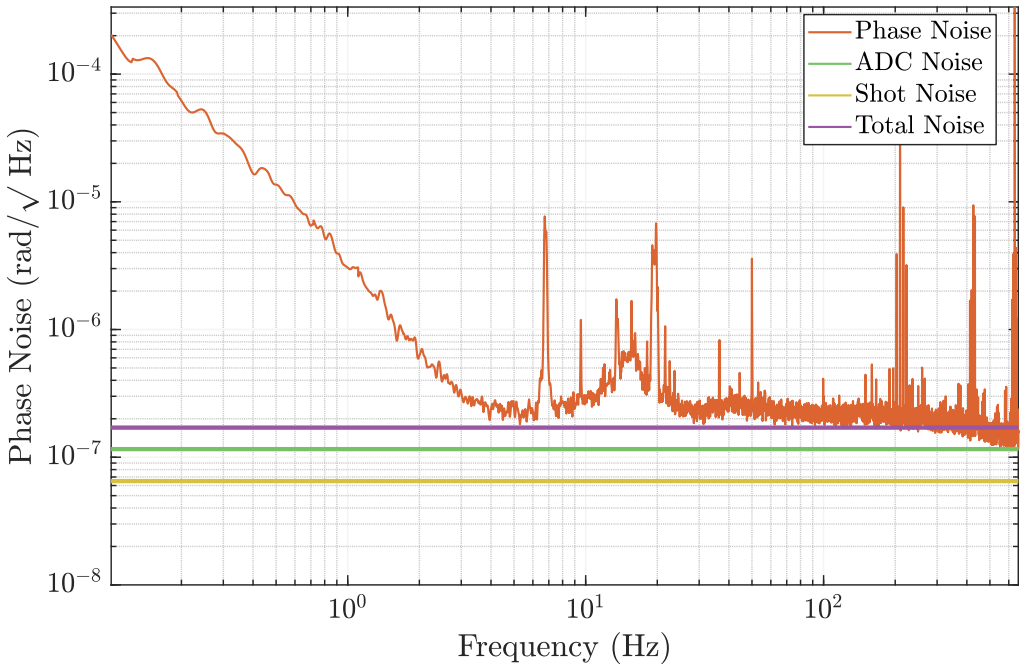

Figure 4.5: A frequency domain measurement of the noise floor of the DI Sagnac interferometer. The noise floor level is 0.2 µrad/$\sqrt{\text{Hz}}$. The two dominant sources of noise, ADC and shot noise, and their quadrature sum are also plotted.

Following calibration, we proceed to characterize the phase noise performance of the readout. In Fig. 4.5, we plot the amplitude spectral density computed from a time series measurement, showing the phase sensitivity of the Sagnac interferometer phase readout of 0.2 µrad/$\sqrt{\text{Hz}}$ above approximately 10 Hz. In order to determine that we are not limited by noise due to the digital interferometric phase extraction scheme, we perform a noise budget analysis. We begin with shot noise, a fundamental noise source due to discrete arrival times of photons on the photodetector. The voltage noise due to shot noise out of the photodetector, and as seen by the ADC is obtained by the following [78]:

$$\begin{aligned}\Delta V_{\text{shot}} &= \alpha\sqrt{2e\eta P}T_G \\ &= 0.14\sqrt{2(1.6\times10^{-19}\text{ C})(1.176\text{ A/W})(7\times10^{-4}\text{ W})}\,(5000\text{ V/W}) \\ &= 13.2\text{ nV}/\sqrt{\text{Hz}}\end{aligned} \tag{4.10}$$

where e denotes the electron charge, α denotes the unitless electronic attenuation factor of 0.14 required to step the photodetector voltage output down to match the 1 V ADC input voltage range, η denotes the quantum efficiency of InGaAs at 1550 nm of approximately 1.176 amp per watt, P denotes the total optical power on the detector of 700 microwatts, and T_G denotes the transimpedance gain of the Insight Balanced Photodetector, which is 5 volts per milliwatt.

A second source of noise in photodetection is dark noise, which is inherent to the p-i-n type photodiodes used here. In these photodiodes, a photocurrent is generated when an photon is incident on the depletion layer of a p-n junction [79]. However, even when there are no incident photons (dark), a small dark current is generated due to leakage of charge

carriers across the junction. The dark current is usually quoted in spectral density units of noise-equivalent power (NEP), or W/$\sqrt{\text{Hz}}$, as this reflects the detection of 'phantom' photons.

We can convert noise-equivalent power to voltage noise spectral density in order to match the units of shot noise given in 4.10. This is done by multiplying the NEP by the photodetector transimpedance gain. Thus, the voltage noise contribution from dark noise as seen at the ADC is calculated as follows:

$$\begin{aligned} \Delta V_{\text{dark}} &= \alpha \text{NEP}_{\text{Insight}} T_G \\ &= (0.14)(4 \times 10^{-12}\ \text{W}/\sqrt{\text{Hz}})(5000\ \text{V/W}) \\ &= 2.8\ \text{nV}/\sqrt{\text{Hz}} \end{aligned} \tag{4.11}$$

where $\text{NEP}_{\text{Insight}}$ is the noise equivalent power or dark noise of the Insight Balanced Photodetector of 4×10^{-12} W/$\sqrt{\text{Hz}}$, as quoted on the specifications [80]. The dark noise contribution works out to be quite small, as it is also electronically attenuated by a factor of α.

Finally, the 5781 ADC front end voltage noise ΔV_{ADC} is estimated from the specification sheet as 25 nV/$\sqrt{\text{Hz}}$ [81]. This is a form of quantization noise that reflects the bitwidth limited precision in the conversion from analog to digital signals. Since all three noise sources are uncorrelated, we add them in quadrature to find the total voltage noise on the signal:

$$\Delta V_{\text{total}} = \sqrt{\Delta V_{\text{shot}}^2 + \Delta V_{\text{Dark}}^2 + \Delta V_{\text{ADC}}^2} = 28.4\ \text{nV}/\sqrt{\text{Hz}} \tag{4.12}$$

To calibrate this total voltage noise to phase noise in radians per root hertz, we multiply by a calibration factor of 2π rad/V, since we assume that the 1 V dynamic range of the ADC is mapped to a full 2π radians in phase - in other words we have full optical fringe visibility. In this case, one period of an interference fringe with a peak-to-peak amplitude of 1 volt corresponds to 2π radians in phase. We thus obtain for a phase noise estimate:

$$\Delta\phi = \Delta V_{\text{total}}(2\pi) = (27.3\ \text{nV}/\sqrt{\text{Hz}})\ (2\pi\ \text{rad/V}) = 1.78 \times 10^{-7}\ \text{rad}/\sqrt{\text{Hz}} \tag{4.13}$$

Our current noise floor of 2×10^{-7} rad/$\sqrt{\text{Hz}}$ is superimposed with these noise estimates in Figure 4.5 below. In this figure, we have taken the individual ADC, shot noise, and dark noise estimates in units of nV/$\sqrt{\text{Hz}}$ and converted them to units of rad/$\sqrt{\text{Hz}}$ using the 2π rad/V calibration factor.

From Figure 4.5, the predicted shot noise limited phase sensitivity for this measurement is 0.1 µrad/$\sqrt{\text{Hz}}$, a factor of four below our experimentally obtained results. Analog front end electronic noise currently dominates our experimental sensitivity at approximately 0.4 µrad/$\sqrt{\text{Hz}}$. The broad noise features around 10 Hz are due to optical table mechanical resonances. At frequencies below approximately 5 Hz, the noise floor is seen to roll up caused by the AOM thermal phase noise coupling into the Sagnac phase due to its asymmetric position within the interferometer.

From an accounting of the these noise sources, we have demonstrated that the noise floor of the digital homodyne phase extraction scheme is limited by ADC noise and shot noise, and not by the phase extraction scheme itself, or noise driven by scattering, as commonly seen in fiber optic gyroscopes.

4.5 Conclusion

In this chapter, we introduced a Sagnac interferometer with a DeHoI readout, a variant of Digital Heterodyne interferometry. Using this readout scheme, we are able to suppress phase noise due to spurious scattering effects within the interferometer. We have also demonstrated shot noise and ADC noise limited performance of digital interferometry in the Sagnac interferometer. This allows us to reach a phase noise floor of $2 \times 10^{-7}\,\mathrm{rad}/\sqrt{\mathrm{Hz}}$, serving as a good proof of concept for a digitally enhanced Sagnac interferometer. By adding a calibration tone to the acousto-optic modulator frequency, we also demonstrated that we could recover a signal injected inside the loop. From here, we consider placing a spectroscopic analyte within the loop, with the dispersion induced phase shift serving as the phase signal. In the next chapter, by integrating a fiber coupled vapor cell into the loop, we demonstrate the recovery of an analyte induced phase shift.

5

Dispersion Spectroscopy with a Sagnac Interferometer

This chapter is based on work published in *Optics Letters* titled "Digitally enhanced molecular dispersion spectroscopy" [82].

In the previous chapter, we introduced the Sagnac interferometer architecture as an ideal proving ground for digital interferometry, due to its balanced arm lengths leading to excellent stability, and first order immunity to frequency and path length noise. This resulted in a phase noise floor of $2 \times 10^{-7}\,\mathrm{rad}/\sqrt{\mathrm{Hz}}$, purely limited by front end electronic and shot noise. In this chapter, we leverage this proven phase extraction method, along with the low-noise Sagnac interferometer architecture to extract dispersion induced phase shifts. As our test analyte, we use Hydrogen Cyanide (HCN), a commonly reference used to evaluate the performance of techniques in near-infrared laser spectroscopy.

This is a field that has seen widespread use and development in recent years due to its ability to perform highly sensitive atmospheric and in-situ measurements of trace gas concentrations [6, 7]. Here, we briefly review the two differing approaches to laser spectroscopy of molecules: absorption which measures a change in field amplitude, as the laser is swept across the absorption line, and dispersion, which measures a change in the phase of the field. As shown in Chapter 3, this phase shift is proportional to the refractive index change, or anomalous dispersion around an absorption line. By measuring dispersion instead of absorption, dispersion spectroscopy avoids the need to calibrate acquired spectra for power fluctuations as the laser frequency is tuned.

From Chapter 2, we provided a heuristic proof that dispersion is linearly proportional to concentration, in contrast to absorption, which follows the exponential Beer-Lambert Law. Dispersion methods therefore circumvent the sensitivity limits of amplitude methods when performing high concentration measurements, enabling a large measurement dynamic range [83], with zero baseline, as the signal rises from zero, with increasing concentration. However, phase shifts measured in dispersion spectroscopy are relatively small.

Thus, highly stabilized and isolated components are required to extract these phase shifts, adding hardware complexity to the interferometric system. Existing methods for dispersion spectroscopy, such as Chirped Laser Dispersion Spectroscopy (CLaDS) [17, 84] and Heterodyne Phase Sensitive Dispersion Spectroscopy (HPSDS) [85, 86] rely on optical heterodyning to achieve this, and typically yield phase sensitivities on the order of a milliradian. In this chapter, we present a new homodyne dispersion spectroscopy method using

Digitally Enhanced Homodyne Interferometry (DEHoI) as a phase extraction technique with better than μrad phase sensitivity.

This is accomplished by integrating a vapor cell containing our analyte (HCN) into the Sagnac interferometer, and interrogating it using Digitally Enhanced Homodyne Interferometry. The architecture benefits from first order immunity to laser frequency noise due to matched optical path lengths within the Sagnac interferometer, enabling a frequency agile dispersion spectroscopy system that requires no active stabilization. In addition, utilising a balanced photo-detector subtracting the optical power of the symmetric and anti-symmetric outputs of the Sagnac interferometer provides a high degree of relative intensity noise immunity. The combined suppression of both frequency and relative intensity noise in our readout relaxes the stability requirements on the laser to achieve a highly sensitive noise immune phase readout enabling the use of a free running diode laser with a linewidth of approximately 10 MHz.

5.1 Experimental Concept

A conceptual diagram of our dispersion spectrometer, along with a sketch of an idealized dispersion profile near a molecular transition is shown in Fig. 5.1.

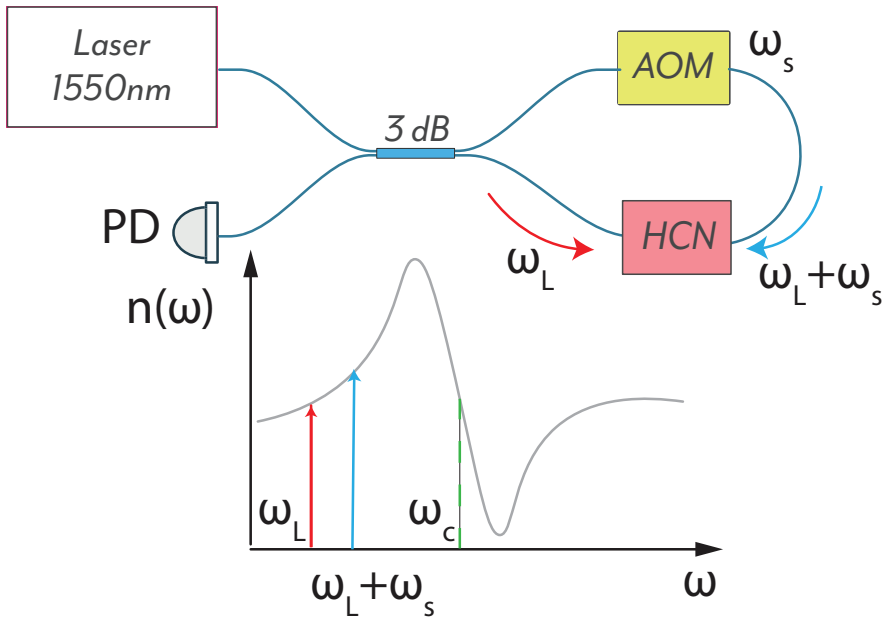

Figure 5.1: An optical tone of frequency ω_L with linewidth much narrower than a HCN molecular transition is split by a 3 dB coupler and injected into a loop in clockwise and counterclockwise directions. The clockwise path enters an AOM and is frequency shifted by ω_s before entering a vapor cell containing HCN with a molecular transition at a center frequency ω_c. The counterclockwise path immediately enters the vapor cell unshifted. The two frequencies propagating within the loop interrogate the dispersion $n(\omega)$ of the molecular transition at different frequencies. The clockwise and counterclockwise fields thus experience different phase shifts. When recombined at the coupler, the two fields interfere, and the resulting signal is recorded by a photodetector (PD).

In this configuration, a single optical tone is split into clockwise and counterclockwise paths around a common path closed loop Sagnac interferometer. The clockwise path experiences a frequency shift induced by an acousto-optic modulator (AOM) before entering

a Hydrogen Cyanide (HCN) vapor cell. The counterclockwise path immediately enters the vapor cell unshifted and is only frequency shifted after it exits the vapor cell. The vapor cell is thus interrogated by two optical frequencies, each experiencing a different phase shift corresponding to the dispersion profile of the molecular transition of interest. The two fields exit the loop however, at the same shifted optical frequency. Thus, when the two counterpropagating fields are recombined at the coupler and observed with a photodetector, their interference results in a baseband signal whose phase is equal to the differential dispersion experienced by the two fields. As the laser frequency is swept across the molecular transition, this differential phase shift can be extracted using interferometric methods, allowing the dispersion profile corresponding to the molecular transition to be reconstructed. Importantly, since the clockwise and counterclockwise paths in the interferometer are necessarily length matched, the differential phase signal will be immune to laser frequency noise.

We also distinguish this differential dispersion signal from that obtained with Differential Optical Dispersion Spectroscopy [21], where a second vapor cell is placed in the reference arm of a CLADs Mach Zehnder Interferometer setup, serving as a spectroscopic reference. In this configuration, both the signal and reference vapor cells are sampled at the same optical frequency, with one interferometer arm frequency shifted by an AOM afterwards to form a heterodyne readout. By contrast, for the Sagnac setup presented here, a vapor cell is sampled at two different frequencies, but interfere at the *same* frequency, forming a homodyne readout.

5.2 Differential Phase Signal

As the laser center frequency ω_l is swept across the transition, the counterclockwise and clockwise fields in the loop interferometer experience differing phase shifts given respectively by Equation 5.1 and Equation 5.2:

$$\phi_{CCW} = \frac{\omega_l n(\omega_l) l_{cell}}{c} \tag{5.1}$$

$$\phi_{CW} = \frac{(\omega_l + \omega_s) n(\omega_l + \omega_s) l_{cell}}{c} \tag{5.2}$$

where ω_l is the center frequency of the laser, ω_s is the frequency shift induced by the AOM, n is the frequency dependent refractive index of the HCN sample, and l_{cell} is the length of the vapor cell. The counterclockwise and clockwise fields, when recombined at the coupler, can then be expressed by the following:

$$E_{CCW} = \frac{E}{2}\alpha(\omega_l)\exp\left[i(\omega_l + \omega_s)t + i\phi_{CCW}\right] \tag{5.3}$$

$$E_{CW} = \frac{E}{2}\alpha(\omega_l + \omega_s)\exp\left[i(\omega_l + \omega_s)t + i\phi_{CW}\right] \tag{5.4}$$

where $\phi_{ccw}(\omega)$ and $\phi_{cw}(\omega)$ are the optical phase shifts induced by the vapor cell at the laser frequency and the shifted frequency, and $\alpha(\omega)$ are the frequency dependent absorption coefficients experienced by the counter-propagating fields that modulate their amplitude

E. The sum of these fields incident on a square law photodetector is then converted into a voltage signal P with three terms:

$$P = \frac{E^2}{4}\alpha^2(\omega_l + \omega_s) + \frac{E^2}{4}\alpha^2(\omega_l) + \frac{E^2}{4}\alpha(\omega_l + \omega_s)\alpha(\omega_l)\cos(\Delta\phi) \tag{5.5}$$

where $\Delta\phi = \phi_{CCW} - \phi_{CW}$ has been defined as the differential phase between the frequency shifted and unshifted fields.

The first two terms of Equation 5.5 are terms at DC resulting from the frequency dependent absorption. The third term carries the interference between the clockwise and counterclockwise fields due to the differential dispersion induced phase shift $\Delta\phi$ experienced by the counterpropagating paths. An expression for this phase shift can be derived by combining Eqns. 5.1, and 5.2:

$$\Delta\phi = \frac{l_{cell}}{c}[(\omega_l + \omega_s)n(\omega_l + \omega_s) - \omega_l n(\omega_l)] \tag{5.6}$$

$$\approxeq \frac{\omega_l l_{cell}}{c}[n(\omega_l + \omega_s) - n(\omega_l)] \tag{5.7}$$

where we have made the approximation $\omega_s << \omega_l$, as the radio frequency AOM shift MHz is much smaller than the optical frequency. As the laser frequency ω_l is swept across the molecular transition, the phase shift (Equation 5.7) encodes the dispersion profile of the transition. This phase shift for a frequency shift of 40 MHz and a linewidth of 1 GHz, is plotted in Figure 5.2 below. Qualitatively, for this set of parameters, we see that the signal corresponds approximately to the derivative of the dispersion profile. This is clear when we consider that the phase shift in Equation 5.7 results from sampling the dispersion curve at two points, and taking their difference.

Using a phase sensitive detection method like DeHoI, the interferometric phase shift can be recovered as a phase signal. The phase signal amplitude will also increase as a function of the AOM frequency shift ω_s up to approximately the half width half maximum of the spectral feature. At this maximum phase point, the laser frequency and its shifted component line up exactly with the frequency spacing between the maximum and minimum of the dispersion profile. Beyond this point, the amplitude of the phase signal drops off, corresponding to the tails of the anomalous dispersion curve. This effect is explained in more detail and modelled in a later section of this chapter. We also note that since the refractive index variation scales proportionally to species concentration, by the linearity of Equation 5.7, the phase shift will also scale linearly with concentration.

The interferometric phase shift is extracted using digitally enhanced homodyne interferometry (DeHoI) [39]. In the implementation of DeHoI used here, similar to our testbed system introduced in the previous chapter, the frequency shifting AOM is also used to encode the optical fields with two orthogonal PRBS codes at a modulation frequency which is known as the chip frequency. This phase modulation is in addition to the frequency shift imparted onto the clockwise (CW) and counterclockwise (CCW) optical fields. The orthogonality of the PRBS codes form an orthonormal basis on the complex phase plane on which the in-phase and quadrature components of the fields are projected. This four level phase shift is known as Quadrature Phase Shift Keying (QPSK) and takes on the

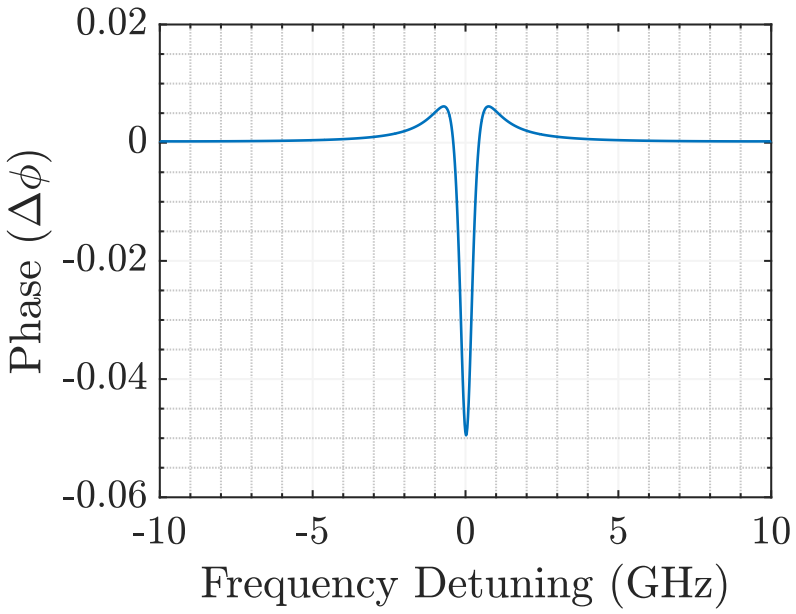

Figure 5.2: The dispersion induced phase signal for a Lorentzian absorption line with a full width half maximum of 1 GHz, an AOM shift of 40 MHz, and a vapor cell length of 16.5 cm. The curve is obtained by plugging these parameters into Equation 5.7

function of a heterodyne frequency scanning four quadratures of the phase plane. We insert this modulation into the field calculation as follows:

$$E_{\mathrm{CW}}(t) = \tilde{E}(t)M(t)\exp[i(\omega_L+\omega_s)t + i\phi_{\mathrm{CW}}(\omega_L)] \tag{5.8}$$

$$E_{\mathrm{CCW}}(t) = \tilde{E}(t)M(t-\tau)\exp[i(\omega_L+\omega_s)t + i\phi_{\mathrm{CCW}}(\omega_L+\omega_s)] \tag{5.9}$$

where we have adopted the same convention introduced in the previous chapter, with M(t) being a compound code formed from the sum of two orthogonal PRBS sequences. The clockwise field is immediately encoded with the code, but the counterclockwise field passes first through the vapor cell and the Sagnac loop, introducing a relative delay in the QPSK modulation between the two paths. Upon interference at the photodetector, the resulting signal must be demodulated with the appropriately time delayed compound codes. Doing so recovers the in-phase and quadrature components of the interference, allowing the dispersion induced phase shift between the interfering CW and CCW fields to be extracted at a sample rate equal to the repetition frequency of both PRBS codes. The explicit calculation of the demodulation process is given in the previous chapter.

The auto-correlation properties of PRBS sequences also ensure that spurious scattered fields with different time delays are rejected during demodulation, resulting in the suppression of both coherent phase noise due to fiber backscattering as well as etalon effects in the vapor cell.

5.3 Experimental Implementation

A schematic of the initial experimental demonstration is shown in Fig. 5.3. A tunable JDSU DFB laser diode with 10 MHz linewidth is used to interrogate the 1550.515 nm P11 Hydrogen Cyanide vibrational absorption line. For this, we use a fiber coupled $H^{13}CN$ vapor cell with a pressure of 25 Torr at room temperature, and a path length of 16.5 cm produced by Wavelength References. The vapor cell is housed within a Sagnac interferometer with an anti-symmetrically placed, polarization-insensitive acousto-optic modulator (AOM). Here, the clockwise (CW) path immediately enters the vapor cell unshifted while the counter-clockwise (CCW) path first passes through an AOM and experiences a 120 MHz frequency shift. This ensures that the CW and CCW paths through the vapour cell have different frequencies, and produce a differential phase shift at the interferometer output. In addition, we use the AOM to apply the DEHoI phase modulation with a chip frequency of 2 MHz. The AOM drive, consisting of the RF carrier and the DEHoI phase modulation are both generated on a NI 7954 FPGA and output using a NI 5781 transceiver.

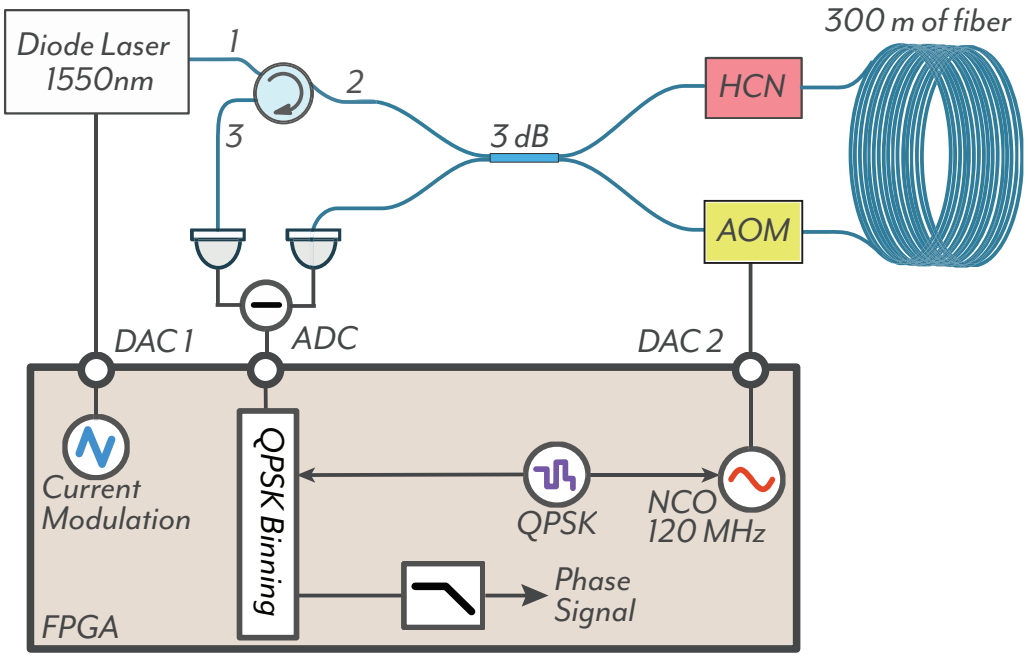

Figure 5.3: A 1550 nm tunable DFB laser diode output is used to interrogate a Sagnac interferometer containing an anti-symmetrically placed HCN vapour cell and AOM. The modulator applies a frequency shift to the CCW path relative to the CW path as they interrogate the vapour cell, allowing the HCN dispersion profile to be interrogated at two optical frequencies. Both paths also experience DEHoI phase modulation which enables measurement of the differential phase caused by the HCN dispersion profile. The length of fiber was used to add a relative delay between the CW and CCW DEHoI modulation to ensure complete and correct decoding. To scan the dispersion profile, the laser wavelength is swept across the HCN transition by modulating the injection current of the laser diode. Note that all optical components downstream from the laser diode output used were polarization independent including optical fiber – SMF28e, optical circulator, the 3dB coupler, the AOM and HCN cell.

Following recombination at the 3dB coupler, an Insight Balanced photodetector with 400 MHz bandwidth, in conjunction with an optical circulator subtracts the symmetric and anti-symmetric Sagnac outputs to provide relative intensity noise suppression. The photodetector measures the spread-spectrum DEHoI modulation containing the differential phase information from the HCN dispersion profile, which is digitized using the NI 5781 transceiver card, and demodulated on the FPGA. The demodulation decodes the DEHoI modulation based on the code time-of-flight of the CW and CCW paths with respect to the AOM. Due to the asymmetric positioning of the AOM within the Sagnac interferometer, the code time-of-flight is given by the transit time of the Sagnac coil. Provided the transit time exceeds the DEHoI chip period, it can be resolved and correctly decoded. Therefore, increasing the DEHoI modulation frequency, and thereby reducing the symbol period thus decreases the necessary transit time for correct decoding and can enable the use of a shorter Sagnac coil.

To interrogate the full width of the dispersion profile, the laser frequency is swept using the current modulation port of an ILX Lightwave 3724B Laser Diode Controller driven by a triangle wave generated on the FPGA and output through a second DAC. While scanning the laser frequency over the HCN transition, the output of the Insight Balanced photodetector is read into an ADC on the FPGA where the appropriately delayed codes are used to demodulate and recover the phase signal modelled by Equation 5.7. To frequency tune across the transition, we use a slow sub-hertz scan frequency. This is possible due to the common path configuration of the Sagnac interferometer, conferring immunity of the readout to laser frequency noise during the scan. In doings so, the readout can be averaged to improve the spectroscopic sensitivity.

5.4 Spectroscopic Signal

A spectroscopic measurement of the P11 in the $2\nu_3$ rotational-vibration band of $H^{13}C^{14}N$ is made with a 200 ms averaging window. Using measurements made by Swann and Gilbert on the pressure broadening coefficient of the HCN P and R branch lines [66], a theoretical ab initio phase signal for the HCN vapor cell under experimental temperature and pressure conditions is also computed from the model described by Equation 5.7, where a Voigt lineshape is used to numerically compute the dispersion profile $n(\omega)$ [87]. At 25 torr, the resulting 2.3 GHz Voigt linewidth of the transition is dominated by pressure broadening, with only a small contribution due to Doppler broadening. With this Voigt lineshape as the model, the experimental vs. theoretical phase signal are overlaid in Fig. 5.4.

From Fig. 5.4a, the measured dispersion displays good agreement with the ab initio dispersion data over the absorption line. However, we see a linear phase ramp of approximately 2 mrad across the 10 GHz laser frequency scan range in the experimental data. This leads to a systematic downward sloping residual visible in the absorption line tails, as shown in Fig. 5.4b:

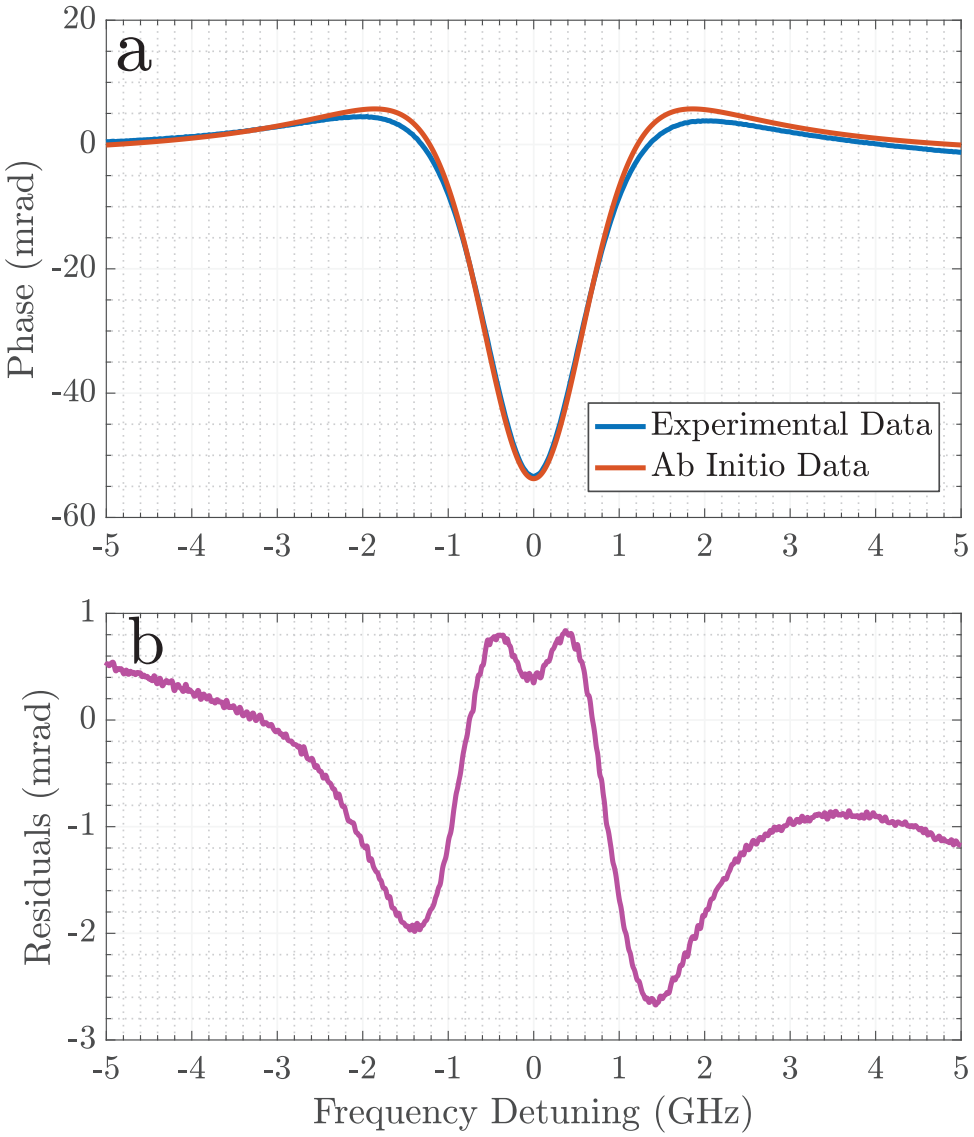

Figure 5.4: The experimental phase signal, and the theoretical phase signal generated from the model using experimental pressure and temperature conditions are plotted in subplot Fig. 5.4a. The x-axis is shifted such that the phase signal is centered at the linecenter of the P11 transition. The residuals are plotted in subplot Fig. 5.4b.

5.5 Fiber Dispersion

To investigate the cause of this residual, we begin by verifying that this systematic phase error is not driven by chromatic dispersion in the 300 m long fiber spool. Such an error would cause an additive parasitic signal on top of the vapor cell induced signal.

Dispersion spectroscopy introduces a nonreciprocal phase shift into a Sagnac fiber coil in order to measure the differential dispersion of a spectroscopic sample. However, this also results in a differential measurement of the chromatic dispersion of the fiber Sagnac coil. If the dispersion had a constant slope (only group delay), the differential phase shift as the laser frequency is scanned would be constant, resulting in only a DC phase on top of the spectroscopic phase. However, if the dispersion slope changes (this is called group velocity dispersion or second order dispersion) [88], there will be an additional varying phase shift

on top of the spectroscopic phase due to the fiber loop, as the curvature of the dispersion varies across the scanning range of the laser. In other words, if the frequency dependent refractive index of fiber has some nonlinear behavior like a molecular dispersion profile, there will be a spurious phase shift, because the derivative is non-zero.

Here, we calculate the expected phase shift contribution for a given length of fiber from its group velocity dispersion coefficient D, commonly given in units of $\mathrm{ps\,nm^{-1}\,km^{-1}}$. For this thesis, we use SMF28 fiber, which has the following wavelength dependent dispersion coefficient [89]:

$$D(\lambda) = \frac{S_0}{4}\left[\lambda - \frac{\lambda_0^4}{\lambda^3}\right] \tag{5.10}$$

where

$$S_0 \leq 0.092\,\mathrm{ps\,nm^{-2}\,km^{-1}} \tag{5.11}$$
$$\lambda_0 = 1310\,\mathrm{nm}. \tag{5.12}$$
$$\lambda = 1550\,\mathrm{nm}. \tag{5.13}$$

We first convert both parameters S_0 and λ_0 to SI units, using SI units throughout. In addition, to make calculations easier, we convert Equation 5.10 such that it is frequency instead of wavelength dependent:

$$D(f) = \frac{S_0}{4}\left[\frac{c}{f} - \frac{cf^3}{f_0^4}\right] \tag{5.14}$$

As the dispersion coefficient is frequency dependent, the dispersion coefficients at the shifted and unshifted frequencies will be different. To quantify this difference, we convert the wavelength of the unshifted and shifted fields to units of frequency:

$$f = \frac{c}{\lambda}. \tag{5.15}$$
$$f_s = f + 120\mathrm{MHz}. \tag{5.16}$$
$$\tag{5.17}$$

We then evaluate the dispersion coefficient D at the unshifted frequency f, and the shifted frequency f_s:

$$D = D(f).$$
$$D_s = D(f_s).$$

We can convert D and D_s into group delay dispersion per unit length $\frac{\partial^2 k}{\partial \omega^2}$ with the following relation [90]:

$$\frac{\partial^2 k}{\partial \omega^2}\Big|^{\text{unshifted}} = \frac{D\lambda^2}{2\pi c} \tag{5.18}$$

$$\frac{\partial^2 k}{\partial \omega^2}\Big|^{\text{shifted}} = \frac{D_s\lambda^2}{2\pi c} \tag{5.19}$$

where k is the wavenumber of light propagating through the fiber.

We take the difference between Equations 5.18 and 5.19 to obtain the difference in group delay dispersion per unit length across the AOM frequency shift

Multiplying by the length of the coil L of 300 meters, we obtain the difference in group delay dispersion ΔD_2:

$$\Delta D_2 = \frac{\partial^2 \phi}{\partial \omega^2} = L\left[\frac{\partial^2 k}{\partial \omega^2}\Big|^{\text{unshifted}} - \frac{\partial^2 k}{\partial \omega^2}\Big|^{\text{shifted}}\right] \tag{5.20}$$

To obtain the differential phase shift, we integrate Equation 5.20 twice, yielding:

$$\Delta\phi = \frac{\Delta D_2}{2}\Delta\omega^2 \tag{5.21}$$

where $\Delta\omega$ is the angular frequency over which the laser is swept

$$\Delta\omega = 2\pi \times 10\ \text{GHz} \tag{5.22}$$

Combining Equations 5.21 and 5.22, along with the constants S_0, and λ_0 we finally obtain a phase shift:

$$\Delta\phi = 10\ \text{nrad} \tag{5.23}$$

as the laser frequency is swept along the dispersion profile of the 300 m long SMF28 fiber spool. We note that this is the "worst case" phase shift assuming the zero dispersion slope S_0 in Equation 5.11 is its maximum value of $0.092\,\text{ps}\,\text{nm}^{-2}\,\text{km}^{-1}$.

Given that the residual observed in the spectroscopic measurement is on the order of milliradians, we can rule out chromatic dispersion of the fiber as the cause. Instead, we hypothesize that the phase residual is driven by the nonlinearity of the frequency scan as the laser frequency is scanned. However, as this effect induces a deterministic phase ramp in the spectroscopic readout it can be readily calibrated out in post-processing. In the work presented in the subsequent chapter, we also demonstrate a real time method of tracking and linearizing the frequency scan.

5.6 Concentration Sensitivity

To determine the sensitivity of the spectroscopic phase measurement, a ten minute off resonance measurement is taken where the laser diode is temperature tuned away from the transition, measuring solely the intrinsic noise of the phase measurement. This is equivalent to the noise measurement performed in the DI testbed system from the previous chapter. From this, we compute the DEHoI noise floor as determined by the off resonance phase spectral density, shown in Fig. 5.5. This shows a minimum readout noise floor of 0.8 μrad/$\sqrt{\text{Hz}}$.

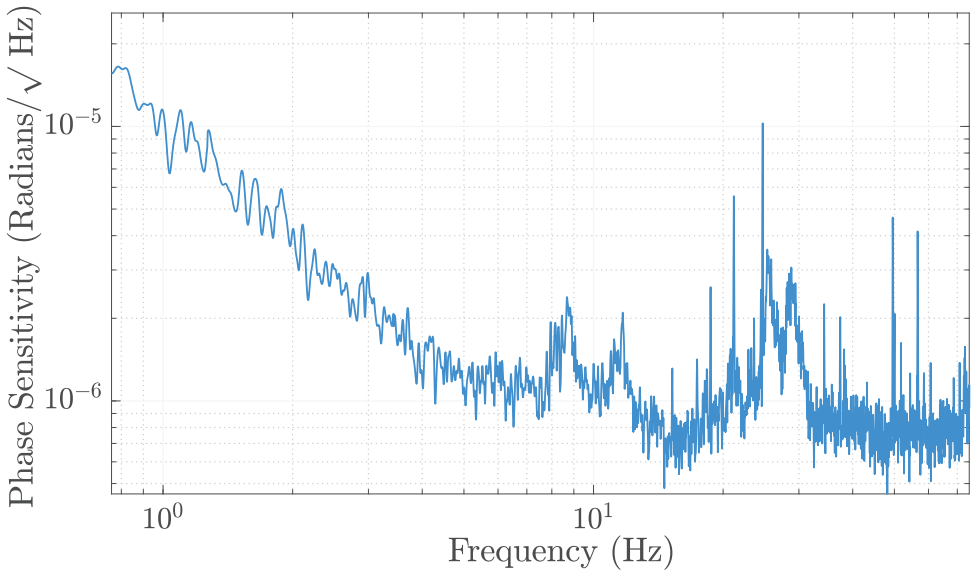

Figure 5.5: The sensitivity of the spectroscopic measurement is given by the DEHoI readout phase spectral density. This is measured by tuning the laser diode off resonance such that the characteristic phase signal is not obtained and only phase excursion due to noise is measured. This phase noise floor is seen to reach a minimum of 0.8 μrad/$\sqrt{\text{Hz}}$.

To determine the concentration sensitivity of digitally enhanced dispersion spectroscopy, the phase noise value must be converted to units of parts per million, or billion. We use as the starting point the phase noise spectral density of the off-transition data, as shown in Fig. 5.5, where the phase sensitivity above 30 Hz was measured to be 0.8 μrad/$\sqrt{\text{Hz}}$.

In order to determine the concentration sensitivity, we recall the Equation to obtain spectroscopic concentration in derived in Chapter 2:

$$C = \frac{N_g}{N_0} = \frac{k_B T_0}{P_0} \frac{P}{k_B T} \tag{5.24}$$

where T_0 and P_0 are standard temperature and pressure. Substituting the parameters of the vapor cell used here (25 Torr), at 293 Kelvin, we obtain a value of 0.03, or 30,000 parts per million. Since we measure through a column of gas in a vapor cell, and not a point source, we then proceed to multiply by the length of the vapor cell (16.5 cm) to obtain a path integrated concentration of 5463 ppm meter. From Fig. 5.4a, we see that this concentration yields a spectroscopic phase signal of 60 mrad.

This sets a calibration factor of 91 ppm-meter per mrad for a dispersion signal. Since the spectroscopic phase signal scales linearly with concentration as demonstrated in Equation 5.7, we convert our phase noise spectral density to units of mrad/$\sqrt{\text{Hz}}$, scale by the calibration factor, and then multiply by one thousand, to give a detection sensitivity scaled to units of ppb $\times$ m/$\sqrt{\text{Hz}}$. In performing this calibration, we arrive at a noise equivalent detection limit of 77 ppb $\times$ m/$\sqrt{\text{Hz}}$.

5.7 Sensitivity Dependence on Frequency Shift

As discussed earlier, it is possible to increase the detection sensitivity limit further by increasing the AOM frequency shift, or by cascading multiple AOMS, such that the phase signal is maximized for a fixed phase sensitivity limit, increasing the SNR of the spectrometer. This occurs when the frequency shift is optimized to the linewidth of the desired absorption line. Since the phase signal is a differential dispersion readout, the amplitude of the phase signal increases with frequency shift until this shift becomes larger than the width between the peak and the trough of the dispersion profile. In the following Figure 5.6, we have described these two cases as the optimal frequency shift, and the "overshot frequency shift".

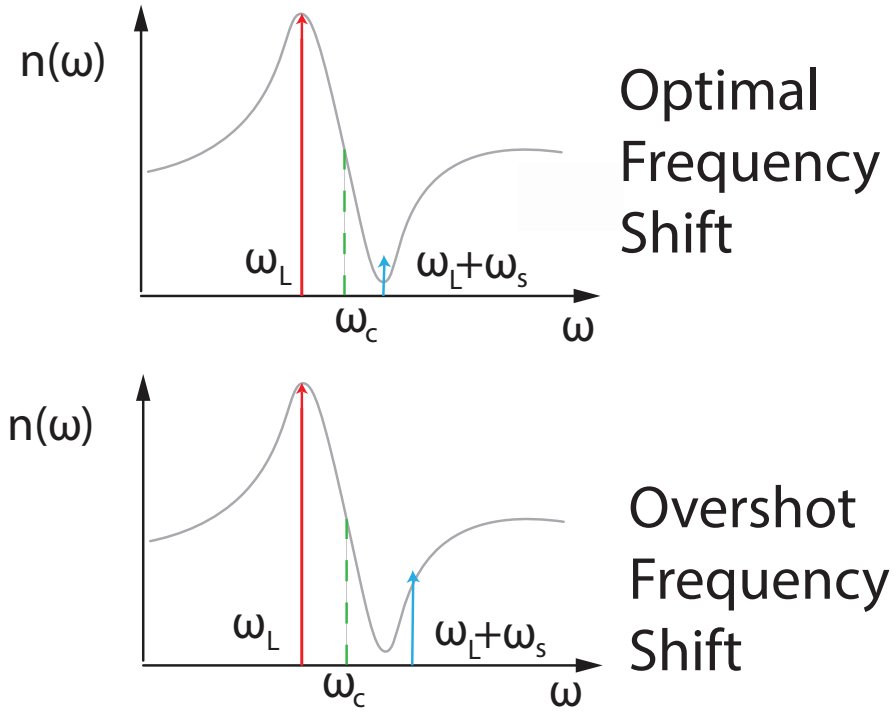

Figure 5.6: Two cases for the AOM frequency shift that demonstrate the optimal or maximized phase signal, and an "overshot" frequency shift. In the optimal case, the signal is maximimized, as the laser frequency, and its shifted frequency sample the peak and trough of the dispersion feature. In the overshot case, the shifted frequency has gone beyond the trough.

We can express this dependence analytically from the equation for the dispersion phase signal:

$$\Delta\phi(\omega_s) \propto 2\frac{\omega_c l_{cell}}{c}[n(\omega_c+\omega_s)-n(\omega_c)] \tag{5.25}$$

Here, we have rewritten $\Delta\phi$ as a function of the shift frequency ω_s, and fixed ω_c to be the center frequency of the absorption line.

This dependence is numerically calculated and plotted as a function of the ratio between AOM frequency shift and the transition linewidth (2.23 GHz) in Fig. 5.8A. To verify this dependence, we reduce the AOM frequency shift to 40 MHz and record a phase signal, measuring its amplitude as 20 mrad. This is plotted in Figure 5.7 below:

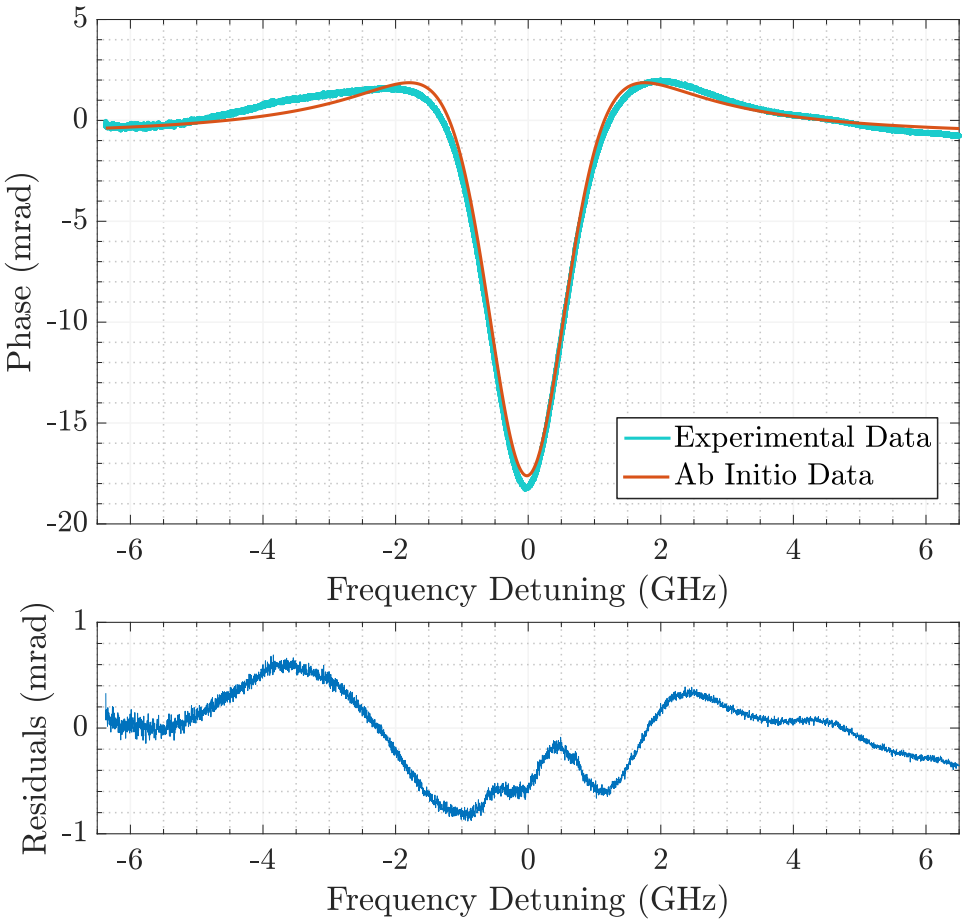

Figure 5.7: A plot of the phase signal recorded with a 40 MHz AOM frequency shift is shown. The peak to peak phase deviation is 20 milliradians, as opposed to 60 milliradians for the 120 MHz AOM frequency shift, shown in Figure 5.4.

With the amplitude of the phase signals measured using 40 and 120 MHz frequency shifts, the two frequency shift, amplitude pairs are plotted in Figure 5.8A on top of the signal magnitude model given by Equation 5.25:

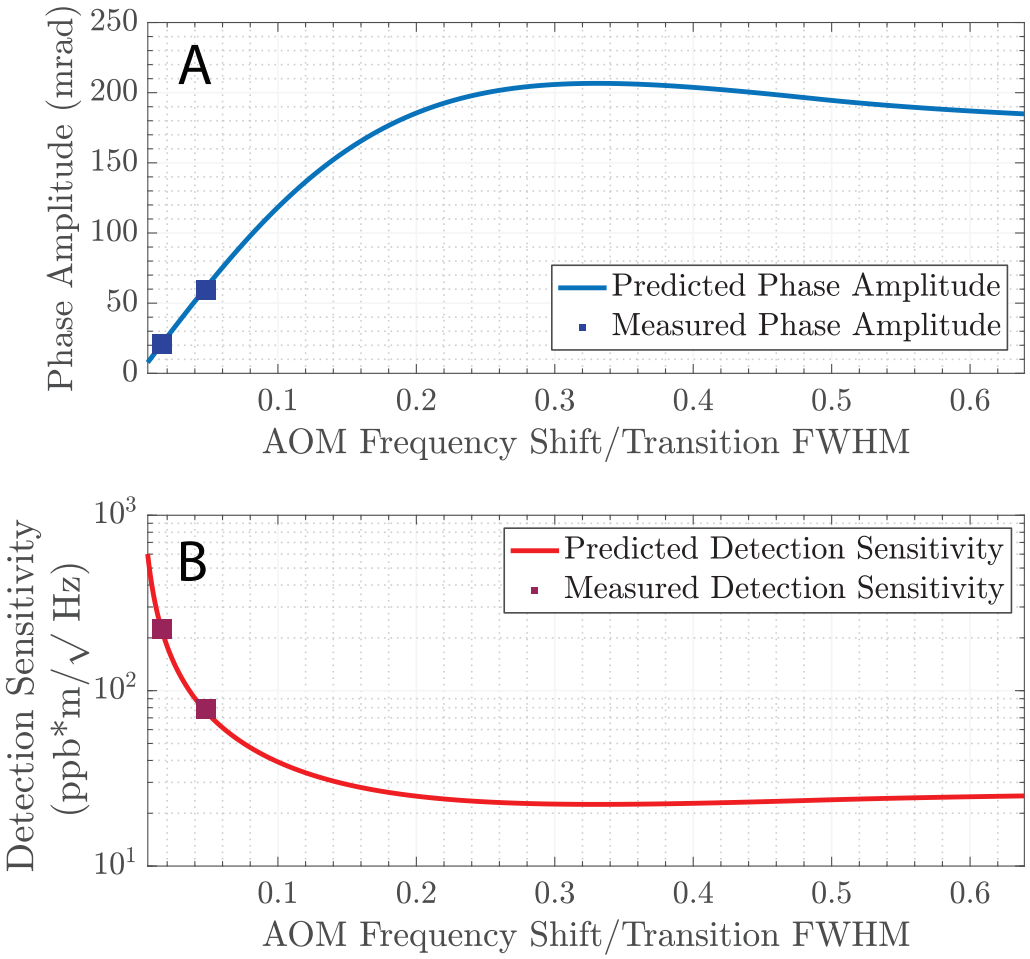

Figure 5.8: The predicted peak to peak amplitude of the the phase signal as a function of AOM frequency shift is plotted in Figure 5.8a. This curve is derived from Equation 5.25. The corresponding predicted detection sensitivity curve calibrated from the phase sensitivity is also plotted in Figure 5.8b. The measured phase amplitudes and detection sensitivities for 40 and 120 MHz frequency shifts are overlaid in their respective subplots.

We can determine the maximum possible concentration sensitivity given an optimal AOM frequency shift. In Fig. 5.8B, the phase sensitivity of the system as shown in Fig. 5.5 is used to calibrate the phase amplitude axis to units of detection sensitivity where the corresponding detection sensitivities for the 40 and 120 MHz frequency shifts are also plotted. This was done using the calibration factor of 91 ppm per mrad calculated in the previous section of this chapter. From this, we can predict that with an optimal AOM frequency shift of around thirty percent of the transition FWHM, a detection limit of 22.5 ppb $\times$ m/$\sqrt{\text{Hz}}$ can be achieved with our current optical phase sensitivity.

5.8 Conclusion

In this chapter, a noise immune digitally enhanced dispersion spectroscopy technique has been presented and experimentally validated using a HCN sample. By measuring dispersion induced phase shifts instead of absorption, dispersion spectroscopy can provide a sensitive calibrated measurement with a linear dependence on sample concentration. The dispersion induced phase shift is measured interferometrically in a Sagnac configuration with a frequency shifting AOM such that an HCN vapor cell is interrogated with two frequencies. However, because both paths around Sagnac interferometer are frequency shifted, this results in a relative phase shift at baseband between two common paths that interfere on a balanced photodetector. This combination of balanced path lengths and balanced detection yields a frequency and intensity noise immune interferometric readout with $0.8\mu\text{rad}/\sqrt{\text{Hz}}$ phase sensitivity.

Extraction of the baseband phase signal is performed using Digitally Enhanced Homodyne Interferometry. This method offloads the optical complexity required for phase extraction onto digital signal processing on a FPGA, and also suppresses etalon and backscattering effects in the interferometer. The obtained phase signal compares favorably to a theoretical phase signal computed using a analytical model under experimental temperature and pressure conditions, indicating that the phase readout can be used to extract key spectroscopic parameters. By tuning off transition, a noise analysis of the system is conducted to yield a noise equivalent detection limit of 77 $\text{ppb} \times \text{m}/\sqrt{\text{Hz}}$. With an optimized AOM frequency shift of 330 MHz, we further project a detection limit down to 22.5 $\text{ppb} \times \text{m}/\sqrt{\text{Hz}}$.

6

Molecular Dispersion Spectroscopy with Code Division Multiplexing

This chapter is based on work published in *Physical Review Applied* titled "Molecular Dispersion Spectroscopy Using a Code-Division-Multiplexed Optical Carrier" [91].

6.1 Introduction

In the previous chapter, we introduced a Sagnac-dispersion spectrometer which utilizes a balanced homodyne detection scheme within a common-path interferometer. This architecture inherently suppresses laser frequency and intensity noise, achieving a phase sensitivity of 0.8 µrad /Hz with a free-running diode laser. By interrogating dispersion-induced phase shifts with differential measurements, this method offers robust noise immunity and a detection limit of 22.5 ppb $\times$ m/$\sqrt{\text{Hz}}$ given an optimal optical frequency shift.

Although the Sagnac architecture confers first order frequency noise immunity, the topology is not as flexible as a standard Mach Zehnder interferometer. This is due to the integration of the vapor cell into the Sagnac loop, requiring bidirectional coupling of light through the analyte. The Sagnac configuration is also a double edged sword where the balanced path lengths provide stability, but do not allow for a simultaneously interferometric measurement of the laser frequency.

In contrast, the re-entrant dispersion spectroscopy technique employs a code-division multiplexed optical carrier in a single optical path. This approach also uses pseudo-random noise (PRN) modulation to synthesize interferometric measurements, allowing for multiplexing as well as noise suppression through digital signal processing. Despite requiring a slightly more complex electronic framework, it offers increased flexibility in sample interrogation and adaptability to various configurations, such as reflection-based measurements.

In this implementation of digital interferometry, the deterministic properties of the pseudo-random modulation allow us to synthesize complex interferometric measurements on simple optical hardware, using code correlation properties to distinguish different optical paths. Our previous implementations of this technique in the Sagnac configuration discussed in the previous chapter, relied on the common-path interferometer to achieve noise immunity, and thus required the sample-under-test to be integrated tightly within the measurement optics [82]. Digital interferometry was used in that application to reject

spurious non-common scattering paths within a common path Sagnac loop. Here, we differ by utilizing Digital Interferometry to independently recover measurements from multiple transits of a re-entrant optical delay-line, inherently an uncommon path length interferometer. With this simplified optical setup, we retain the ability to suppress both laser frequency noise and delay-line path length noise, which appear as common noise sources in successive round-trips of the delay-line, in effect re-synthesizing a common path interferometer with a phase noise floor of 8 µrad /Hz . Furthermore, this allows precise interferometric measurements using a single optical path, which adds the flexibility to interrogate the measurement sample either in transmission or reflection and obviates the need for a separate optical reference or local oscillator.

In this manner, we experimentally demonstrate molecular dispersion spectroscopy via a single optical path transmitted through a gas cell and achieve a molecular detection sensitivity of 159 ppb × m/$\sqrt{\text{Hz}}$, which is within a factor of two of our noise-immune Sagnac interferometer architecture [82]. Having decoupled the sideband generation and demodulation from the gas sensing optics, this optical topology can achieve a higher degree of flexibility, and enable the optics for the sample-under-test to be independently modified to fit design requirements of target applications.

6.2 Code Division Multiplexed Re-entrant Interferometer

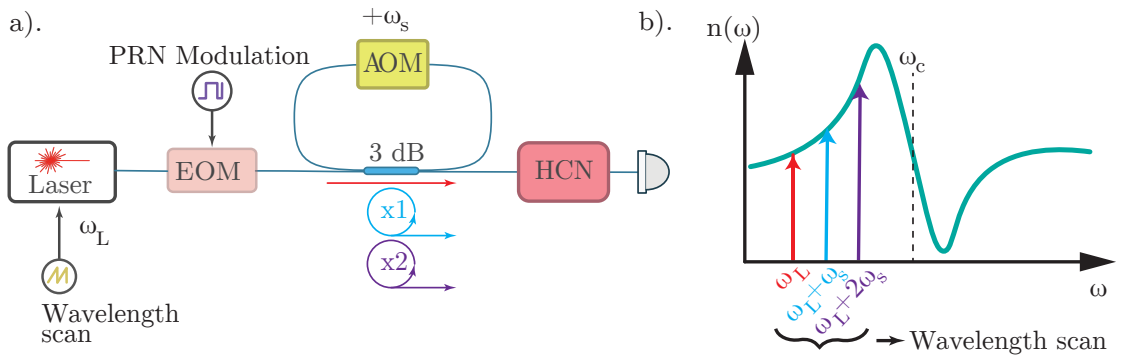

Figure 6.1: In a), we present a conceptual diagram demonstrating the basic optical architecture of our spectrometer. An optical source, with frequency ω_l with linewidth much narrower than a $H^{13}C^{14}N$ molecular transition is split by a 3 dB coupler and seeded into a frequency shifting re-entrant delay line loop. An acousto-optic modulator (AOM) with frequency shift ω_s is used to provide this frequency shift. There is prompt transmission through the coupler bypassing the loop. This field will have the unshifted frequency ω_l. Successive passes through the loop will be frequency shifted to $\omega_l + q\omega_s$, where q is the number of loop transits. The three fields illustrated exit the re-entrant loop and enter a vapor cell containing hydrogen cyanide ($H^{13}C^{14}N$), where they experience differential phase shifts corresponding to the anomalous dispersion around an $H^{13}C^{14}N$ transition, as shown in b).

The foundational technique used in this architecture is Digitally Enhanced Heterodyne Interferometry (DeHeI) which has been used extensively in many other ranging, and multiplexing interferometric applications [35, 92]. This is the base form of Digital Interferometry we described in Chapter 3, which we briefly review here. In this application of DI, as per the conceptual diagram shown in Figure 6.1a, a laser of frequency ω_L is phase modulated with a DeHeI binary pseudo-random noise (PRN) sequence by an electro-optic

modulator (EOM) at a modulation depth of π radians. The resultant phase modulation has the effect of pseudo-randomly inverting and thus scrambling the optical phase. After propagating through an optical system, the modulated optical signal is correlated with a delayed local copy of the pseudo-random sequence. By choosing a delay equal to the transit time of the optical system, DeHeI uses the correlation of the code to recover the signal of interest. Other signals with different delays will be strongly suppressed by the auto-correlation of the PRN sequence, effectively creating a range gate. This allows for multiple optical signals to be multiplexed within a single interferometer, differentiated by their code time-of-flight.

In this architecture, the modulated DeHeI field is seeded into a re-entrant delay-line loop using a 3 dB coupler, as seen in Figure 6.1a. An acousto-optic modulator (AOM) is placed within the loop such that successive passes of the delay-line are frequency shifted by integer multiples of the AOM frequency ω_s. In addition, each successive pass around the loop delays the pseudo-random sequence by the transit time of the loop allowing pseudo-random code separability of each frequency term. Note, there will also be an unshifted zero-pass field that bypasses the delay-line altogether. In this analysis, we will only consider the zero (ω_l), first ($\omega_l + \omega_s$), and second passes ($\omega_l + 2\omega_s$) of the delay-line. This restriction is reasonable as the cumulative losses through the AOM and lack of amplification within the delay-line mean that subsequent transits contribute negligible optical power to the final readout.

Following the re-entrant delay-line, the three fields we consider enter an $H^{13}C^{14}N$ vapor cell, where they experience different phase shifts corresponding to the anomalous dispersion around an $H^{13}C^{14}N$ molecular transition. This is depicted in Figure 6.1b. Thus when the three fields are incident on the photodetector, the differential dispersion between the three fields will be carried on the phase of the heterodyne beatnotes at ω_s and $2\omega_s$. As the laser frequency ω_l is tuned across the transition, which can be achieved using thermal tuning of the laser, we can write the frequency dependent phase shifts experienced by each of the fields as per Equations 6.1-6.3:

$$\begin{aligned}\phi_0 = &\frac{\omega_l n(\omega_l) L_{\text{cell}}}{c} + \phi_{\text{laser}}(t-\tau_0) \\ &+ m(t-\tau_0),\end{aligned} \tag{6.1}$$

$$\begin{aligned}\phi_1 = &\left[\frac{(\omega_l+\omega_s) n(\omega_l+\omega_s) L_{\text{cell}}}{c} + \phi_{\text{laser}}(t-\tau_1)\right] \\ &+ m(t-\tau_1),\end{aligned} \tag{6.2}$$

$$\begin{aligned}\phi_2 = &\left[\frac{(\omega_l+2\omega_s) n(\omega_l+2\omega_s) L_{\text{cell}}}{c} + 2\phi_{\text{laser}}(t-\tau_1)\right] \\ &+ m(t-2\tau_2),\end{aligned} \tag{6.3}$$

$$m(t) \in [0, \pi],$$

where ϕ_{laser} is the differential path length phase noise induced by the laser frequency noise, ω_l is the center frequency of the laser, ω_s is the frequency shift induced by the AOM, $n(\omega)$ is the frequency dependent refractive index of the $H^{13}C^{14}N$ sample, and L_{cell}

is the length of the vapor cell. We write the DI phase modulation as $m(t)$, which pseudo-randomly toggles between 0 and π and is time shifted corresponding to the delays τ_0, τ_1, τ_2 experienced by the three optical fields respectively. We also note that the phase noise scales as the integer multiple of the loop passes, hence the factor of 2 in front of the phase noise term in Equation 6.3. At the photodetector, the three fields, with their respective phase shifts can be written as per Equations. 6.4-6.6:

$$E_0 = \frac{E}{2}\alpha(\omega_l)\exp\left[i\omega_l t + i\phi_0\right] \times P(t-\tau_0), \tag{6.4}$$

$$E_1 = \frac{E}{4}\alpha(\omega_l+\omega_s)\exp\left[i(\omega_l+\omega_s)t + i\phi_1\right] \times P(t-\tau_1), \tag{6.5}$$

$$E_2 = \frac{E}{8}\alpha(\omega_l+2\omega_s)\exp\left[i(\omega_l+2\omega_s)t + i\phi_2\right] \times P(t-\tau_2), \tag{6.6}$$

$$P(t) \in [1,-1],$$

where $\alpha(\omega)$ is the frequency dependent absorption coefficient. The DeHeI phase modulation term $m(t)$ in Equations 6.1-6.3 is mathematically equivalent to multiplying the field by 1 or -1. Thus, we factor the DeHeI modulation out of the phase term and rewrite the modulation as a bipolar sequence: $P(t)$. The sum of these fields incident on a square law photodetector results in a signal with 6 terms: three DC terms, two terms with heterodyne frequency equal to the AOM frequency: ω_s, and one term with a heterodyne frequency double the AOM frequency: $2\omega_s$. We first write the three DC terms, I_{DC}, in compact form:

$$\sum_{n=0}^{2} E_i^2 P^2(t-\tau_i), \tag{6.7}$$

The two interference terms between E_0 and E_1, and E_1 and E_2 are written respectively as $I_{\omega,1}$ and $I_{\omega,2}$:

$$I_{\omega,1} \propto \frac{E^2}{4}\alpha(\omega)\alpha(\omega_l+\omega_s)\cos(\omega_s t+\phi_1-\phi_0) \times P(t-\tau_0)P(t-\tau_1), \tag{6.8}$$

$$I_{\omega,2} \propto \frac{E^2}{16}\alpha(\omega_l+\omega_s)\alpha(\omega_l+2\omega_s)\cos(\omega_s t+\phi_2-\phi_1) \times P(t-\tau_1)P(t-\tau_2), \tag{6.9}$$

and finally, the $I_{2\omega}$ term:

$$I_{2\omega} \propto \frac{E^2}{8}\alpha(\omega_l)\alpha(\omega_l+2\omega_s)\cos(2\omega_s t+\phi_2-\phi_0) \times P(t-\tau_0)P(t-\tau_2) \tag{6.10}$$

For the spectroscopic readout described here, we isolate the two interference terms (Equations. 6.8-6.9). Since these two terms have the same heterodyne frequency, conventionally, it would not be possible to separately extract the phase carried on each of these heterodyne terms. However, since they have been tagged with DeHeI phase modulation, by correlating with the appropriately delayed code pairs: $P(t-\tau_0)P(t-\tau_1)$ and $P(t-\tau_1)P(t-\tau_2)$, we can isolate these terms in two separate channels.

We then proceed with the standard method of IQ demodulation in heterodyne interferometry as described in Chapter 3, demodulating Equations 6.8-6.9 by mixing down the photodetector voltage signal with a local oscillator phase locked to the AOM frequency ω_s, low pass filtering, and then calculating the arctangent to recover the phase angle.

We thus extract the differential phases $\Phi_1 = \phi_1 - \phi_0$ and $\Phi_2 = \phi_2 - \phi_1$, noting that these phases will still include the laser phase noise term ϕ_{laser}. However, by taking the difference between these two expressions, we can form the combination ϕ_{sig} that allows the cancellation of the common laser phase noise, leaving only laser phase noise $\phi_{\text{laser}}(t-\tau_0)$ carried on the unshifted pass:

$$\begin{aligned}\phi_{\text{sig}} &= (\phi_2 - \phi_1) - (\phi_1 - \phi_0) \\ &= \frac{L_{\text{cell}}}{c}[(\omega_l + 2\omega_s)n(\omega_l + 2\omega_s) - 2(\omega_l + \omega_s)n(\omega_l + \omega_s) \\ &\quad + \omega_l n(\omega_l) + \phi_{\text{laser}}(t-\tau_0)] \\ &\approx \frac{\omega_l L_{\text{cell}}}{c}[n(\omega_l + 2\omega_s) - 2n(\omega_l + \omega_s) + n(\omega_l)] + \phi_{\text{laser}}(t-\tau_0)\end{aligned} \tag{6.11}$$

Noting that the AOM frequency shift of 200 MHz is six orders of magnitude smaller than the optical frequency of the laser (193 THz) $\omega_s \ll \omega_l$, we have simplified and collected the ω_l frequency term. The form of this expression is equivalent to the definition of the second derivative of the refractive index. Intuitively, we can infer this as ϕ_{sig} is formed by taking the difference between two phase differences.

The uncancelled residual phase noise term $\phi_{\text{laser}}(t-\tau_0)$ depends on the intrinsic laser phase noise. This can be minimized by using single-frequency fiber lasers, which have < 1 KHz/$\sqrt{\text{Hz}}$ frequency noise at spectroscopic signal detection bandwidths of 10-100 Hz [93]. Inserting a typical frequency noise trace for one of these lasers into the frequency noise calculation shown in Chapter 3, we arrive at a phase noise of just under 2 μrad/$\sqrt{\text{Hz}}$ for a 1 meter armlength difference at 10 Hz, falling to 0.4 μrad/$\sqrt{\text{Hz}}$ per meter at 100 Hz. Thus, by using a single frequency fiber laser, and shortening fiber pigtails such that the zero pass path length is under 1 m, the laser phase noise contribution can be minimized such that this technique retains sub-microradian phase sensitivity.

6.3 Experimental Implementation

The experimental demonstration, shown in Figure 6.2, uses a Koheras X15 fiber laser with 100 Hz linewidth. To interrogate the full width of the dispersion profile, the laser frequency is thermally tuned using the X15 control software. The laser output is phase modulated with a binary pseudo-random noise modulation (PRN) using an iXBlue MPX-LN0.1 electro-optic modulator (EOM). The PRN modulation generates an optical spread-

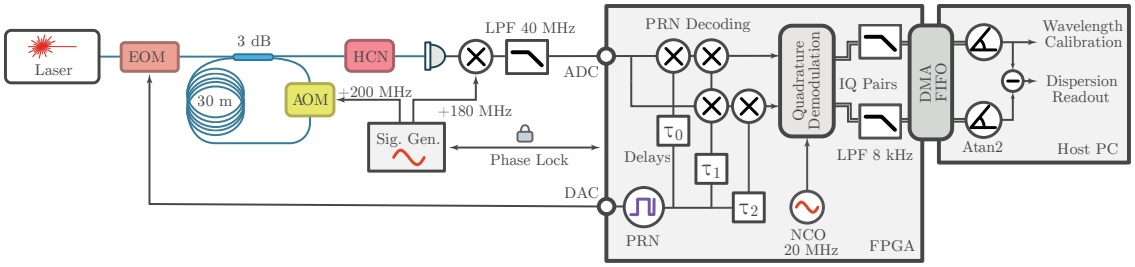

Figure 6.2: The output of a 1550 nm fiber laser is phase modulated by an EOM to encode a PRN sequence. This is seeded into a re-entrant frequency shifting loop consisting of a 30 m long fiber coil and a 200 MHz AOM. There is a prompt path through the loop coupler bypassing the loop that does not experience a frequency shift, a single pass around the loop that experiences a 200 MHz shift, as well as a double pass that experiences a 400 MHz shift. The three fields experience differential phase shifts as they interrogate the dispersion profile of an $H^{13}C^{14}N$ vapor cell, and a photodetector records the resulting interference. To scan the dispersion profile, the laser wavelength is swept across the $H^{13}C^{14}N$ transition by thermal tuning.

spectrum, centered around the laser frequency, with characteristic nulls at the PRN symbol (chip) frequency of 16 MHz.

The spread-spectrum optical field is coupled into a fiber re-entrant delay-line using a 3 dB coupler. The delay-line consists of a 30 m potted fiber coil and a fiber coupled, Gooch & Housego FiberQ AOM. This is used to frequency shift successive round-trips of the re-entrant delay-line by the AOM drive frequency of 200 MHz. The output of the re-entrant delay line is connected to a fiber coupled vapor cell containing pure $H^{13}C^{14}N$ gas manufactured by Wavelength References (Model Number: HCN-13-C-10). The cell has a pressure of 10 Torr at room temperature, and a path length of 16.5 cm. After interacting with the vapor cell, the resulting interference signal is incident on a fiber coupled New Focus 1611 photodetector with 1 GHz bandwidth.

Digital Signal processing for the system is handled using a National Instruments platform consisting of a Virtex-5 field programmable gate array (FPGA) coupled with an NI5781 transceiver module, consisting of two differential output digital-to-analog converters (DACs) at 100 MS/s and two differential input analog-to-digital converters (ADCs) at 100 MS/s. The analog front-end of the ADCs additionally has a 7th order elliptical low-pass anti-aliasing filter with a 3 dB corner frequency at 40 MHz.

The FPGA system is firstly used for the generation of the PRN modulation. This is output from the DAC at the 16 MHz symbol frequency to drive the EOM. The modulation is also digitally delayed internally on-FPGA and used for demodulation of the three optical delays from the system. These delays correspond to the prompt (τ_0), first (τ_1), and second (τ_2) round trip through the re-entrant delay line.

The AOM is driven at 200 MHz using a Liquid Instruments Moku:Pro signal generator which is phase locked to the National Instruments FPGA system. The frequency offset from the AOM center frequency (200 MHz) is to tune the DEHeI heterodyne frequency for optimal cross-talk rejection [94].

The voltage signal from the New Focus 1611 photodetector is first mixed down by a 180 MHz tone phase locked to the 200 MHz tone used to drive the AOM. The downmixing is

performed with a Minicircuits ZP-3MH+ mixer in order to meet the 40 MHz bandwidth requirement of the ADC on the FPGA. We choose a local-oscillator frequency of 180 MHz, which is mixed with the heterodyne beat note at 200 MHz, thus placing the 20 MHz mixed down output squarely in the middle of the ADC bandwidth. The resulting 20 MHz intermediate-frequency is digitized by the ADC on the FPGA and then correlated with the appropriately delayed codes.

Following code correlation, the two demultiplexed channels corresponding to Equations 6.8 and 6.9 are mixed with a numerically controlled oscillator (NCO) at 20 MHz and low pass filtered to recover the in-phase and quadrature projections relative to the NCO. These two IQ pairs are low pass filtered and decimated to 8 KHz to remove high frequency upshifted components and then streamed onto a host PC, where an arctangent is performed to recover the phases of the two channels. Finally, the recovered differential phases are subtracted to obtain the double derivative spectroscopic readout.

6.4 Self-calibration & Sensitivity

The individual phases of the two measurement channels can be used to perform a calibration of the wavelength scan. As the laser is thermally tuned across the transition, the re-entrant delay line causes each channel to accumulate a phase shift at a rate proportional to the rate of frequency tuning. Since 2π radians of phase corresponds to one free spectral range (FSR) of the re-entrant delay line, by measuring the FSR, we can calibrate the accumulated phase to laser frequency detuning relative to the absorption line. The calibration curve is then used to re-parameterize the time axis into units of frequency, thus removing the tuning nonlinearity from our measurement. Here, we give the equation used for this calibration:

$$f_{\mathrm{cal}}(t)[\mathrm{Hz}] = \frac{\phi_{\mathrm{sig}}(t)}{2\pi} \times \frac{c}{nL} \tag{6.12}$$

The first term converts the phase accrued over one pass of the re-entrant loop into cycles. The second term is the FSR of the re-entrant loop in units of frequency. This is equivalent to $1/\tau$, where τ is the loop transit time. Thus, the product yields the frequency of the laser as function of time f(t). By inverting the function $f_{\mathrm{cal}}^{-1}(t) = t(f)$, the timebase of a spectroscopic measurement can be converted to frequency units. In our spectroscopic measurement, the laser is freely thermally tuned over > 9 GHz in order to capture the wings of a 1 GHz FWHM absorption line. This calibration method allows us to compensate for any nonlinearity in the thermal tuning that would otherwise distort the lineshape of the spectroscopic measurement.

We have performed this calibration procedure on the absorption profile of the $H^{13}C^{14}N$ transition, calibrating a time domain trace of the absorption line into frequency. To begin, we plot the raw demodulated readout for the two channels $I_{\omega,1}$ and $I_{\omega,2}$, in Figure 6.3. This is composed of two measurements. The first is amplitude (absorption) in Figure 6.3A, which is the quadrature sum of in-phase and quadrature components. The second, shown in Figure 6.3B is the two-argument arctangent phase:

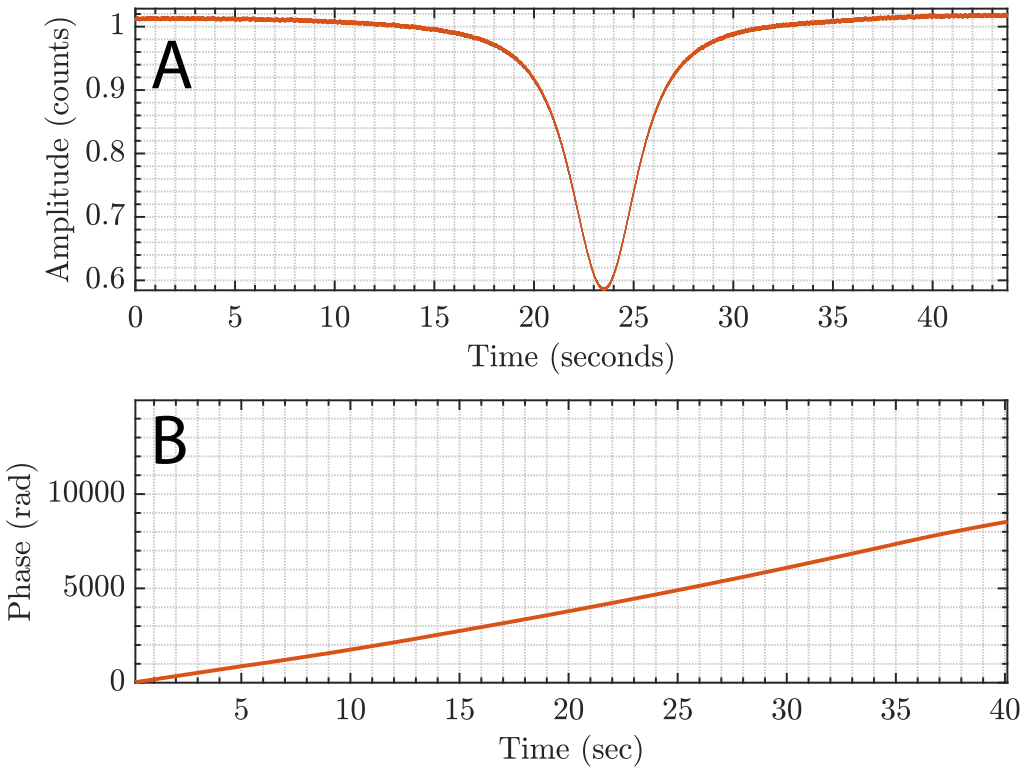

Figure 6.3: The top panel shows the amplitude response of the $I_{\omega,1}$ and $I_{\omega,2}$ terms as the laser is freely thermally tuned over the transition. The two traces are overlaid as to be indistinguishable, as they separated only by the optical transit time of the 30 meter coil. The bottom panel shows the phase excursion (Φ_1 and Φ_2) corresponding to the amplitude traces (also overlaid as to be indistinguishable). In the phase readout, there is a slight concave nonlinearity visible, due to laser tuning. This is what we aim to calibrate out.

From the raw phase readout in Figure 6.3B, we use Equation 6.12 to convert the phase into a frequency deviation. Since the center frequency of the P10 absorption line is known a priori, we are free to center the absorption peak around zero detuning. We have plotted this frequency calibration in Figure 6.4B below:

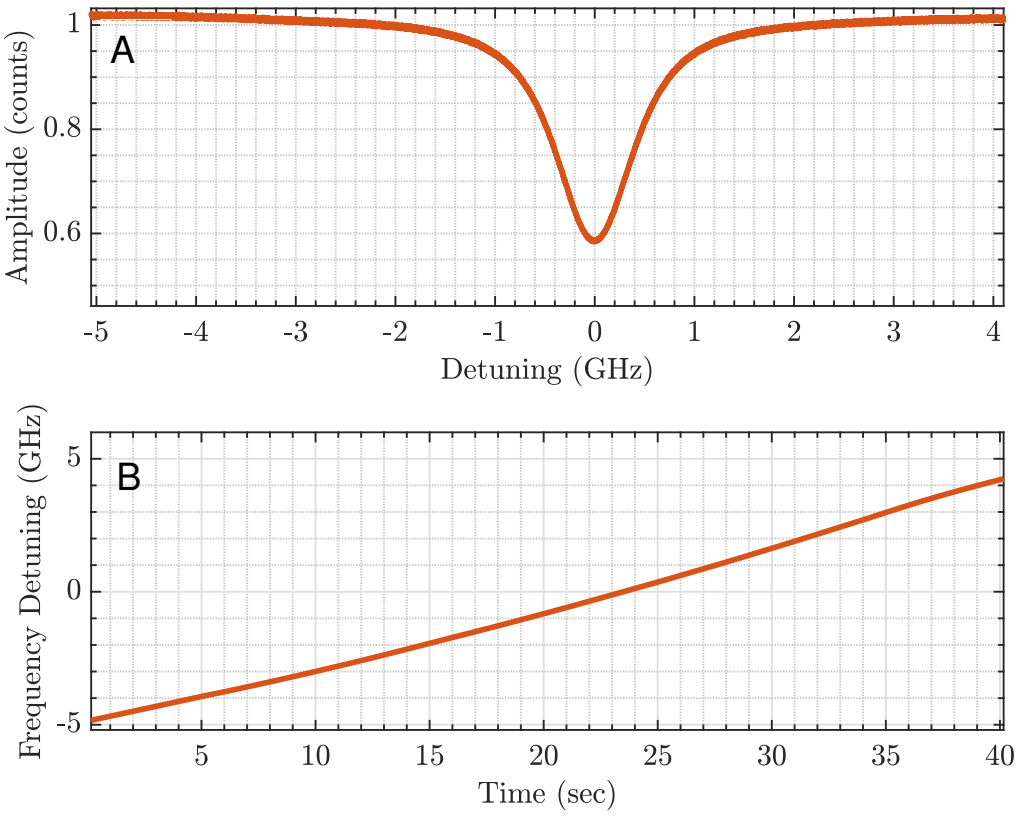

Figure 6.4: The curve in B shows the frequency calibration of the raw phase readout plotted in Figure 6.3B. In A, this frequency calibration is used to remap the measured absorption from time to frequency. The frequency plotted in the x-axis in A. therefore corresponds with the y-axis in B. Crucially, the slight concave nonlinearity visible in the laser tuning frequency has now been calibrated for in the absorption readout.

The relationship between frequency and time in Figure 6.4B now allows us to remap the time axis of the absorption line in Figure 6.3A to frequency, yielding Figure 6.4A. For the sake of clarity, this calibration process was illustrated for absorption, as the absorption signal is large compared to the double derivative dispersion signal. However, once the time to frequency calibration trace is obtained, the dispersion signal can be calibrated using the same procedure.

6.5 Phase Sensitivity

To determine the sensitivity of the spectroscopic phase measurement, a ten minute off resonance measurement is taken where the laser is thermally tuned away from the transition, measuring solely the intrinsic noise of the phase measurement. From this, we compute the noise floor as determined by the off resonance phase spectral density of the two channels, and their subtraction which forms the spectroscopic readout. The two individual channels as well as their subtraction (Equation 6.11) are shown in Figure 6.5. The subtracted readout shows a minimum noise floor of 8 $\mu\text{rad}/\sqrt{\text{Hz}}$, along with a shelf below 10 Hz, while the phase noise of the individual channels display a 1/f rollup below 10 Hz. At 10 mHz, this results in 5 orders of magnitude of suppression in phase noise, indicating that

the subtraction strongly suppresses laser phase noise, which is correlated between the two channels.

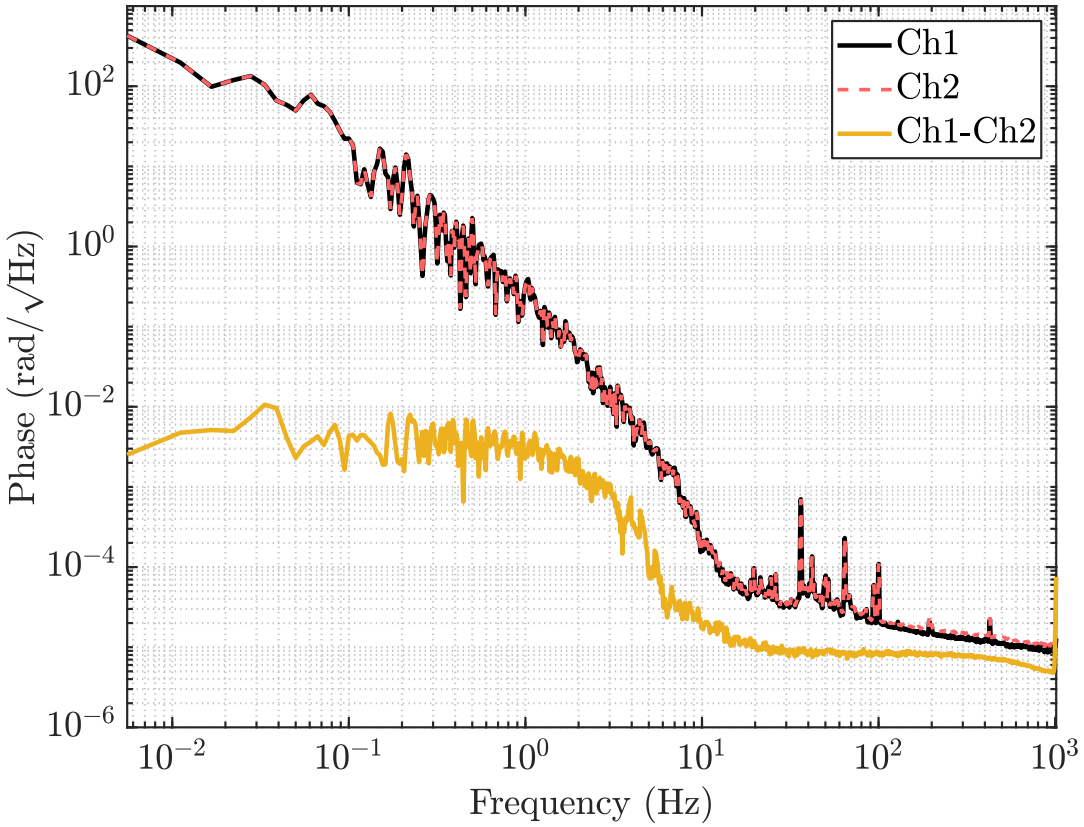

Figure 6.5: The phase readouts from the two individual channels, and their subtraction are plotted. The subtraction, which forms the spectroscopic readout demonstrates strong suppression of up to five orders of magnitude for 1/f phase noise below 10 Hz. The low frequency noise shelf in the subtracted measurement is due to code noise [44].

The noise shelf is caused by digital interferometric code noise, as seen in previous implementations of re-entrant delay lines [44]. Code noise is the result of residual crosstalk between the pseudo-random codes modulated onto each pass of the re-entrant delay line. This can be addressed in future implementations using two strategies. Previous work on DI has demonstrated code noise suppression using an additional laser frequency ramp with modulation depth equal to the delay line free spectral range. This has the effect of ramping the code noise to beyond the measurement bandwidth [44]. Alternatively, zero-crosstalk DI modulation codes [95] have been identified as a potential solution. This will be discussed further in the next Chapter.

6.6 Spectroscopic Measurement

To validate the measurement scheme, we perform a spectroscopic measurement of the P10 line in the $2\nu_3$ rotational-vibration band of $H^{13}C^{14}N$, a common wavelength reference for 1550 nm. Instead of P11 used in the previous chapter, this particular line was chosen as the fiber laser we used was factory calibrated against it. The measured spectroscopic signal is shown in Figure 6.6a. This is taken by subtracting the two phase traces displayed in 6.4B, and remapping the time axis to frequency using the calibration method outlined

above. Since the phase signal is roughly a tenth of a radian, it is not visible in the raw phase readout, but only when the two channels are subtracted, removing phase ramp driven by frequency tuning. Indeed, we can think of this subtraction as suppressing very low frequency (sub Hz) noise. This suppression was shown in Figure 6.5 to be greater than 5 orders of magnitude at 0.01 Hz, on the same order as the 40 second laser tuning window.

The 16.5 cm gas cell used for the measurement contains pure $H^{13}C^{14}N$ gas at a calibrated pressure of 10 Torr and was interrogated by freely thermally tuning the X15 laser over the transition. With these vapor cell parameters, the peak absorption fraction of the P10 transition in the vapor cell was calculated to be 0.7 using data from the GEISA2003 spectroscopic database [96]. The double-differential readout was calibrated from time to relative optical frequency using a single round trip measurement to remove non-linearities in the thermal tuning rate, as described in the previous section. In order to aid fitting, the resulting calibrated double differential readout was then low-pass filtered from a readout rate of 7.8 KHz to 10 Hz to remove high frequency technical noise from the measurement.

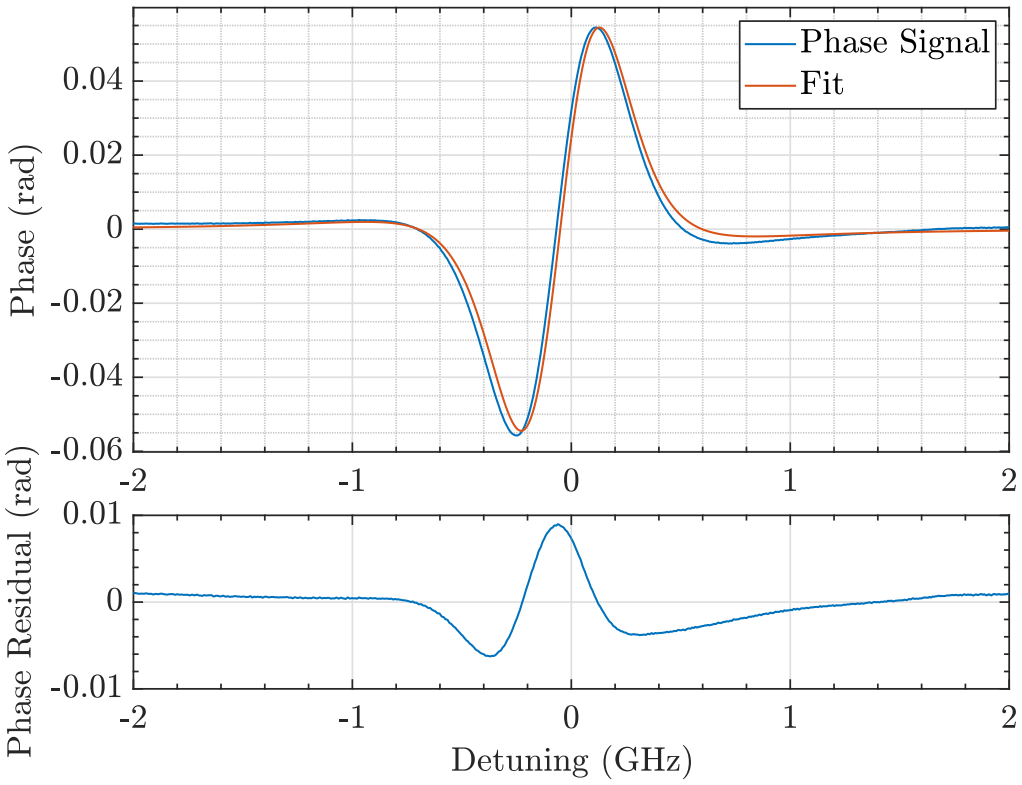

Figure 6.6: The experimental phase signal, and the theoretical phase signal generated from the model using experimental pressure and temperature conditions are plotted in the top panel of Figure 6.6. The x-axis is shifted such that the phase signal is centered at the linecenter of the P10 transition. In the bottom panel we plot the residuals between the measurement and fit.

Using the known pressure, temperature, and concentration of the cell, we compute a theoretical Voigt lineshape with a linecenter defined at zero detuning. We then compute the dispersion by performing a numerical Hilbert transform [63], using the method outlined in chapter 2, yielding a refractive index curve $n(\omega)$. This refractive index curve is then

entered into the Equation 6.11 as the fitting function, where L_{cell}, and ω_s are known parameters.

With the model parameters fully defined we plot the expected double-differential readout, which is then overlaid on the experimental data in Figure 6.6a. The modeled signal shows good agreement with the experimentally obtained signal, with the residuals plotted in Figure 6.6b. We also note that the slope of the residual is small compared to the the Sagnac dispersion phase signal in Figure 5.7b. This demonstrates that the self-calibration has removed the effect of laser tuning nonlinearity on the phase signal. The remaining residual is then dominated by a fitting error, which arises from the Hilbert Transform generation of the fit function, as described in Section 2.3.2. Since the Hilbert Transform operates over the whole real domain, we suspect that the fit error can be minimized through smooth zero-padding of the transmission spectrum used to compute the fit function.

To determine the concentration sensitivity of this technique, we refer back to the phase noise spectral density shown in Figure 6.5, where the phase sensitivity above 30 Hz was measured to be 8 µrad/$\sqrt{\text{Hz}}$. This phase sensitivity can be calibrated to concentration in units of parts per billion meters (ppb×m) by noting that the peak phase excursion of 110 mrad measured in Figure 6.6 occurs at a vapor cell concentration of 2185 ppm-meter, as calculated using Equation 2.12 derived in Chapter 2. We note that this is a lower concentration than for the Sagnac spectrometer, which used a 25 Torr cell, as here we use a 10 Torr vapor cell of the same physical dimensions (Wavelength References 16.5 cm cell).

Dividing the concentration by the phase amplitude sets a calibration factor of 19.9 ppm-meter per mrad. Since the spectroscopic phase signal scales linearly with concentration, we can readily convert our phase noise spectral density by this calibration to give a concentration sensitivity in units of ppb × m/$\sqrt{\text{Hz}}$. In performing this calibration, we arrive at a noise equivalent detection limit of 159 ppb × m/$\sqrt{\text{Hz}}$, which exceeds FM and WM spectroscopy sensitivity in the near infrared with single pass gas cells by a factor of 3 [97], and is comparable to the concentration sensitivity achieved by CLaDS and HPSDS [86]. This is equivalent to a fractional absorption absorption sensitivity of $4.9 \times 10^{-5}/\sqrt{\text{Hz}}$.

The detection limit is a factor of two less sensitive to that achieved by our previous work in dispersion spectroscopy using a Sagnac interferometer. We sacrifice the inherent stability of the Sagnac interferometer, in return gaining access to a measurement of relative laser frequency that can be used for real-time calibration. The method described in this chapter also affords greater flexibility in that the spectroscopic sample is placed uni-directionally, in line with the fiber delay loop, instead of embedded within a bidirectional Sagnac loop. As such, this single pass approach allows easier alignment for spectroscopic measurements using free space cells. We also highlight the ability (with the addition of a circulator) to obtain a dispersion signal in reflection in addition to transmission. With this slight modification in the setup layout, this architecture can thus be used as an optical network analyzer to characterize a wide array of photonic components such as Fiber Bragg gratings, filters, and dichroic mirrors. In the final chapter, we will also discuss potential applications to using this setup to interrogate metasurfaces, which operate both under reflection and transmission.

6.7 Conclusion

In this chapter, we have presented and experimentally verified an alternative molecular dispersion spectroscopy technique that retains the sub microradian phase sensitivity and sub parts per million concentration detection limit of Sagnac dispersion spectroscopy.

In the Sagnac interferometer, homodyne digital interferometry was used as a phase sensing technique with enhanced noise rejection properties. In this implementation, digital interferometry is used to track and demodulate multiple passes of optical fields traveling in a re-entrant delay line in order to synthesize a common path interferometer. The resulting spectroscopic signal is proportional to the second derivative of the refractive index, as opposed to the first derivative for Sagnac dispersion spectroscopy. Taking this into account in the fitting routine, we demonstrate good agreement between experimental measurements and a theoretical phase signal computed using a analytical model. Utilizing the raw phase output corresponding to interference between successive delay line transits we also remove laser tuning nonlinearity. This was a systematic error source in Sagnac dispersion spectroscopy, causing a non-zero slope in the fitting residual.

By subtracting these individual wavelength tuning calibration channels, we synthesize common-mode suppression of laser and path length phase noise down to 8 µrad $/\sqrt{\text{Hz}}$. At suppression factors of up to 5-orders of magnitude, the system demonstrated a noise equivalent concentration detection limit of 159 ppb $\times$ m$/\sqrt{\text{Hz}}$. This is only a factor of 2 higher than the concentration sensitivity of the Sagnac dispersion spectrometer, which benefits from inherent common path frequency noise suppression. Given that this technique retains sub-ppm detection limit, the architecture offers a robust, optically simple, and flexible metrology scheme which can be readily adapted to the requirements of different sensing configurations.

7

Conclusion and Future Work

The research presented in this thesis has leveraged digital interferometric techniques to enhance dispersion spectroscopy. Digital interferometry, with its robust phase sensing capabilities, has been demonstrated as a highly effective tool for measuring milliradian phase signals, crucial for precise dispersion measurements.

A key milestone was the successful implementation of digital interferometry within a Sagnac interferometer, which provided an optimal testbed due to its inherently balanced arm lengths and first-order frequency noise suppression. However, the symmetry of the Sagnac interferometer made traditional interferometric phase extraction techniques difficult. Hence, we proposed digital interferometry as an alternate phase extraction technique for the Sagnac interferometer. This configuration enabled us to evaluate the fidelity of digital interferometric phase extraction. Here, digital interferometry demonstrated suppression of scattering-induced noise while maintaining high phase sensitivity, down to $2 \times 10^{-7}\,\mathrm{rad}/\sqrt{\mathrm{Hz}}$, only limited by shot noise and ADC noise. Building upon this foundation, we developed a digitally enhanced homodyne dispersion spectrometer by incorporating a vapor cell into the Sagnac loop, achieving $77\mathrm{ppb} \times \mathrm{m}/\sqrt{\mathrm{Hz}}$ concentration sensitivity through homodyne digital interferometry, and the stability of the interferometer architecture.

Expanding on these developments, we introduced a more flexible unidirectional sensing system based on a re-entrant delay line Mach-Zehnder interferometer. By tracking multiple passes through the delay line, we synthesized a balanced path-length interferometer capable of subtracting common frequency noise, leading to spectroscopic sensitivity of 159 $\mathrm{ppb} \times \mathrm{m}/\sqrt{\mathrm{Hz}}$, comparable to that of the Sagnac configuration. The delay line configuration also allowed us to obtain a real time measurement of the laser detuning with respect to the linecenter of the measured transition. By using the relative frequency measurement, we were able to calibrate for laser tuning nonlinearity, which was a source of systematic error in the Sagnac spectrometer.

The work in this thesis is to date, the first demonstration of digital interferometry for spectroscopy, paving the way for future applications of digital interferometry for phase-based spectroscopic sensing. Ongoing work on digital interferometric algorithms [95] should allow for higher fidelity phase recovery and thus lower phase noise floors, especially in differential measurements, where common mode noise rejection is critical, further enhancing the concentration sensitivity of the techniques described in this thesis. In the following section,

we focus on current and future work applying these newer DI algorithms to dispersion spectroscopy systems requiring large optical bandwidths.

7.1 Future Directions

Building on the work presented, ongoing research involves two complementary streams. The first is the development of digital interferometric techniques for dispersion sensing of wide spectral features, without needing laser tuning. The second stream explores applications of dispersion spectroscopy to metasurface sensing, which are wide in optical bandwidth compared to molecular transitions, and thus would benefit from broadband dispersion sensing.

7.1.1 Digitally Addressable Optical Frequency Comb

As an extension of re-entrant dispersion spectroscopy, we harness the multiplexing potential of digital interferometry to recover up to twenty transits through the delay line, effectively forming an acousto-optic frequency comb enhanced by Digital Heterodyne Interferometry.

The digital interferometric frequency comb attempts to address two fundamental limitations of the dispersion techniques presented in the previous chapters. The first being the requirement for the laser to tune across the transition. This was the cause of the sloped residuals in Sagnac dispersion spectroscopy introduced in chapter 4. Although calibrated out in the re-entrant dispersion spectroscopy technique, it nevertheless introduces an opto-electronic constraint to dispersion spectroscopy techniques, especially when wide and fast tuning across transition(s) is required. The digital interferometric frequency comb addresses this limitation by synthesizing a single shot measurement across the transition of interest without laser tuning. By varying the EDFA gain and changing the AOM frequency, it is possible to tailor the comb span to the linewidth of a transition of interest.

The second limitation that the digital interferometric frequency comb aims to address is the dependence of signal amplitude and thus concentration sensitivity on the acousto-optic frequency shift. In traditional dispersion spectroscopy techniques, a frequency shift on the order of half the transition linewidth is required to optimize the maximize the signal size. We demonstrated this effect in Chapter 4. For wide transitions, greater than 5 GHz, this would require shifts greater than 2 GHz. To the best of the author's knowledge there currently exist no acousto-optic modulators that meet this requirement. Using a re-entrant delay line with an line frequency shifter and EDFA allows such larger frequency shifts to be synthesized.

This work derived as a natural extension to re-entrant delay line spectroscopy, where we have added optical gain using an Erbium Doped fiber amplifier (EDFA) within the re-entrant delay line loop. This boosts the field amplitude of each pass around the loop, allowing for multiple transits of the loop (more than 3) to be simultaneously demodulated. In Figure 7.1, we show a conceptual diagram of the experimental setup:

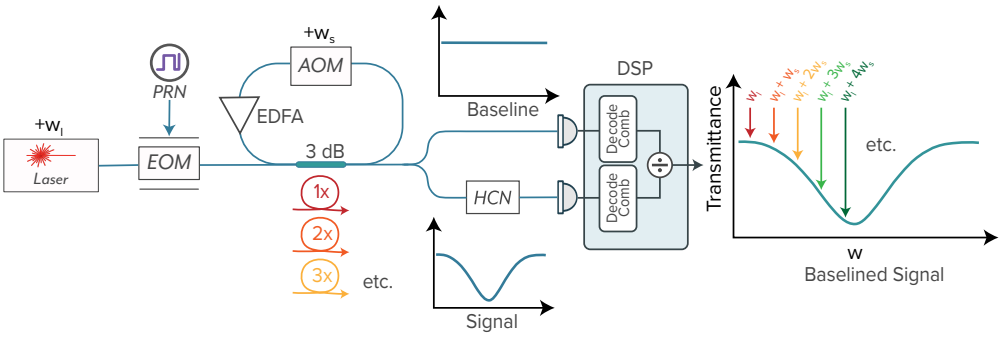

Figure 7.1: A laser of frequency ω_l is split by a 3 dB coupler into a re-entrant delay loop. The re-entrant loop contains an AOM, which induces an ω_s frequency shift, and an EDFA which compensates for power loss. Each successive pass through the loop induces a frequency shift of $\omega_l + n\omega_s$, where n is the number of transits. The output is split into signal and baseline paths, where the signal path interrogates a HCN vapour cell. The absorption profile is constructed by decoding the intra-comb beat amplitudes in digital signal processing (DSP). Baselining is performed by dividing the signal output by the baseline output, generating the final absorption profile.

The generation and digital interferometric tagging of the multiple loop transit fields follows in exactly the fashion as the re-entrant line dispersion spectroscopy technique presented in the previous chapter. Using an AOM driven at a radio frequency of 38 MHz, the resulting RF comb is first characterized on a spectrum analyzer in Figure 7.2 below:

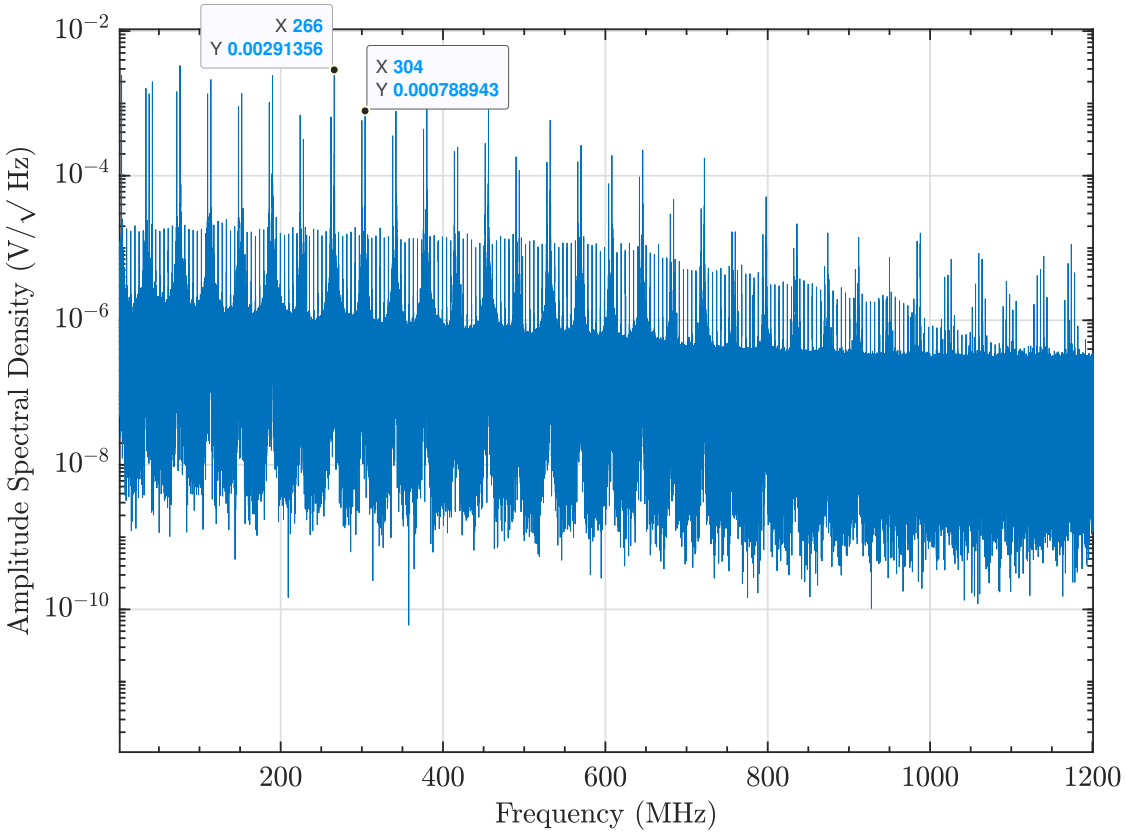

Figure 7.2: The comb spectrum with an AOM drive frequency of 38 MHz is plotted. We have labelled two of the comb teeth (266 MHz and 304 MHz) to illustrate the 38 MHz tooth spacing. The spectrum rolls off at frequencies greater than 600 MHz due to the 1 GHz bandwidth of the photodetector used.

From the spectrum analyzer trace, there is ≤ 3 dB loss over 400 MHz bandwidth, demonstrating the ability to generate a comb with at least 10 teeth; the bandwidth only being limited by the photodetector and spectrum analyzer bandwidth of 1 GHz. To remove the effect of this spectral rolloff, the comb is split into two paths by a 3 dB coupler, one interrogating the vapor cell, and the other acting as a baseline. By dividing the demodulated amplitude of the two combs, it is thus possible to remove the comb envelope from an amplitude measurement.

A key feature of the digital interferometric frequency comb is self-baselining and RF mixdown. As in reentrant dispersion spectroscopy presented in the previous chapter, each tooth is interfered with the previous tooth, and hence the interference occurs at a heterodyne frequency equal to the AOM shift, which is at most, tens to hundreds of MHz. Thus spectroscopic information is compressed to within the acousto-optic shift frequency, removing the need for high speed RF electronics needed to demodulate multi-GHz signals. This further enhances the suitability for using this technique to interrogate wide transitions. At the time of the writing of this thesis, a paper has been submitted for review, using this technique to measure the absorption across a 1 GHz HCN transition without laser wavelength tuning.

Future work on the comb will focus on obtaining a phase readout from each of the comb channels, in addition to absorption, allowing for a tuning free reconstruction of the disper-

sion profile. This is challenging, as amplified stimulated emission (ASE) noise amplifies the digital interferometric code noise associated with each pass of the delay line. Standard digital interferometry as described in this thesis offers 1/N suppression of this noise, with N being the code length. This is the fundamental autocorrelation property of the m-sequences used for DI. For a system with a handful of multiplexed signals, such as reentrant dispersion spectroscopy with three, a code length of 2047 (11 bits) is sufficient to achieve microradian phase noise floors. However, in the digital interferometric comb, at least twenty multiplexed channels are required to encompass the broad wings of a pressure-broadened 1 GHz transition. This leads to a compounding of phase noise associated with the higher order comb teeth, and rapidly deteriorating phase and concentration sensitivity by the tenth tooth. We can also think of this effect as cross-talk between the DI codes attached to each pass of the delay line. With twenty passes, the RF spectrum becomes extremely congested with cross talk between the DI modulated comb teeth.

This can be overcome by resorting to extremely long code lengths, but at the expense of throttling the measurement bandwidth. Alternatively, current work on digital interferometric algorithms focuses on developing low crosstalk DI codes [95], demonstrating crosstalk 40 dB lower than in standard DI. By implementing this new algorithm, we hope to reduce the impact of EDFA amplified code noise. We hope to simultaneously recovering the phase of more than twenty teeth with microradian phase sensitivity, which will allow for a tuning free reconstruction of the dispersion profile, along with absorption.

7.1.2 Dispersion Spectroscopy for Metasurface Sensing

Simultaneously, work is ongoing on applying dispersion spectroscopy techniques to metasurface sensing. Metasurfaces, two-dimensional arrays of subwavelength nanostructures, have emerged as powerful tools for sensing applications due to their ability to be engineered to manipulate electromagnetic waves with high precision. By tailoring their geometrical and material properties, metasurfaces can exhibit optical responses such as resonance shifts [98], polarization rotation [99], and phase modulation [100], making them highly sensitive to environmental changes. Notably, the magnitude of these optical effects, as well as the wavelength at which that they occur can be tailored. Here, we focus on resonance shift-based sensing, as our work on dispersion spectroscopy detects phase shifts around resonances.

One of the most prominent mechanisms for metasurface-based sensing is the shift in resonance frequency upon interaction with external analytes. Metasurfaces are typically designed to support plasmonic or Mie resonances, which are highly dependent on the refractive index of the surrounding medium. When a target analyte such as an antibody, or other complex molecule is introduced, its presence alters the local refractive index, leading to a measurable shift in the resonance wavelength or frequency.

The mechanism behind resonance shift-based sensing relies on the Mie oscillations of circular displacement currents in the dielectric medium that metasurface nanostructures support [101]. These resonances are dictated by the effective refractive index of the metasurface system, which consists of both the structured material and the surrounding medium. When an analyte binds to the metasurface or alters the surrounding refractive index, the effective refractive index changes, leading to a shift in the resonance condition. In general, this resonance shift is linearly proportional with the number of analyte molecules present.

Analogous to molecular resonances, a dispersion induced phase shift is also associated with each resonance.

In the work here, we focus on dielectric metasurfaces. These structures are composed of grids of nanoscale high-refractive-index materials such as silicon or titanium dioxide. These structures leverage Mie resonances, which are highly sensitive to refractive index variations. Compared to plasmonic metasurfaces, they have lower absorption loss from Ohmic heating and vibrational modes, and thus exhibit higher Q, sharper resonances. At the same time, the resonance shift per analyte molecule remains just as high as plasmonic metasurfaces, rendering dielectric metasurfaces equivalent in sensitivity [102].

Traditionally, metasurfaces are characterized, and their resonance shifts read out using intensity based techniques . These techniques include spectrometers, hyperspectral imaging, and microscopy. However, like absorption spectroscopy, these techniques suffer from source intensity fluctuations, and require baselining. Additionally, metasurfaces tend to have sharper dispersion profile compared to its transmission [103], allowing for higher sensitivity with dispersion based measurements. Thus, recent work has been done on phase sensing techniques for metasurfaces, including ellipsometery, and lateral shearing interferometry, which generate spatial interferograms [104]. In our work, we introduce dispersion spectroscopy as an alternative phase sensitive technique.

To characterize the dispersion properties of the metasurface resonance, we constructed a Mach Zehnder interferometer, shown in Figure 7.3. The in-line Mach Zehdner configuration was chosen here, instead of the Sagnac to simplify the free-space optics used to interrogate the metasurface.

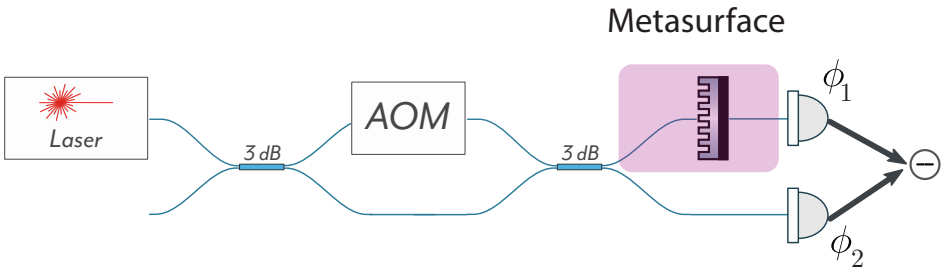

Figure 7.3: The incident laser field is split by a 3 dB coupler into a shifted path through a 200 MHz AOM and an unshifted path, forming a carrier and sideband. The fields are then recombined at a 3 dB coupler and split again by a second 3 dB coupler. The shifted and unshifted fields sample the metasurface dispersion curve at two frequencies, giving a phase readout equal to the derivative of the dispersion curve. The second port of the 3 dB coupler output is used to form a baseline phase readout. This is used to subtract path length noise accrued in the AOM interferometer. The purple shaded box shows the free space optics used to couple light from fiber to the metasurface. This setup is shown in Figure 7.4 below.

Here, the incident laser field is split by a 3 dB coupler, with one of the paths shifted by an acousto-optic modulator, forming a carrier and a sideband, in frequency domain. The two fields are recombined via a second 3 dB coupler and then interfered on a metasurface. The carrier and sideband sample the metasurface dispersion at two different frequencies, which is the same principle throughout the other work presented in this thesis. At the photodetector, the result is a heterodyne frequency, with phase of the resulting readout

equal to the local derivative of the dispersion curve. The intensity measured by the photodetector is given in Equation 7.1 below:

$$P \propto \cos[\omega_s t + \phi_{\text{meta}}(\omega_L + \omega_s) - \phi_{\text{meta}}(\omega_L)] \tag{7.1}$$

where ω_s is the AOM shift frequency ω_L is the laser frequency, and ϕ_{meta}, is the dispersion response of the metasurface.

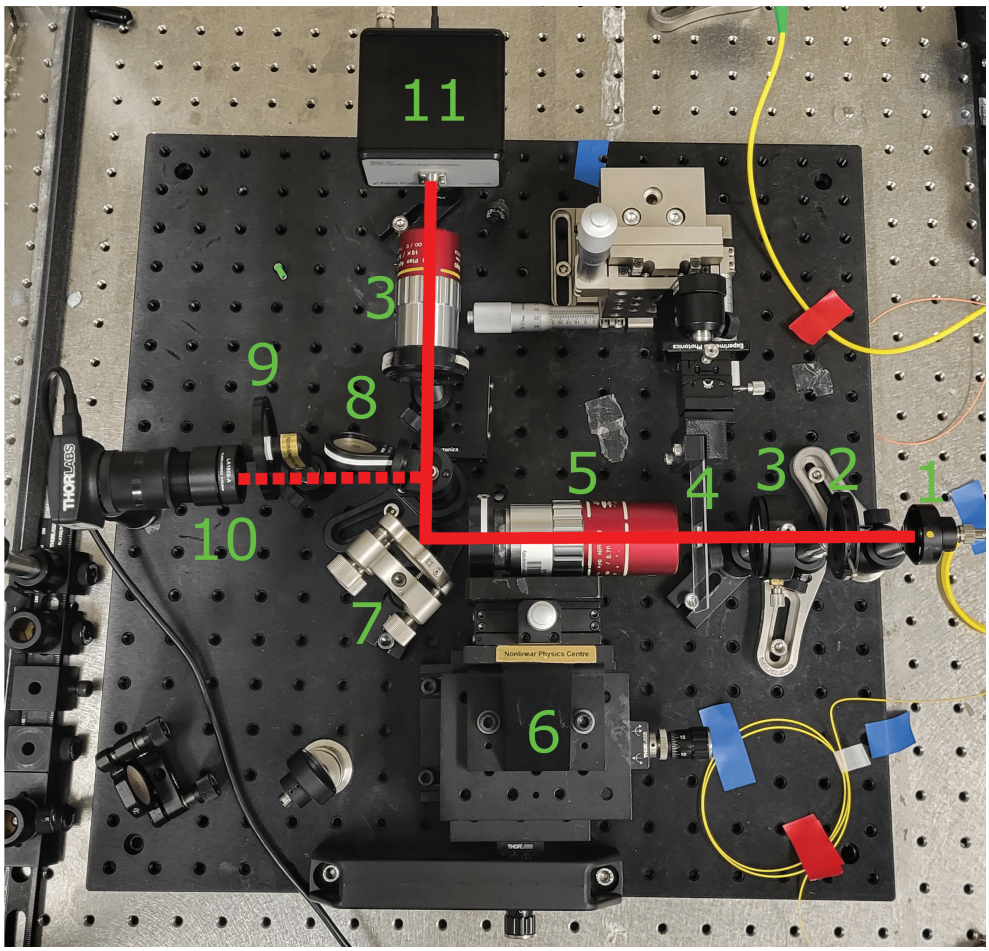

Figure 7.4: Free space optics corresponding to the purple box in Figure 7.31. An input fiber collimator (1) is used to launch the output of the 3 dB coupler into free space. An aperture (2) is used to restrict the beam size to the size of the metasurface substrate. The apodized beam is focused by a lens (3) onto a microscope slide (4) containing the metasurface. The slide is mounted to a translation stage (6) for alignment. The output beam phase modulated by the metasurface is directed to a microscope objective (5) to prevent the beam from diverging, and then directed to a mirror (7), providing a 90 degree dogleg, and thus a more compact optical arrangement. A flip mirror (8) is used to toggle between two paths, an alignment path, and the primary phase readout path. In the alignment path, there is a neutral density filter (9) and a camera (10). This is used in conjunction with the translation stage (6) to ensure alignment of the beam onto the micron scale surface area of the metasurface array. In the primary phase readout path, a third lens (3) is used to focus the beam onto a photodetector (11).

Post heterodyne mixdown of the photodetector signal, the readout of this interferometer is similar to that of Sagnac dispersion spectroscopy, which also yields a derivative of the dispersion. The subtraction of the phase readout from the two photodetectors was inspired by the work done on re-entrant dispersion spectroscopy. This subtraction aims to remove interferometric path length noise in the up-front AOM interferometer used to generate the probing sideband.

Upon tuning the laser over the metasurface resonance, the signal shape should be similar to that of Sagnac dispersion spectroscopy. Unfortunately, at the time of the writing of this thesis, we were unable to recover the dispersion profile of the metasurface. This is due to the metasurface having a FWHM of 125 GHz (100 pm). Recalling that the Sagnac dispersion signal is maximized with an AOM shift frequency on the order of half the resonance FWHM, it follows that since the shift is less than 1 percent of the FWHM, the signal is extremely weak.

At present, we address this limitation from two directions: firstly, we are having a metasurface with a narrower resonance (10-20 GHz) fabricated. Secondly, we are planning to interrogate the metasurface with the digital interferometric frequency comb. With an AOM frequency shift of 200 MHz and 30 teeth, the comb should span 6 GHz. This is ideally suited to interrogate a metasurface with a FWHM of 10 GHz. We also note that the uni-directional configuration of the digital interferometric comb also allows for easier free-space interrogation of the metasurface

7.2 Epilogue

Absorption and dispersion, or amplitude and phase, are intrinsically linked quantities for any resonance. Any absorption line will have an associated dispersion profile that can be calculated using the Kramers Kronig relations. In absorption, we measure the decrease in amplitude of an optical field due to an absorbing molecular transition. This is relatively easy to do, as we simply measure the decrease in power on a photodetector. However, this also means that amplitude fluctuations directly couple into the readout. Additionally, absorbance does not scale linearly with concentration, making large dynamic range measurements challenging. Alternatively, measuring dispersion induced phase shifts allows for a readout linear with concentration and to first order, immune to amplitude fluctuations, but measuring dispersion induced phase shifts with high precision is challenging. For molecular transitions in the near-infrared, dispersion induced phase shifts are fractions of a radian in magnitude, requiring sensitive interferometric methods to extract with good signal to noise ratio.

This thesis has aimed to apply recent developments in digital interferometric techniques to dispersion spectroscopy. As a measurement of phase, dispersion spectroscopy has always drawn from a rich history of interferometric techniques. The past century has seen the application of photographic fringe counting (hook method), photoelectric fringe counting (laser interferometry), and recently, direct phase readout (heterodyne phase sensitive interferometry) to dispersion techniques. With each generation, the concentration sensitivity of dispersion methods has increased. The work presented here aims to continue this tradition by applying digital interferometry to dispersion spectroscopy.

We demonstrated two methods, both relying on frequency noise suppression, to enhance the concentration sensitivity of dispersion interferometers. These are the use of a balanced

path length interferometer with a digital interferometric readout, or the digital synthesis of an equivalent balanced interferometer. We first present a balanced path length Sagnac interferometer as a testbed for digital interferometry. We introduced a modified technique for digital interferometry, called homodyne digital interferometry that is compatible with the Sagnac interferometer. The common path configuration of the Sagnac interferometer provided inherent frequency and path length noise suppression. We conducted a noise floor measurement, analyzing and accounting for noise sources, finding that the phase sensitivity of the interferometer was only limited by electronic noise and shot noise to the 2×10^{-7} rad/$\sqrt{\text{Hz}}$ level. This demonstrates the range gating ability of DI to reject scattering fields present in the traditional Sagnac interferometer.

Building on the DI testbed system developed in Chapter 4, Chapter 5 detailed the implementation of a Sagnac-based spectrometer for molecular gas sensing, where a vapor cell is integrated into the Sagnac loop. This is a novel interferometer architecture for dispersion spectroscopy, owing to the traditional difficulty in implementing phase recovery for a Sagnac interferometer. Using the Digital Homodyne interferometric readout introduced in Chapter 4, we successfully recovered a dispersion induced phase signal, and also derived the theoretical phase signal expected from the readout, showing that the phase signal is proportional to the derivative of anomalous dispersion. Experimental results demonstrated excellent agreement with this theoretical dispersion profile, validating the spectroscopic measurement. An off-transition measurement of the phase noise demonstrated a 0.8 μrad/$\sqrt{\text{Hz}}$ noise floor for this technique, showing this is equivalent to 159 ppb $\times$ m/$\sqrt{\text{Hz}}$ concentration sensitivity, comparable to existing dispersion spectroscopy techniques such as CLADs and HPSDS. We also discussed systematic errors that may arise from this technique, including a the impact of fiber dispersion, and laser tuning nonlinearity.

The final experimental chapter built on digital interferometric phase extraction techniques from previous dispersion spectroscopy work. However, instead of a Sagnac interferometer, we introduced re-entrant delay-line spectroscopy, a novel approach leveraging digital interferometric code-division multiplexing. This technique enables simultaneous interrogation of multiple optical paths traveling in a re-entrant delay line. Here, the phase signal is formed from the subtraction of phases accrued through two consecutive passes of the re-entrant delay line. This yields a phase signal proportional to the second derivative of dispersion, and allows for subtraction of frequency and path length noise accrued during the loop transits. This is functionally equivalent to digitally synthesizing a common path interferometer, like the Sagnac. Despite its slightly higher demodulation complexity compared to the Sagnac system, the re-entrant approach offered greater configurational flexibility, owing to its unidirectional topology.

Experimental results also demonstrated good agreement with a theoretical dispersion profile, which in contrast to the Sagnac spectrometer first derivative signal, was the second derivative of dispersion. The interferometer configuration also allowed for linearization of laser thermal tuning over the transition, addressing laser tuning nonlinearity seen in the Sagnac readout. This removed another source of systematic error that would otherwise have to be baselined out. With this synthesized common path interferometer, we reached a noise floor of 2 μrad/$\sqrt{\text{Hz}}$ and a converted concentration detection limit of 159 ppb $\times$ m/$\sqrt{\text{Hz}}$. This was only a factor of two lower than the concentration sensitivity of the Sagnac dispersion spectrometer. However, this is still within the range of existing

dispersion spectroscopy methods. Given the configurational flexibility offered by this architecture, as well as the ability to perform tuning nonlinearity correction, we believe that this is a worthwhile tradeoff in sensitivity.

As we close this thesis, we look ahead to recent and future developments in dispersion spectroscopy that have opened the door for further configurational flexibility. It is the ethos of digital interferometry to simplify optical complexity, offloading it to digital signal processing. We have done this in moving from the Sagnac configuration with the vapor cell somewhat awkwardly placed within the sensing loop, to a digitally synthesized balanced interferometer interrogating an inline vapor cell. In recently published work on the digital interferometric comb, we further remove a layer of optical complexity by doing away with laser tuning. Here, we harness the powerful multiplexing capability of DI to simultaneously demodulate the amplitude of up to twenty comb teeth, spanning across the full width half maximum of a 1 GHz absorption line. More sophisticated digital signal processing schemes and algorithms developed for DI will also enable the phase of these comb teeth to be recovered with high fidelity, paving the way for a broadband dispersion measurement, in addition to absorption. We hope this will unlock dispersion techniques for metasurface sensing, which span multiple GHz in linewidth, opening the door for dispersion-enabled sensing of complex biomolecules.

Bibliography

[1] W. C. Marlow. Hakenmethode. *Appl. Opt.*, 6(10):1715–1724, Oct 1967.

[2] Jerome Workman. A review of the latest spectroscopic research in pharmaceutical and biopharmaceutical applications. *Spectroscopy*, pages 25–29, 08 2024.

[3] Margherita Maiuri, Marco Garavelli, and Giulio Cerullo. Ultrafast spectroscopy: State of the art and open challenges. *Journal of the American Chemical Society*, XXXX, 12 2019.

[4] Steven Schill, R. McEwan, Ryan Moffet, Josette Marrero, Clinton MacDonald, and Eric Winegar. Real-world application of open-path uv-doas, tdl, and ft-ir spectroscopy for air quality monitoring at industrial facilities. *Spectroscopy*, pages 18–22, 11 2022.

[5] KM Merrill and ST Ridgway. Infrared spectroscopy of stars. *In: Annual review of astronomy and astrophysics. Volume 17.(A79-54126 24-90) Palo Alto, Calif., Annual Reviews, Inc., 1979, p. 9-41. USAF-NASA-NSF-supported research.*, 17:9–41, 1979.

[6] Michal Nikodem and Gerard Wysocki. Chirped laser dispersion spectroscopy for remote open-path trace-gas sensing. *Sensors*, 12, 12 2012.

[7] Michal Nikodem, Genevieve Plant, David Sonnenfroh, and Gerard Wysocki. Open-path sensor for atmospheric methane based on chirped laser dispersion spectroscopy. *Applied Physics B*, 119:3–9, 04 2014.

[8] John David Jackson. *Classical electrodynamics*. Wiley, New York, NY, 3rd ed. edition, 1999.

[9] Alicja Dabrowska, Stefan Lindner, Andreas Schwaighofer, and Bernhard Lendl. Mid-ir dispersion spectroscopy – a new avenue for liquid phase analysis. *Spectrochimica Acta Part A: Molecular and Biomolecular Spectroscopy*, 286:122014, 2023.

[10] Thomas Mayerhöfer and Jürgen Popp. Beer's law – why absorbance depends (almost) linearly on concentration. *ChemPhysChem*, 20, 01 2019.

[11] Henk Arnoldus. Power absorption by a dipole in a laser beam. *Journal of Modern Optics*, 69:381–391, 03 2022.

[12] P. Weijer and R. Cremers. Hook method: improvement and simplification of the experimental setup. *Applied Optics*, 22:3500–3502, 11 1983.

[13] Martin C. E. Huber. Interferometric gas diagnostics by the hook method. *Modern Optical Methods in Gas Dynamic Research*, 02 1971.

[14] M Crance, P Juncar, and J Pinard. A new method for measuring relative oscillator strengths using a cw dye laser. *Journal of Physics B: Atomic and Molecular Physics*, 8(15):2461, oct 1975.

[15] A B Duval and A I McIntosh. Measurement of oscillator strength by tunable laser interferometry. *Journal of Physics D: Applied Physics*, 13(9):1617, sep 1980.

[16] J. Moschella, R. Hazelton, and M. Keitz. Resonant, heterodyne laser interferometer for state density measurements in atoms and ions. *Review of Scientific Instruments*, 77:093108–093108, 09 2006.

[17] Gerard Wysocki and Damien Weidmann. Molecular dispersion spectroscopy for chemical sensing using chirped mid-infrared quantum cascade laser. *Optics Express*, 18(25):26123, Dec 2010.

[18] Genevieve Plant. *Chirped Laser Dispersion Spectroscopy: Fundamentals and Applications*. Phd thesis, Princeton University, Princeton, NJ, June 2016. Available at http://arks.princeton.edu/ark:/88435/dsp01w66346117.

[19] Michal Nikodem and Gerard Wysocki. Suppressing the influence of optical fringes in dispersion spectroscopy. *Photonics Letters of Poland*, 5(4):pp. 152–154, Dec. 2013.

[20] Michal Nikodem, Damien Weidmann, Clinton Smith, and Gerard Wysocki. Signal-to-noise ratio in chirped laser dispersion spectroscopy. *Opt. Express*, 20(1):644–653, Jan 2012.

[21] Michał Nikodem and Gerard Wysocki. Differential optical dispersion spectroscopy. *IEEE Journal of Selected Topics in Quantum Electronics*, 23(2):464–468, 2017.

[22] Michal Nikodem, Genevieve Plant, Zhenxing Wang, Paul Prucnal, and Gerard Wysocki. Chirped lasers dispersion spectroscopy implemented with single- and dual-sideband electro-optical modulators. *Opt. Express*, 21(12):14649–14655, Jun 2013.

[23] Michal Nikodem, Karol Krzempek, Renata Karwat, Grzegorz Dudzik, Krzysztof Abramski, and Gerard Wysocki. Chirped laser dispersion spectroscopy with differential frequency generation source. *Optics Letters*, 39, 07 2014.

[24] Pedro Martín-Mateos and Pablo Acedo. Heterodyne phase-sensitive detection for calibration-free molecular dispersion spectroscopy. *Opt. Express*, 22(12):15143–15153, June 2014. Publisher: OSA.

[25] Pedro Martín-Mateos, Borja Jerez, Cristina De Dios, and P. Acedo. Mid-infrared heterodyne phase-sensitive dispersion spectroscopy using difference frequency generation. *Applied Physics B*, 124, 03 2018.

[26] Pedro Martín-Mateos, Jakob Hayden, Pablo Acedo, and Bernhard Lendl. Heterodyne phase-sensitive dispersion spectroscopy in the mid-infrared with a quantum cascade laser. *Analytical Chemistry*, 89(11):5916–5922, 2017. PMID: 28480710.

[27] Kun Duan, Mengyuan Hu, Yongbin Ji, Zhimin Lu, Shunchun Yao, and Wei Ren. High-temperature ammonia detection using heterodyne phase-sensitive dispersion spectroscopy at 9.06 µm. *Fuel*, 325:124852, 2022.

[28] Genevieve Plant, Yifeng Chen, and Gerard Wysocki. Optical heterodyne-enhanced chirped laser dispersion spectroscopy. *Opt. Lett.*, 42(14):2770–2773, Jul 2017.

[29] Mengyuan Hu and Wei Ren. Wavelength-modulation dispersion spectroscopy of no with heterodyne phase-sensitive detection. *Opt. Lett.*, 47(11):2899–2902, Jun 2022.

[30] Liuhao Ma, Zhen Wang, Kin-Pang Cheong, Hongbo Ning, and Wei Ren. Temperature and h2o sensing in laminar premixed flames using mid-infrared heterodyne phase-sensitive dispersion spectroscopy. *Applied Physics B*, 124(6):117, May 2018.

[31] Mingli Zou, Liqun Sun, and Shaomin Li. Simultaneous measurement of gas absorption and path length based on the dual-sideband heterodyne phase-sensitive detection of dispersion spectroscopy. *Opt. Express*, 29(8):11683–11692, Apr 2021.

[32] Andreas Hangauer, Yifeng Chen, and Gerard Wysocki. Chirped laser dispersion spectroscopy for spectroscopic chemical sensing with simultaneous range detection. *Opt. Lett.*, 46(2):198–201, Jan 2021.

[33] Yifeng Chen, Michael Soskind, James McSpiritt, Jie Liu, Rui Wang, Nathan Li, Xuehui Guo, Mark A. Zondlo, and Gerard Wysocki. Fugitive methane detection using open-path stand-off chirped laser dispersion spectroscopy. *Opt. Lett.*, 46(13):3005–3008, Jul 2021.

[34] Laser Dispersion Spectroscopy — Mirico — mirico.co.uk. https://www.mirico.co.uk/laser-dispersion-spectroscopy. [Accessed 24-02-2025].

[35] Daniel A. Shaddock. Digitally enhanced heterodyne interferometry. *Opt. Lett.*, 32(22):3355–3357, Nov 2007.

[36] Stephen M. Trimberger. Three ages of fpgas: A retrospective on the first thirty years of fpga technology. *Proceedings of the IEEE*, 103(3):318–331, 2015.

[37] Oliver Gerberding. Deep frequency modulation interferometry. *Opt. Express*, 23(11):14753–14762, Jun 2015.

[38] Haotian Yu, Dongliang Zheng, Jiaan Fu, Yi Zhang, Chao Zuo, and Jing Han. Deep learning-based fringe modulation-enhancing method for accurate fringe projection profilometry. *Opt. Express*, 28(15):21692–21703, Jul 2020.

[39] Andrew J. Sutton, Oliver Gerberding, Gerhard Heinzel, and Daniel A. Shaddock. Digitally enhanced homodyne interferometry. *Opt. Express*, 20(20):22195–22207, Sep 2012.

[40] Glenn de Vine, David S. Rabeling, Bram J. J. Slagmolen, Timothy T-Y. Lam, Sheon Chua, Danielle M. Wuchenich, David E. McClelland, and Daniel A. Shaddock. Picometer level displacement metrology with digitally enhanced heterodyne interferometry. *Opt. Express*, 17(2):828–837, Jan 2009.

[41] David J. Bowman, Malcolm J. King, Andrew J. Sutton, Danielle M. Wuchenich, Robert L. Ward, Emmanuel A. Malikides, David E. McClelland, and Daniel A.

Shaddock. Internally sensed optical phased array. *Opt. Lett.*, 38(7):1137–1139, Apr 2013.

[42] Ya Zhang, Chathura P. Bandutunga, Malcolm B. Gray, and Jong H. Chow. Multi-target cw interferometric acoustic measurements on a single optical beam. *Opt. Express*, 27(13):18477–18483, Jun 2019.

[43] Silvie Ngo, Terry G. McRae, Malcolm B. Gray, and Daniel A. Shaddock. Homodyne digital interferometry for a sensitive fiber frequency reference. *Opt. Express*, 22(15):18168–18176, Jul 2014.

[44] Silvie Ngo, Daniel A. Shaddock, Terry G. McRae, Timothy T-Y. Lam, Jong H. Chow, and Malcolm B. Gray. Suppressing rayleigh backscatter and code noise from all-fiber digital interferometers. *Opt. Lett.*, 41(1):84–87, Jan 2016.

[45] C. P. Bandutunga, Y. Zhang, T. G. Mcrae, M. B. Gray, and J. H. Chow. Coherent rayleigh backscatter phase noise in digitally enhanced fiber interferometers. *Journal of Lightwave Technology*, pages 1–1, 2021.

[46] Terry G. McRae, Silvie Ngo, Timothy T-Y. Lam, David. E. McClelland, Jong H. Chow, Daniel A. Shaddock, and Malcolm B. Gray. Algebraic cancellation of polarisation noise in fibre interferometers. *Opt. Express*, 24(10):10486–10494, May 2016.

[47] John L. Hall. Nobel lecture: Defining and measuring optical frequencies. *Rev. Mod. Phys.*, 78:1279–1295, Nov 2006.

[48] Nathalie Picqué and Theodor W. Hänsch. Frequency comb spectroscopy. *Nature Photonics*, 13(3):146–157, March 2019.

[49] Arman Cingoz, Dylan Yost, Thomas Allison, Axel Ruehl, Martin Fermann, Ingmar Hartl, and Jun Ye. Direct frequency comb spectroscopy in the extreme ultraviolet. *Nature*, 482:68–71, 02 2012.

[50] Lora Nugent-Glandorf, Tyler Neely, Florian Adler, Adam J. Fleisher, Kevin C. Cossel, Bryce Bjork, Tim Dinneen, Jun Ye, and Scott A. Diddams. Mid-infrared virtually imaged phased array spectrometer for rapid and broadband trace gas detection. *Opt. Lett.*, 37(15):3285–3287, Aug 2012.

[51] Ian Coddington, Nathan Newbury, and William Swann. Dual-comb spectroscopy. *Optica*, 3(4):414–426, Apr 2016.

[52] A. M. Zolot, F. R. Giorgetta, E. Baumann, J. W. Nicholson, W. C. Swann, I. Coddington, and N. R. Newbury. Direct-comb molecular spectroscopy with accurate, resolved comb teeth over 43 thz. *Opt. Lett.*, 37(4):638–640, Feb 2012.

[53] Julien Roy, Jean-Daniel Deschênes, Simon Potvin, and Jérôme Genest. Continuous real-time correction and averaging for frequency comb interferometry. *Opt. Express*, 20(20):21932–21939, Sep 2012.

[54] Takuro Ideguchi, Antonin Poisson, Guy Guelachvili, Nathalie Picqué, and Theodor Haensch. Adaptive real-time dual-comb spectroscopy. *Nature communications*, 5:3375, 02 2014.

[55] Khaoula Fdil, Vincent Michaud-Belleau, Nicolas Bourbeau Hébert, Philippe Guay, Adam J. Fleisher, Jean-Daniel Deschênes, and Jéróme Genest. Dual electro-

optic frequency comb spectroscopy using pseudo-random modulation. *Opt. Lett.*, 44(17):4415–4418, Sep 2019.

[56] Alexandre Parriaux, Kamal Hammani, and Guy Millot. Electro-optic frequency combs. *Adv. Opt. Photon.*, 12(1):223–287, Mar 2020.

[57] Tao Chen, Wei Kong, Hao Liu, and Rong Shu. Frequency-stepped pulse train generation in an amplified frequency-shifted loop for oxygen a-band spectroscopy. *Opt. Express*, 26(26):34753–34762, Dec 2018.

[58] Pedro Martín-Mateos, Borja Jerez, Pedro Largo-Izquierdo, and Pablo Acedo. Frequency accurate coherent electro-optic dual-comb spectroscopy in real-time. *Opt. Express*, 26(8):9700–9713, Apr 2018.

[59] Lawrence Robert Trask, Srinivas Varma Pericherla, and Peter J. Delfyett. Self-oscillating, self-stabilizing, and self-referenced electro-optic comb. *Opt. Express*, 33(2):3429–3437, Jan 2025.

[60] Vicente Durán, Côme Schnébelin, and Hugues Guillet de Chatellus. Coherent multi-heterodyne spectroscopy using acousto-optic frequency combs. *Optics Express*, 26(11):13800–13809, May 2018. Publisher: Optical Society of America.

[61] Climate Change Indicators: Atmospheric Concentrations of Greenhouse Gases — US EPA — epa.gov. https://www.epa.gov/climate-indicators/climate-change-indicators-atmospheric-concentrations-greenhouse-gases. [Accessed 19-02-2025].

[62] George Stewart. *Laser and Fiber Optic Gas Absorption Spectroscopy*. Cambridge University Press, 2021.

[63] Kate A. Whittaker, James Keaveney, Ifan G. Hughes, and Charles S. Adams. Hilbert transform: Applications to atomic spectra. *Phys. Rev. A*, 91:032513, Mar 2015.

[64] Thomas Mayerhöfer, Alicja Dabrowska, Andreas Schwaighofer, Bernhard Lendl, and Jürgen Popp. Beyond beer's law: Why the index of refraction depends (almost) linearly on concentration. *ChemPhysChem*, 21, 03 2020.

[65] Georges Durry, Virginie Zéninari, Bertrand Parvitte, Thibault Le Barbu, Franck Lefèvre, J. Ovarlez, and R.-R. Gamache. Pressure-broadening coefficients and line strengths of H2O near 1.39 μm: application to the in situ sensing of the middle atmosphere with balloonborne diode lasers. *Journal of Quantitative Spectroscopy and Radiative Transfer*, 94:387–403, 2005.

[66] William C. Swann and Sarah L. Gilbert. Line centers, pressure shift, and pressure broadening of 1530-1560 nm hydrogen cyanide wavelength calibration lines. *Journal of the Optical Society of America B*, 22(8):1749, Aug 2005.

[67] W. Demtröder. *Laser Spectroscopy: Vol. 1: Basic Principles*. Laser Spectroscopy. Springer Berlin Heidelberg, 2008.

[68] Xianglei Huang and Yuk Yung. A common misunderstanding about the voigt line profile. *Journal of the Atmospheric Sciences*, 61, 07 2004.

[69] John F. Kielkopf. New approximation to the voigt function with applications to spectral-line profile analysis. *J. Opt. Soc. Am.*, 63(8):987–995, Aug 1973.

[70] Xiaobin Zhou, Gang Zhao, Yong Li, Ziwei Cheng, Kang Jiao, Bofeng Zhang, Zihao Zhang, Yanke Li, Xiaojuan Yan, Weiguang Ma, and Suotang Jia. Optical feedback noise-immune cavity-enhanced optical heterodyne molecular spectrometry for sub-doppler-broadened detection of c2h2. *Optics Letters*, 49, 01 2024.

[71] Peter Werle and Franz Slemr. Signal-to-noise ratio analysis in laser absorption spectrometers using optical multipass cells. *Applied Optics*, 30:430–434, 02 1991.

[72] R. Pickholtz, D. Schilling, and L. Milstein. Theory of spread-spectrum communications - a tutorial. *IEEE Transactions on Communications*, 30(5):855–884, 1982.

[73] Silvie Ngo, Terry Mcrae, Malcolm Gray, and Daniel Shaddock. Homodyne digital interferometry for a sensitive fiber frequency reference. *Optics Express*, 22, 07 2014.

[74] Hervé C. Lefèvre. The fiber-optic gyroscope, a century after sagnac's experiment: The ultimate rotation-sensing technology? *Comptes Rendus Physique*, 15(10):851–858, 2014. The Sagnac effect: 100 years later / L'effet Sagnac : 100 ans après.

[75] Jacob Nemr Chamoun and Michel J. F. Digonnet. Noise and bias error due to polarization coupling in a fiber optic gyroscope. *Journal of Lightwave Technology*, 33(13):2839–2847, 2015.

[76] Danielle M. R. Wuchenich, Timothy T.-Y. Lam, Jong H. Chow, David E. McClelland, and Daniel A. Shaddock. Laser frequency noise immunity in multiplexed displacement sensing. *Opt. Lett.*, 36(5):672–674, Mar 2011.

[77] Dan Popescu, Lin-P'ing Choo-Smith, Costel Flueraru, Youxin Mao, Shoude Chang, John Disano, Shehab Sherif, and Michael Sowa. Optical coherence tomography: Fundamental principles, instrumental designs and biomedical applications. *Biophysical Reviews*, 3:155–169, 09 2011.

[78] Lionel Jacubowiez, Jean-Francois Roch, Jean-Philippe Poizat, and Philippe Grangier. Teaching about photodetection noise sources in the laboratory. In Christiaan H. F. Velzel, editor, *Fifth International Topical Meeting on Education and Training in Optics*, volume 3190, pages 166 – 178. International Society for Optics and Photonics, SPIE, 1997.

[79] Kwok K. Ng. *pin Photodiode*, pages 431–437. 2002.

[80] sweptlaser.com. https://www.sweptlaser.com/sites/default/files/files/photodetector_guide.pdf. [Accessed 21-02-2025].

[81] National Instruments. *NI 5781R User Guide and Specifications*, 2 2023.

[82] Justin Wong, Chathura P. Bandutunga, Ya Zhang, Malcolm B. Gray, and Jong H. Chow. Digitally enhanced molecular dispersion spectroscopy. *Opt. Lett.*, 45(22):6290–6293, Nov 2020.

[83] Michal Nikodem and Gerard Wysocki. Molecular dispersion spectroscopy - new capabilities in laser chemical sensing: Molecular dispersion spectroscopy. *Annals of the New York Academy of Sciences*, 1260(1):101–111, Jul 2012.

[84] Genevieve Plant, Michal Nikodem, David Sonnenfroh, and Gerard Wysocki. In *CLEO: 2013*, page JW2A.79. Optical Society of America, 2013.

[85] Pedro Martín-Mateos, Borja Jerez, and P. Acedo. Heterodyne architecture for tunable laser chirped dispersion spectroscopy using optical processing. *Optics letters*, 39:2611–2613, 05 2014.

[86] Pedro Martín-Mateos and Pablo Acedo. Heterodyne phase-sensitive detection for calibration-free molecular dispersion spectroscopy. *Opt. Express*, 22(12):15143–15153, Jun 2014.

[87] Genevieve Plant. *Chirped Laser Dispersion Spectroscopy: Fundamentals and Applications*. PhD thesis, Princeton University, 2016.

[88] Gowind P. Agrawal. *Fiber-Optic Communication Systems*. John Wiley & Sons, 3rd edition, 2002.

[89] Corning. *Corning SMF28 Optical Fiber Product Information*, 4 2002.

[90] Rajiv Ramaswami and Kumar N. Sivarajan. *Optical networks: a practical perspective*. Morgan Kaufmann Publishers Inc., San Francisco, CA, USA, 1998.

[91] Justin Wong, Chathura Bandutunga, Priya Singh, Malcolm Gray, and Jong Chow. Molecular dispersion spectroscopy using a code-division-multiplexed optical carrier. *Physical Review Applied*, 19, 04 2023.

[92] Ya Zhang, Chathura P. Bandutunga, Malcolm B. Gray, and Jong H. Chow. Multi-target cw interferometric acoustic measurements on a single optical beam. *Optics Express*, 27:18477, 06 2019.

[93] Fang Wei, Fei Yang, Xi Zhang, Dan Xu, Meng Ding, Li Zhang, Dijun Chen, Haiwen Cai, Zujie Fang, and Gu Xijia. Subkilohertz linewidth reduction of a dfb diode laser using self-injection locking with a fiber bragg grating fabry-perot cavity. *Opt. Express*, 24(15):17406–17415, Jul 2016.

[94] Paul Sibley, Robert Ward, Lyle Roberts, Daniel Shaddock, and Samuel Francis. Crosstalk reduction for multi-channel optical phase metrology. *Optics Express*, 28, 03 2020.

[95] Anneshwa Dey, Ya Zhang, Justin Wong, Paul G. Sibley, Chathura P. Bandutunga, Malcolm B. Gray, and Jong H. Chow. Algebraic cancellation of inter-channel cross talk in multiplexed heterodyne interferometry. *Opt. Lett.*, 46(23):5830–5833, Dec 2021.

[96] T. Delahaye, R. Armante, N.A. Scott, N. Jacquinet-Husson, A. Chédin, L. Crépeau, C. Crevoisier, V. Douet, A. Perrin, A. Barbe, V. Boudon, A. Campargue, L.H. Coudert, V. Ebert, J.-M. Flaud, R.R. Gamache, D. Jacquemart, A. Jolly, F. Kwabia Tchana, A. Kyuberis, G. Li, O.M. Lyulin, L. Manceron, S. Mikhailenko, N. Moazzen-Ahmadi, H.S.P. Müller, O.V. Naumenko, A. Nikitin, V.I Perevalov, C. Richard, E. Starikova, S.A. Tashkun, Vl.G. Tyuterev, J. Vander Auwera, B. Vispoel, A. Yachmenev, and S. Yurchenko. The 2020 edition of the geisa spectroscopic database. *Journal of Molecular Spectroscopy*, 380:111510, 2021.

[97] Fei Wang, Shuhai Jia, Yonglin Wang, and Zhenhua Tang. Recent developments in modulation spectroscopy for methane detection based on tunable diode laser. *Applied Sciences*, 9(14), 2019.

[98] Jürgen Sautter, Isabelle Staude, Manuel Decker, Evgenia Rusak, Dragomir N. Neshev, Igal Brener, and Yuri S. Kivshar. Active tuning of all-dielectric metasurfaces. *ACS Nano*, 9(4):4308–4315, 2015. PMID: 25748581.

[99] Yuhang Sun, Yumin Liu, Tiesheng Wu, Yu Wang, Jing Li, Han Ye, Hongjie Fan, and Xueyu Wang. All-dielectric metasurface for linear-polarization conversion with an arbitrary polarization rotating angle. *Optics Laser Technology*, 157:108762, 2023.

[100] Amir Arbabi, Yu Horie, Mahmood Bagheri, and Andrei Faraon. Dielectric metasurfaces for complete control of phase and polarization with subwavelength spatial resolution and high transmission. *Nature nanotechnology*, 10, 08 2015.

[101] Yuri Kivshar and Andrey Miroshnichenko. Meta-optics with mie resonances. *Opt. Photon. News*, 28(1):24–31, Jan 2017.

[102] Patrice Genevet, Federico Capasso, Francesco Aieta, Mohammadreza Khorasaninejad, and Robert Devlin. Recent advances in planar optics: from plasmonic to dielectric metasurfaces. *Optica*, 4(1):139–152, Jan 2017.

[103] Andrei V. Kabashin, Sergiy Patskovsky, and Alexander N. Grigorenko. Phase and amplitude sensitivities in surface plasmon resonance bio and chemical sensing. *Opt. Express*, 17(23):21191–21204, Nov 2009.

[104] Peng Wang. Chapter two - phase-sensitive surface plasmon resonance sensors for highly sensitive bioanalysis. In You-Peng Chen and Teng-Fei Ma, editors, *Surface Plasmon Resonance in Bioanalysis*, volume 95 of *Comprehensive Analytical Chemistry*, pages 55–88. Elsevier, 2021.